UNIVERSITÀ
DEGLI STUDI
FIRENZE

TESYS RAIL

DOTTORATO DI RICERCA IN
INGEGNERIA INDUSTRIALE E DELL'AFFIDABILITÀ

CICLO XXXII

Development and validation of innovative damage tool to study wear, RCF and corrugation for railway applications

Settore Scientifico Disciplinare ING/IND 13

Dottorando
Dott. Butini Elisa

Tutor
Prof. Rindi Andrea

Co-Tutor
Prof. Benedetto Allotta
Dott. Ing. Meli Enrico
Dott. Ing. Marini Lorenzo

Coordinatore
Prof. De Lucia Maurizio

Anni 2016/2019

Ai miei genitori

You can't always get what you want
But if you try sometimes, well, you might find
You get what you need

The Rolling Stones, 1969

Index

Abstract I

Introduction 1

1. Layout of the damage tool 5

  1.1. Wear and RCF part 5

  1.2. Corrugation part 8

2. Wear: state of the art and current work 10

  2.1. Wear mechanisms 10

  2.2. Wear modelling approaches 15

    2.2.1. Sliding wear models 15

    2.2.2. Energetic approach models 16

  2.3. The current work: wear prediction model 17

    2.3.1. The local contact model 17

    2.3.2. The wear evaluation 20

    2.3.3. The profiles update 22

3. Rolling contact fatigue: state of the art and current work 29

  3.1. RCF defects 29

  3.2. RCF mechanisms 33

    3.2.1. Cyclic Fatigue and material responses 33

    3.2.2. Crack initiation 35

    3.2.3. Crack propagation 36

    3.2.4. Wear and RCF interaction 37

  3.3. RCF modelling approaches 38

  3.4. The current work: RCF prediction model 42

  3.5. RCF law characterization 47

4. Corrugation: state of the art and current work 51

4.1. Corrugation mechanisms and classification 51

4.2. Corrugation treatment 59

4.3. Corrugation modelling approaches 61

4.4. The current work: corrugation prediction model 64

4.4.1. The contact model 65

4.4.2. Track model 66

4.4.3. Damage model 68

4.4.3.1. The local contact model 69

4.4.3.2. The wear evaluation 70

4.4.3.3. Profile update 73

5. Test case: tramway application 74

5.1. Simulated Scenario 74

5.2. Wear 79

5.2.1. Wheel 80

5.2.2. Rail 89

5.2.2.1. New innovative measuring instruments 94

5.3. RCF 104

5.3.1. Wheel 104

5.3.2. Rail 105

5.4. Sensitivity analysis 107

6. Test case: subway application 112

6.1. Simulated Scenario 112

6.2. Wear 116

6.2.1. Wheel 116

6.2.2. Rail 124

6.3. RCF 128

6.3.1. Wheel 128

6.4. Corrugation 129

6.4.1. Measured data ... 130
6.4.2. Results ... 132
6.4.3. Sensitivity analysis ... 135
Conclusion ... 137
Recommendations for future works ... 139
References ... 140
Publications ... 147

List of figures

Fig. 1 Layout of wear-RCF part 5

Fig. 2 Layout of corrugation part 8

Fig. 3 Wear rates of R8T wheel material [43] 11

Fig. 4 UIC60 900A rail steel wear map [43] 11

Fig. 5 Wear rates as a function of $T\gamma/A$ for R8T wheel material tested with UIC60 900A rail material [43] 12

Fig. 6 Wear zones on the wheel [38] 13

Fig. 7 Different distributions of wear on the wheel [46] 13

Fig. 8 Rail profile changes due to contact conditions [49] 14

Fig. 9 Different distribution of wear on the rail [46] 14

Fig. 10 Wear map for Archard's coefficient [47] 16

Fig. 11 Contact patch discretization: (a) not constant grid resolution, (b) constant dimension cells 19

Fig. 12 Wear rate trend [8][16] 22

Fig. 13 Normal abscissa for the wheel profile 24

Fig. 14 Discretization of the mileage and the total vehicle number 25

Fig. 15 Simulation strategy 28

Fig. 16 Contact patch: adhesion and sliding zone 30

Fig. 17 Head Checking (HC) and gauge corner cracking (GCC) [48] 31

Fig. 18 Gauge Corner Cracking (GCC) [49] 31

Fig. 19 Breaks from a “tache ovale” [48] 32

Fig. 20 RCF damage on wheel [48] 32

Fig. 21 Wheel spalling [48] 32

Fig. 22 Rail shelling [48] 33

Fig. 23 Material response to cyclic loading [46] 34

Fig. 24 Shakedown map [43] 35

Fig. 25 Ratchetting and crack initiation [49] 36

Fig. 26 Ratchetting and crack initiation [49] 36

Fig. 27 Fluid entrapment [49] 37

Fig. 28 Wear vs fatigue. a) crack truncation; b) grow rate vs crack length; c) rail life vs removal rate [49] 37
Fig. 29 FIsurf on the shakedown diagram [18] 39
Fig. 30 WRLM damage function [17] 39
Fig. 31 Fracture mechanics mode [43] 40
Fig. 32 MMSA-2A test apparatus: 1. DC motor; 2. Drive belt; 3. Torque sensor; 4. Drive shaft gears; 5. Photosensor; 6. Wheel roller; 7. Rail roller; 8. Driven shaft gears; 9. Controller; 10. Computer; 11. Load sensor 47
Fig. 33 JD-1 test apparatus: 1.Normal loading cylinder; 2.Loading carriage; 3.Spindle and yoke; 4.Univesal shaft; 5.Wheel roller; 6.Wheel shaft; 7.Rail roller; 8.Lateral loading cylinder; 9.Turning plate; 10.Base plate; 11.Magnetic powder brake; 12.Speed measuring motor; A,B.ZQDR-204 DC motor; C.Gear box 48
Fig. 34 Crack dimensions 49
Fig. 35 Crack on wheel roller after 480 000 cycles 50
Fig. 36 Wavelength-fixing mechanism 52
Fig. 37 “Pinned–pinned resonance” corrugation with modulation over sleepers 55
Fig. 38 Rutting” on the inside (low) rail in a curve 56
Fig. 39 Torsional resonances of wheelset [58] 57
Fig. 40 “P2 resonance” corrugation on ballasted track, highlighted by grinding 57
Fig. 41 Simulation strategy 65
Fig. 42 Track reference system 67
Fig. 43 Rail surface description 67
Fig. 44 Lateral forces acting on the first leading wheelset wheels, expressed in the track coordinate system 68
Fig. 45 Discretization od rail profile along curvilinear lateral abscissa 69
Fig. 46 Rail “main grid” 70
Fig. 47 Distribution of nodes inside the contact patch 71
Fig. 48 Interpolation on the “small grid” 72
Fig. 49 Tramway Line 1 75
Fig. 50 Wheel-rail coupling 75
Fig. 51 Tram Sirio vehicle 75
Fig. 52 Vehicle nomenclature 75
Fig. 53 Multibody model of Tram Sirio 77
Fig. 54 Multibody model of the bogie 77

Fig. 55 Vehicle mission profile 78
Fig. 56 Vehicle model validation - load distribution 78
Fig. 57 Extract from EN14363: parameters for model validation 79
Fig. 58 Vehicle model validation - lateral acceleration comparison (R=600 m) 79
Fig. 59 Vehicle model validation- lateral acceleration comparison (R=140 m) 79
Fig. 60 Tram wheel reference parameters 80
Fig. 61 Plot of experimental wheel reference parameters of the first wheelset as a function of the mileage 83
Fig. 62 Plot of experimental wheel reference parameters of the third wheelset as a function of the mileage 84
Fig. 63 Starting profile of the wheel – CM1 wheelset 1 85
Fig. 64 Reference parameters comparison at first rail step – wheelset 1 86
Fig. 65 Reference parameters comparison at first rail step – wheelset 3 87
Fig. 66 Flange tip contact 88
Fig. 67 Simulated wheel profile evolution at first rail step – Motor bogie CM1 - leading wheelset 88
Fig. 68 Simulated wheel profile evolution at first rail step – Trailer bogie CP3 - leading wheelset 89
Fig. 69 Wheel reference parameters - Whole track vs statistical analysis 91
Fig. 70 Rail profile evolution – Curve R=38 m 92
Fig. 71 Rail profile evolution – Curve R=149 m 92
Fig. 72 Rail profile evolution – Curve R=1084 m 92
Fig. 73 Definition of rail wear control parameter 93
Fig. 74 QM dimension progress 94
Fig. 75 LW dimension progress 94
Fig. 76 Curve A-V08 layout 96
Fig. 77 HandySCAN 700 97
Fig. 78 Rail section used in laboratory analysis to preliminarily test the acquisition procedure 97
Fig. 79 3D optical scanning campaign 98
Fig. 80 Workflow to obtain 2D rail profiles starting from 3D surfaces 98
Fig. 81 Rail 3D wear map 99
Fig. 82 Cross sections 99
Fig. 83 Considered rail section related to the first measurement campaign 100

Fig. 84 Considered rail section related to the second measurement campaign 100

Fig. 85 Surfaces comparison between first and second measurement campaign 101

Fig. 86 Contact profilometer 101

Fig. 87 Experimental and simulated rail profiles comparison 102

Fig. 88 Experimental and simulated rail profiles comparison – zoom on rail flank zone ... 102

Fig. 89 Comparison between experimental and simulated lateral wear 103

Fig. 90 Simulated RCF crack depth evolution on wheel of the leading wheelset, left wheel105

Fig. 91 Simulated crack depth against the mileage 105

Fig. 92 Crack depth growth - Curve R=38 m 106

Fig. 93 Crack depth growth - Curve R=149 m 106

Fig. 94 Crack depth growth - Curve R=1084 m 106

Fig. 95 Crack depth growth as a function of the number of vehicles.................................. 107

Fig. 96 Test 1 - Effect on wear of a 105 mm wide wheel profile 108

Fig. 97 Test 1 – RCF damage on 105 mm wide wheel profile.. 109

Fig. 98 Test 2 - Effect on wear of a variable friction coefficient.. 110

Fig. 99 Test 2 – RCF damage with variable friction coefficient 111

Fig. 100 Multibody model of the benchmark vehicle 113

Fig. 101 Multibody model of the bogie... 113

Fig. 102 Even and odd track directions 114

Fig. 103 Speed profile of the four sections 115

Fig. 104 Variable rail profiles 115

Fig. 105 Position along the line of the reference curves.. 116

Fig. 106 Definition of the wheel wear control parameters 117

Fig. 107 Plot of experimental wheel reference parameters of the leading wheelset as a function of the mileage 119

Fig. 108 Measured right wheel profile from August 2015 to January 2016 – CM1 wheelset 1 120

Fig. 109 Measured left wheel profile from August 2015 to January 2016 – CM1 wheelset 1 120

Fig. 110 Starting profile of the right wheel – CM1 wheelset 1 120

Fig. 111 Starting profile of the left wheel – CM1 wheelset 1 121

Fig. 112 Reference parameters comparison at first rail step – left wheel 122

Fig. 113 Reference parameters comparison at first rail step – right wheel 123

Fig. 114 Comparison between experimental and simulated wear evolution – right wheel.. 124

Fig. 115 Comparison between experimental and simulated wear evolution – left wheel 124
Fig. 116 Plasser & Theurer EM-TRIPLEX 125
Fig. 117 Rail wear parameters 125
Fig. 118 Curve C17 - inner rail 126
Fig. 119 Curve C17 - outer rail 126
Fig. 120 Curve C23 - inner rail 127
Fig. 121 Curve C23 - outer rail 127
Fig. 122 RCF crack depth distribution 128
Fig. 123 RCF crack depth distribution on the right wheel 129
Fig. 124 RCF crack depth distribution on the left wheel 129
Fig. 125 Sensors for corrugation measurement 130
Fig. 126 Initial irregularities 132
Fig. 127 Rail surfaces corrugation a) low rail b) high rail 133
Fig. 128 DFT of the wear depth for the low rail 134
Fig. 129 Defect amplitude - numerical and experimental data 134
Fig. 130 Influence of friction coefficient on corrugation amplitude 136
Fig. 131 Influence of rail hardness on corrugation amplitude 136

List of tables

Table 1 Chemical compositions of the specimens 49
Table 2 Experimental tests performed 50
Table 3 Types of corrugation, characteristics and treatments 54
Table 4 Main vehicle and line characteristics 76
Table 5 Tram Sirio reference quotas limits 81
Table 6 Experimental wheel wear parameters 82
Table 7 Wear loop parameters 85
Table 8 Data of the curvilinear and straight tracks of the statistical analysis 90
Table 9 Wear loop parameters 90
Table 10 Total tonnage burden on track 93
Table 11 HandySCAN 700 technical specifications 97
Table 12 Experimental lateral wear values 102
Table 13 Experimental lateral wear as function of the vehicles number 103
Table 14 Simulated lateral wear as function of the vehicles number 103
Table 15 Sensitivity analysis 108
Table 16 Test 1 - Difference in the mileage travelled 109
Table 17 Test 1 - Difference in crack depth 109
Table 18 Test 2 - Difference in the mileage travelled 111
Table 19 Test 2 - Difference in crack depth 111
Table 20 Principal vehicle and line characteristics 113
Table 21 Reference curve characteristics 116
Table 22 Wheel reference quotas limits 117
Table 23 Experimental wheel wear parameters 118
Table 24 Wear loop parameters 121
Table 25 Real and simulated number of vvehicles 127
Table 26 Corrugation measurements of the low rail of the reference curve 131
Table 27 Sensitivity analysis tests 135

Abstract

Nowadays, one of the issues in the railway field is the decreasing in life of wheel and rail. The main damage is caused by wear, rolling contact fatigue and corrugation which deeply affects wheel and rail. These phenomena are closely connected and directly impact both on vehicle dynamics (comfort, stability, safety, etc..) and on the costs (line management, maintenance, etc.), decreasing the useful life of wheel and rail. To face these problems and detect abnormal operating conditions, this Ph.D. work aims at developing a modelling approach for railway applications that effectively combines wear, Rolling Contact Fatigue (abbreviated to the acronym RCF) and corrugation models. The proposed methodology is capable of simultaneously predicting both the profiles shape evolution due to wear and the total RCF damage along the wheel and rail profiles, reaching a good compromise between accuracy and efficiency. Moreover, the corrugation part of the tool allows to have as output the 3D corrugated rail surfaces to study the rail roughness growth as a function of train passages. Thanks to the high numerical efficiency, the damage models can be easily implemented into complex multibody models of railway and tramway vehicles to perform large-scale simulations in a reasonable time. In this way, thanks to the multibody dynamics simulations, it is possible to take into account all the various wheel-rail contact conditions which can occur while the vehicle is running. The development of easy and fast damage models is the main feature for a wheel-rail life prediction tool to be applied to different scenario and vehicles.

Finally, the proposed prediction tool has been applied to different scenario and validated by means of on-field experimental data and through specific laboratory tests carried out on a dedicated test-rigs.

Introduction

The most important factors which negatively affect the life of wheels and rails are intensive wear, rolling contact fatigue (RCF) and corrugation. Consequently, the prediction of wear, crack growth and corrugation is a fundamental problem in railway field, directly connected to maintenance planning, vehicle dynamics and safety. Assuring a good health status of wheel and rail surfaces is a crucial aspect: wear and the other damage mechanisms cause changes in wheel and rail profiles with a great effect on vehicle dynamics and on running stability, leading to a performance decay and less comfortable ride. Therefore, the original profiles must be periodically reconstructed by means of turning or grinding, in order to guarantee the running under safe condition. For these reasons, the development of a reliable damage tool represents a powerful instrument both in vehicle design phase and for the maintenance planning aiming to keep the maintenance costs as low as possible. Hence, the main goal of this Ph.D. thesis is to propose a new and efficient modelling strategy, combined with multibody dynamics simulations, for the simultaneous wear and RCF assessment and rail corrugation growth prediction on general railway lines. Starting from the requirement of non-use a time-consuming Finite Element Model, the proposed tool is fast and simple to implement also in a complex scenario. Such a model can also help in the design of new optimized wheel and rail profiles to obtain a more uniform wear evolution or less RCF damage or investigate the possible causes that lead to corrugation growth.

Concerning wear and RCF, in literature, many important research works investigating these two phenomena can be found. About wear, models specifically developed for complex railway networks [1][2] and not very time consuming [3][4] (then suitable for large-scale simulations using multibody models) are not so frequent. Both approaches based on Archard's law [5][7] and strategies relying on the T-gamma are usually exploited in railway applications [6][7][16]. In this Ph.D. thesis, the T-gamma approach will be exploited and improved to properly combine it with the RCF model.

As regards RCF prediction, many model have been proposed in literature during the years [10][14][17][20][21][22]. Two main approaches can be identified: models based on finite element analysis and models exploiting empirical laws. Despite their high accuracy, the models of the first group [9][10][11] are critical in terms of computational efficiency and are too complex to be used in large scale multibody dynamic simulations of railway networks.

Concerning the second group, in general, two lines of research are present in the literature: the first one adopts a frictional energy based approach (Whole Life Rail Model - WLRM - by Burstow [17]), including the effect of wear on RCF damage. The second one makes use of the 'shakedown limit' [18][19] to calculate the tangential stresses above which the crack appears but it does not take into account the wear contribution. The models of the second group have the main disadvantage that they are not able to evaluate the crack length / depth and, consequently, the damage level; they only determine if the RCF damage occurs. In [14][15] this approach is improved: the crack dimensions are calculated by using a suitable fatigue damage law and the wear effect on crack is considered.

The RCF model considered in this Ph.D. work belongs to the second groups and further improves the approach described in [14][15]. The new model, relying on an experimental relationship between the shear stresses at the wheel-rail contact and the crack dimensions, can evaluate both the crack dimensions (including also the effect of wear on crack growth) and the position of the crack along the wheel and rail profiles (fundamental to know the location of the damage).

Furthermore, the literature lacks efficient models (even if heuristic) able to predict both wear and RCF [21][22] and suitable for complex railway networks. To face this issue, the proposed approach is specifically developed to assure high numerical efficiency and to be applied to complex railway lines, where large-scale multibody simulations are necessary.

More specifically, the general layout of the wear and RCF model proposed in this work consists of three parts: the vehicle model (multibody vehicle model and global wheel-rail contact model) that interacts with the wear model (local contact model, wear evaluation and profiles update procedure) and the RCF prediction model. As regards the wear estimation, the model is based on an experimental relationship found in literature connecting the removed material to the energy dissipated by friction at the contact [16]. In parallel to the calculation of the material removed by wear, the RCF model is able to predict both the crack position on the wheel and rail profiles and the crack dimensions (length and depth). The RCF model takes into account the effect of wear and relies on an experimental relationship between crack length and stress. To characterize the RCF damage law, specific fatigue tests were carried out in the laboratory of the Tribology Research Institute of the Southwest Jiaotong University, using a dedicated two rolling-sliding test machines.

Rail corrugation it has been and it is still today an important research topic due, mainly, to its deep effect on comfort, noise and vehicle dynamic behaviour. Rails are prone to develop periodic irregularities, which are known as corrugation when their wavelength is less than about a meter. This kind of irregularities, characterized by a specific wavelength, are mostly observed on the crown of the inner rail in curves with small radius. This defect can reach amplitudes of tenths of millimetres if not properly controlled and its growth requires maintenance interventions, whenever the allowable limits are overcome. Both corrective and preventive maintenance of the vehicle track system is expensive, and vibrations bother passengers and people nearby the railway track. To date, there is no neat and general solution to face this issue, probably because it is not yet fully understood. In some case, the solutions commonly adopted are demonstrably successful, even if not satisfactory, in other cases, their effectiveness is not certain. The most common mitigation action is rail grinding, expensive and it does not remove the origin of the problem. For this reason, inside the damage tool a model to predict the corrugation growth has been implemented to better understand this phenomenon and assess the effectiveness of the commonly adopted solution. In addition, a tool to predict this phenomenon can be useful to plan the maintenance interventions, consisting in rail reprofiling by means grinding of the running surfaces.

The corrugation part, as the previous described model, consists of two main blocks: the dynamic model and the damage block. The dynamic model carries out a dynamic analysis of the railway vehicle running on a track, calculating the forces acting at the wheel-rail interface. The damage block implemented in Matlab, calculates the quantity of material to be removed from the rail surfaces and updates the rail surfaces, to simulate the corrugation growth. During the service, wheels change their profile because of wear. The proposed model considers this effect including the variability of wheel profiles in the simulation of corrugation growth.

A critical aspect in the development of a tool able to predict rail and wheel damage is the availability of the experimental data necessary to validate the whole model. In fact, they require a long time to have a tangible effect and then several months of monitoring to collect data. In this Ph.D. thesis work, the model will be validated by comparison with a set of experimental data provided by our partners and related to a tramway and a subway application.

In Chapter 1, the general layout of the damage tool will be described. Then, after a brief excursus on the main damage phenomena considering in this Ph.D. thesis and their current modelling approaches, in Chapter 2 and Chapter 3 a detailed description of the theory and methodology behind wear and RCF models will be provided.

Corrugation model will be described in Chapter 4 together with causes and characteristic of all type of corrugations observed to this day.

In Chapter 5 and Chapter 6 the considered test cases will be presented and the numerical results will be compared with experimental data provided by our partner.

1. Layout of the damage tool

In this chapter a description of the general architecture of the proposed damage tool will be explained, focusing on its two main constituting parts: the wear-RCF part and the corrugation part.

1.1. Wear and RCF part

The general layout of the wear and RCF part is made up of two main blocks: the dynamic system and the wear-RCF model (see Fig. 1).

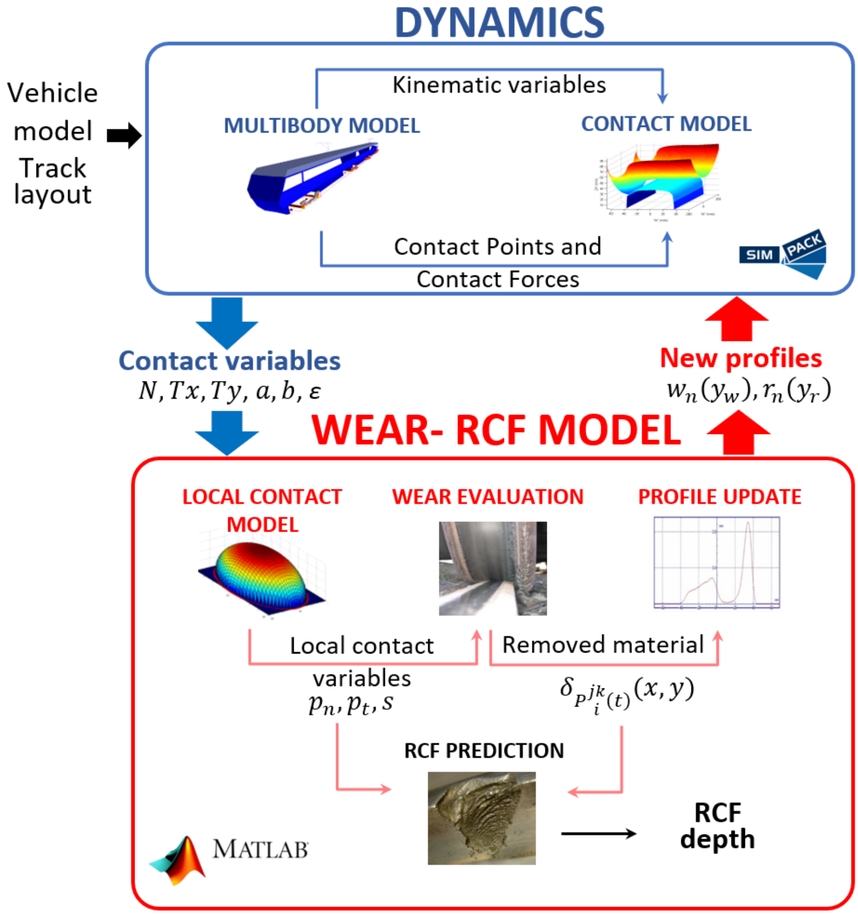

Fig. 1 Layout of wear-RCF part

The *dynamic block* consists of a multibody model of the benchmark vehicle, built in Simpack Rail environment, and of a global contact model. Multibody simulation (MBS) is particularly suitable for the study of complex systems as a railway vehicle running on a track and, in general, is used to predict and optimize the behaviour of any type of multibody system, by solving the equations of motion. Bodies connections of a multibody system are modelled by means of joints and kinematic constraints, which allow certain relative motions and restrict others. The bodies themselves can be modelled as rigid or flexible. The degrees of freedom (DOF) are represented by several independent state variables that define the motion of the bodies (displacement and deformation). The movements within these degrees of freedom are influenced by arbitrary forces and torques provided by according elements. Dynamic problems describe the motion of the system due to the applied forces and the inertia characteristics of the bodies, i.e. their mass, moments of inertia and position of the centre of gravity. For the resolution of dynamic analysis, the multibody model, consisting in a series of modelling element (rigid and flexible bodies, spring, dampers etc.), together with constraints, is converted in a set of differential-algebraic equations (DAE), following a Lagrangian approach. These equations, in this case study are not linearized so they are solved in the time domain, with a proper time-step algorithm. During the dynamical simulation the vehicle and the contact model interact online creating a loop. Generally, the resolution of wheel-rail contact is divided into three phases: detection of contact points, calculation of normal pressure distribution and calculation of tangential pressure distribution. Simpack Rail software already includes several wheel-rail contact models but in this work a 3D global contact model developed by the University of Florence in previous years [26][27] is adopted to achieve better accuracy and reliability. The contact model uses the distance method algorithm [26] to detect the positions of the contact points. Then, for each contact point, the model calculates contact forces (normal and tangential) and the global creepages of the contact patch through Hertz's and Kalker's global theories [30][31]. The global contact variables are then passed to the multibody model in order to carry on the simulation of the vehicle dynamics.

The track and the multibody model of the considered vehicle are the main inputs of the dynamic block. More particularly, in this Ph.D. research activity, the track model represents for the first test case the entire Tram Line 1 of the city of Florence that connects the railway station Santa Maria Novella to the suburban area of Florence. Instead, for the second test case, a subway line has been considered.

Inside the *wear-RCF block,* the models to simultaneously evaluate the wear evolution and crack propagation are implemented. The wear model consists of three distinct phases: the local contact model, the wear evaluation and the profile update. The local contact model (based both on Hertz's local theory and on simplified Kalker's algorithm **FASTSIM** [30][31]), starting from the global contact variables (outputs of multibody simulation), evaluates the local contact variables (contact pressures and local creepages inside the contact patch) and divides the contact patch into adhesion area and slip area. Then, the distribution of removed material is calculated on the wheel and rail surface only within the slip area using an experimental law connecting the removal material to the energy dissipated by friction at the contact interface [16]. Finally, the wheel and rail worn profiles are obtained from the original ones through an innovative update strategy. The new updated wheel and rail profiles are then fed back as inputs to the vehicle model and the whole model architecture can proceed towards the next discrete step. The whole model is therefore based on a discrete process: each discrete step consists in one dynamic simulation and one profile update by means of the wear model. The choice of an appropriate step is fundamental in terms of accuracy and computational load: an increase in the number of steps improve the model precision but, at the same time, the simulation times increase too. Different types of update procedures exist in literature [4][36]. In the constant step approach a constant update step is defined while in the adaptive step a threshold value that imposes the maximum material quantity to remove at each profiles update is imposed and consequently the update step is variable. The second one has been adopted because it is more suitable to follow the nonlinear behaviour of the wear evolution. In fact, the wear evolution is, in a first phase, characterized by a higher rate due to the initial non conformal contact between the unworn profiles while, in a second phase, a slower rate due to the high conformal contact is present.

Moreover, the different time scales characterizing the wheel and rail wear evolution require the development of a suitable strategy for the profiles update. More in detail, the wheel profile update strategy proposed is based on the total distance travelled by the considered vehicle, while the rail profile update strategy is based on the total tonnage burden on the track. In such a way, the removal of material is carried out considering the different time scales of the wheel and rail wear evolution.

The RCF model is implemented in parallel with the wear model (see Fig. 1), allowing the simultaneous evaluation of the removed material due to wear and of the crack growth (in terms of length and depth) both for the wheel and for the rail. Contact stresses, contact creepages and calculated wear are the only inputs for the RCF model.

The influence of wear on crack growth is taken into account at the end of each calculation step. In fact, wear and RCF are deeply connected: wear changes the wheel and rail profiles influencing the stresses magnitude at the wheel–rail contact and leading to a higher or less RCF damage. Furthermore, in presence of a high wear rate, short cracks may also be worn off.

1.2. Corrugation part

The corrugation part has basically the same layout described in the previous paragraph for the wear-RCF model. While in the wear-RCF model both the wheel and the rail are considered, this part of the tool deals only with the rail since this kind of phenomenon occurs on this component. The general architecture shown in Fig. 2 consists of two different sub-models, the dynamic model and the corrugation model.

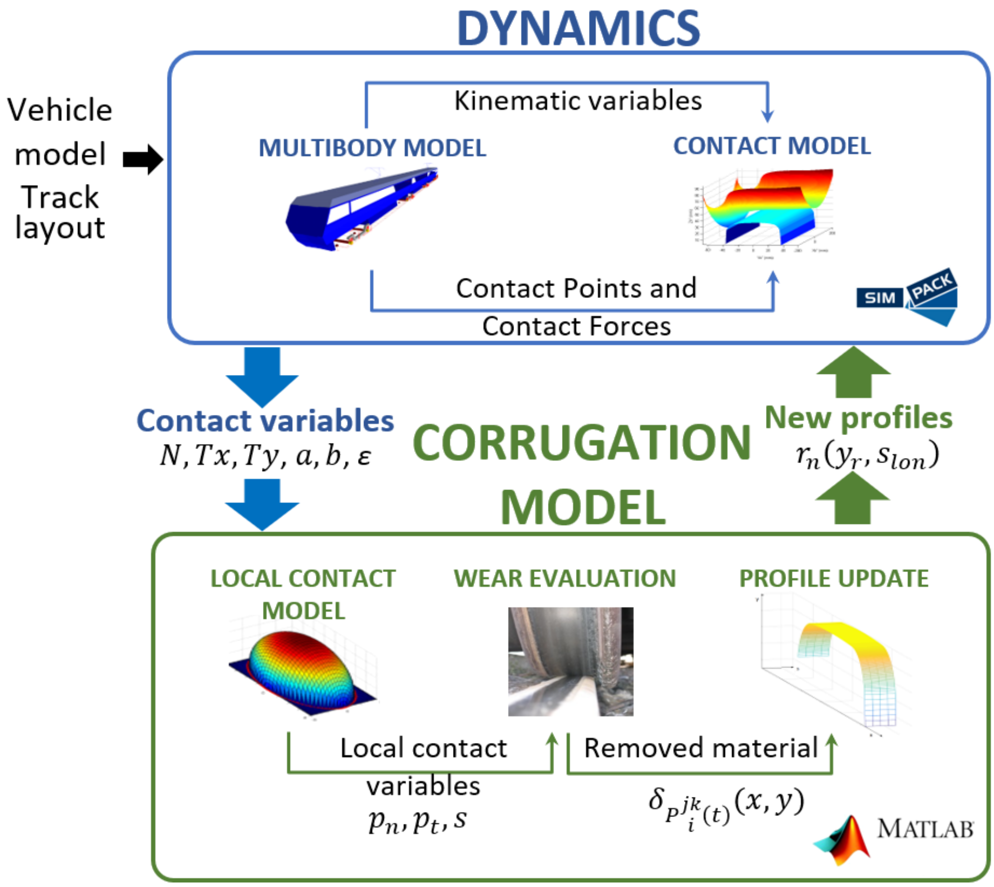

Fig. 2 Layout of corrugation part

In the dynamic block the dynamic analysis is carried out using the multibody software, Simpack Rail, as previously mentioned. The main inputs of the dynamic model are the railway track characteristics (i.e. track layout, rail surfaces, mission profile) and the benchmark vehicle model. In the dynamic simulation the global contact variables, normal and tangential global forces, semi-axes of the contact patch and the global creepages are evaluated and stored. Once the dynamic analysis is carried out, the global contact variables are passed to the damage block which evaluates, in a post-calculating step, the worn rail surface to pass back to the multibody model. It has to be taken into account that corrugation starts growing because an initial irregularity is present on the rail surface. Therefore, to describe the corrugated rail surfaces, a series of different rail profiles are implemented in Simpack multibody model according to a post grinding measurement. Rail profiles are in function of the curvilinear longitudinal coordinate s_{lon}, which represents the length of the considered track. These profiles are updated each step of the iterative process since wear defines a variation of the rail head which in turn gives a new initial irregularity.

2. Wear: state of the art and current work

In this Chapter, after a brief state of the art about the main wear mechanisms and modelling approaches proposed over the years followed by a detailed description of all the phases (the local contact model, the evaluation of the amount of removed material and the wheel and rail profile updating procedure) constituting the wear model will be provided. The latter is included both in the wear-RCF and in the corrugation part.

2.1. Wear mechanisms

Wear can be defined, according to the definition in [37], as the loss or displacement of material from a contacting surface. Surface wear is generally accompanied by the creation of wear debris which may be harder than one or both surfaces and which will result in further wear. Material displacement may occur by transfer of material from one surface to another by adhesion or by local plastic deformation. Several different types of mechanisms may lead to wheel and rail surfaces wear: chemical process, as corrosion or a physical process such as abrasion, adhesion or fatigue. Each of these different wear mechanisms produce a different wear rate. A simple classification in three different types of wear can be done depending on wear rate: "mild wear" "severe wear" and "catastrophic wear"[40][41][43]. Mild wear is characterised by the removal of materials in very small fragments resulting in a smooth surface that often is smoother than the original one. Mild wear is favourable in many cases for the wear life of the contact as it causes a smooth run-in of the contacting surfaces. However, in some cases it has been observed that it worsens the contact condition causing an unfavourable change in the shape of the surfaces in contact. On the other hand, severe wear results in a rough surface that often is rougher than the original surface. Since the first studies [40][41][43] it has been clear that three different wear regimes could be identified, in terms of wear rate, surface appearance, metallographic structure and wear debris. Type I (mild) wear is characterized by oxidative mode, debris are small, typically on the order of 100 nm, the result surface is extremely smooth. Type II (severe) results in a rough, deeply torn surface and debris are around 0.01 mm diameter and like catastrophic regime, it is characterized by surface cracking and material loss [41]. These three wear regimes described above have been pointed out during rolling/

sliding tests on specific test rigs with different wheel and rail materials. As an example, in Fig. 3 the wear rates are plotted as a function of the slip for a R8T wheel material.

The passage between these three wear regimes depends on the combination of contact pressure and sliding velocity [40][43] as shown in Fig. 4 for a wheel-rail contact using R7 wheel material and UIC 60 900A rail. According to field measurements carried out by Olofsson and Nilsson [44] usually the wheel tread and railhead wear are in the mild regime and wheel flange and rail gauge corner wear fall in the severe or catastrophic regime.

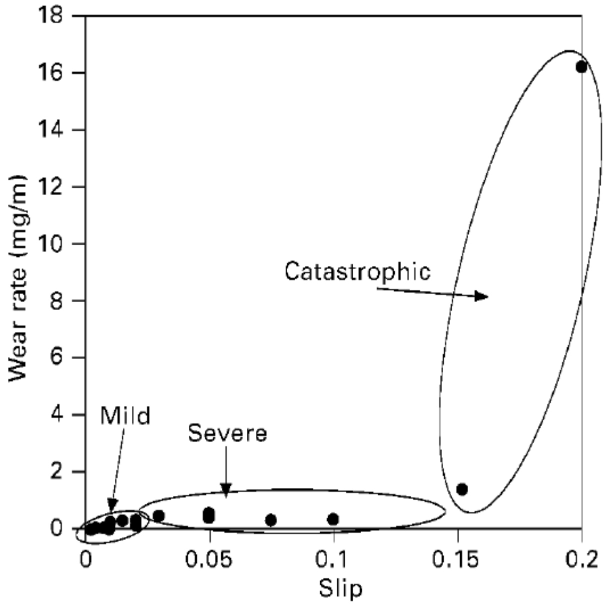

Fig. 3 Wear rates of R8T wheel material [43]

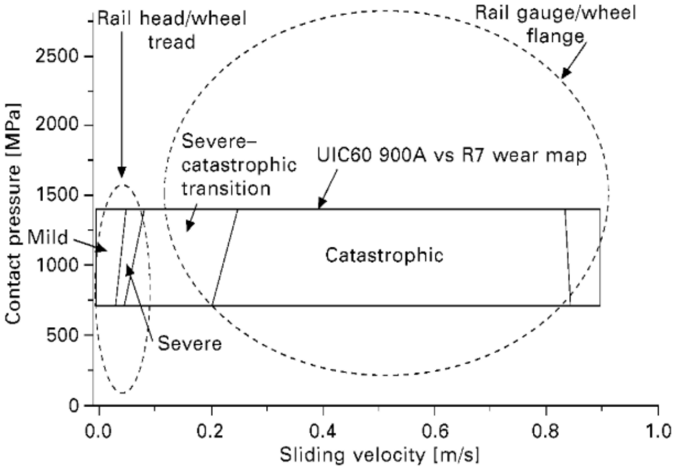

Fig. 4 UIC60 900A rail steel wear map [43]

A common approach in literature [8][40][41] is to plot the wear rate against a parameter, $T\gamma/A$ which is indicative of the work done at the contact, where T is the tractive force (normal load divided by friction coefficient), γ is the slip and A is the contact area. This method of plotting experimental data allows the comparison of different test geometries. As an example in Fig. 5, the wear rate (μg material lost/m rolled/mm^2 contact area) is plotted against $T\gamma/A$ index for a R8T wheel material tested with UIC60 900A rail.

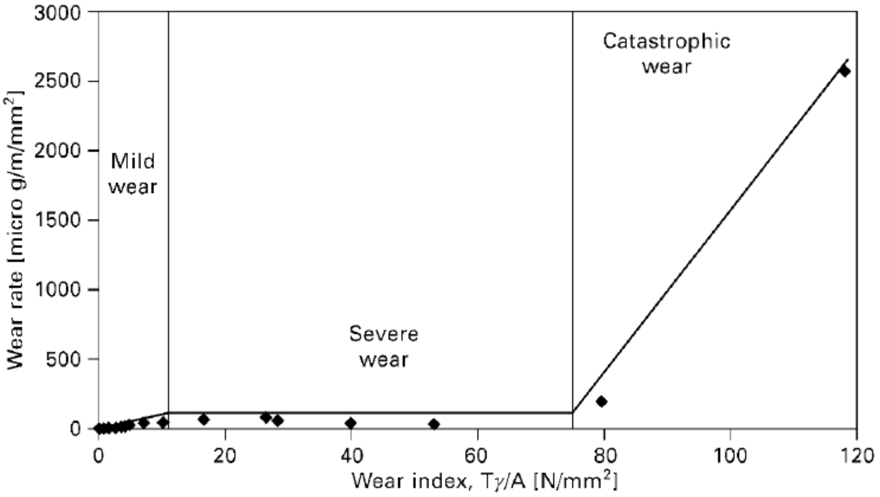

Fig. 5 Wear rates as a function of $T\gamma/A$ for R8T wheel material tested with UIC60 900A rail material [43]

As said previously, wear may take place through different mechanisms [42], sometimes several at the same time. In briefly, the dominant wheel-rail wear mechanisms are:

- *Oxidative wear*, which involves the formation of oxides of iron on the surface of the material; it is typical of when the forces and sliding velocity are small and for low $T\gamma/A$ values. It is clearly related to the presence of oxygen, humidity, temperatures;

- *Adhesive wear*, when in a sliding contact the adhesion forces are high, shear takes place in the material instead of at the contact surface. This may result in detachment of fragments from one surface and attachment to the other surface;

- *Abrasive wear*, when contact is between surfaces of significantly different hardness, or because of hard particles are trapped between the surfaces;

- *Fatigue wear*, which takes place as a consequence of loading and unloading cycles; it consists of cracks forming at and underneath the surface. The cracks propagate and particles from the surface may break away. Wear and fatigue are in competition: when the wear rate is high, fatigue cracks have no time to grow and simply are worn off. An increase in hardness of the rails leads to less adhesive and abrasive wear but in more fatigue damage.

Wear is localized in different zones of wheel and rail depending on where the contact position is. Generally, the amount of wear is lower when the vehicle is running on straight track since the reduced sliding of the wheel.

Concerning the wheel (see Fig. 6), usually the largest amounts of wear are localized on tread (*tread wear*) and on the flange (*flange wear*). Depending on the type of network where the vehicles operates, the distribution of wear may variate. With reference to Fig. 7, wear on the wheel flange will be higher in presence of many narrow curves. In fact, a small curve radius implies a large angle of attack and then higher wear. When the line is mainly straight, wear will be concentrated on wheel tread. In presence of high tread wear (the so-called *hollow wear*) ride instability problems may occur due to an increase in the wheel conicity.

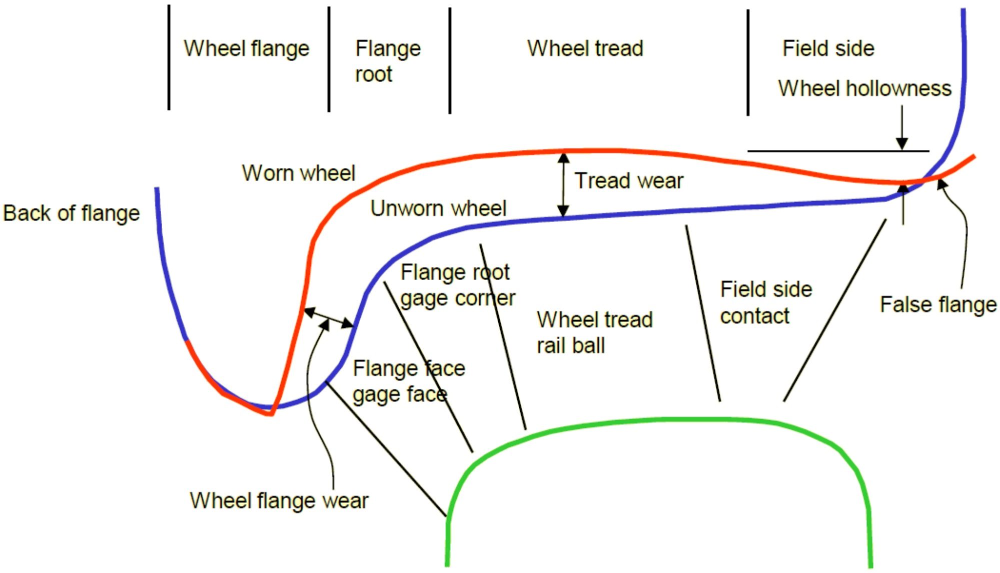

Fig. 6 Wear zones on the wheel [38]

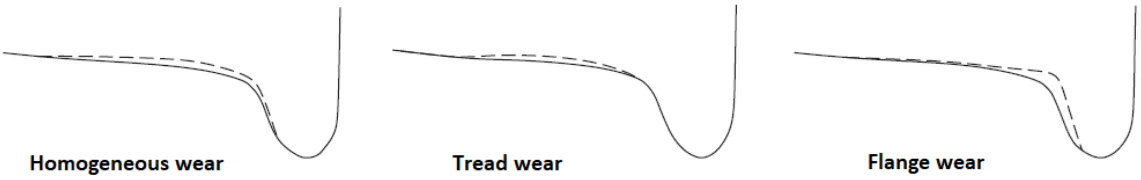

Fig. 7 Different distributions of wear on the wheel [46]

Focusing on the rail (see Fig. 8 and Fig. 9), the way how a rail wears out depends on its location in a curve or on a straight track. Obviously in a curve, the rail experiences higher creep forces and creepages with a consequent more wear. The contact on the outer rail in a curve is located at the gauge side and most of the wear will take place in this zone. For the inner rail in a curve, the highest wear will be located on top of the rail. For rail profiles on straight track, the wear will be more evenly distributed on the top and at the gauge corner. In Fig. 8 the change in shape that develops as a result of plastic flow, contact fatigue, and wear due to different contact condition is shown.

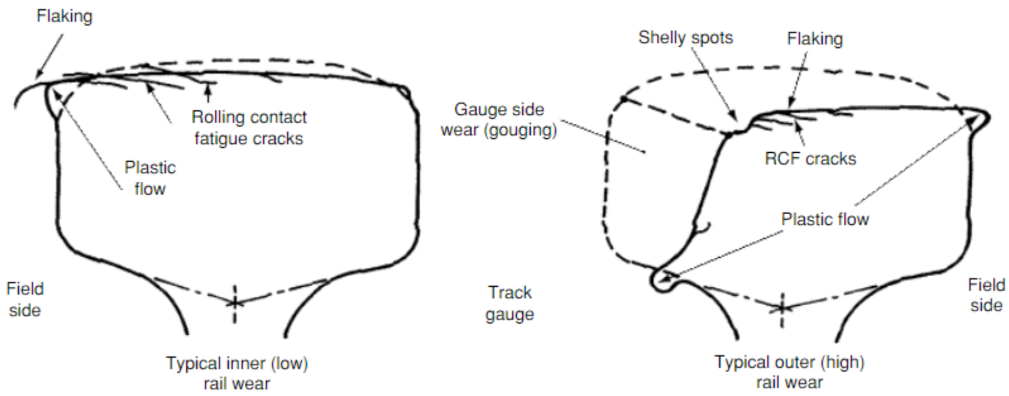

Fig. 8 Rail profile changes due to contact conditions [49]

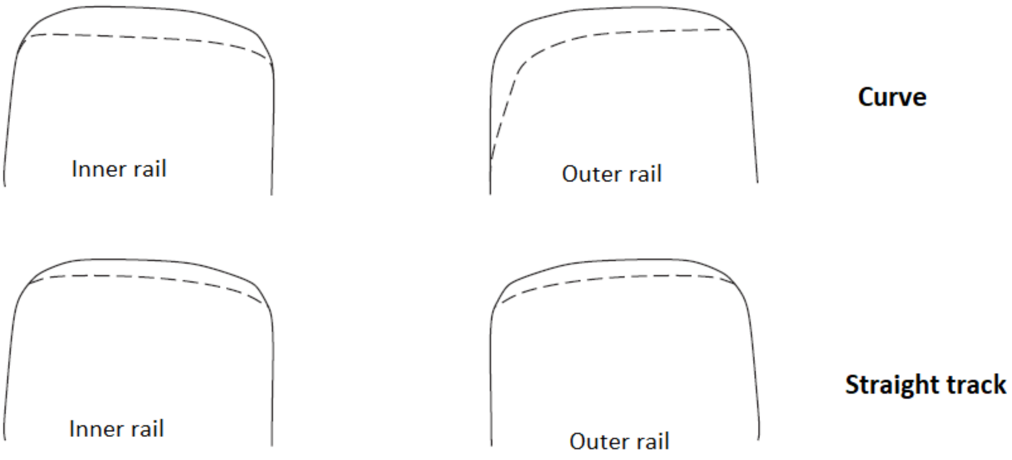

Fig. 9 Different distribution of wear on the rail [46]

Wear directly affects the wheel and rail profile geometry, being therefore a crucial factor for safety against derailment, ride comfort and vehicle dynamic behaviour. Furthermore, due to a change in wheel and rail surface, wheel-rail forces increase and so also the damage to vehicle and track. For all these reasons, wear and in general all the other damage mechanisms are important in terms of running safety.

2.2. Wear modelling approaches

Wear models exist in literature both based on finite element analysis and on empirical laws [4][5][6][7][16][45]. The firsts are accurate, but critical in terms of computational load and not suitable for complex systems analysis. The second group includes two lines of research:

- sliding models described by Archard [45], where the wear rate is related to the sliding distance, normal force and material hardness;
- frictional work (energy) which relates the wear rate to the energy dissipated at the contact [6][7][16].

Both the approaches can be led back to Reye's hypothesis of sliding between bodies, according to which the volume of material loss on a surface is proportional to the work done by frictional forces.

2.2.1. Sliding wear models

The Archard's model [45] predicts the volume of removed material V_W in m^3, based on the experimental formula and correlated to the material hardness H, the normal load N and the sliding distance s through the wear coefficient k_i.

$$V_W = k_i \frac{\mathbf{s} \cdot N}{H} \qquad (2\text{-}1)$$

The coefficient k_i can be determined by experimental results and a wear map can be built as function of the sliding velocity and contact pressure [47]. According to Archard's model, in the adhesion zone of the contact patch no wear is calculated since the sliding is zero. As in some of the energetic approach wear models, the Archard sliding wear model divides the contact patch area into a small grid of elements and the total amount of wear is the sum of the wear calculated for each element.

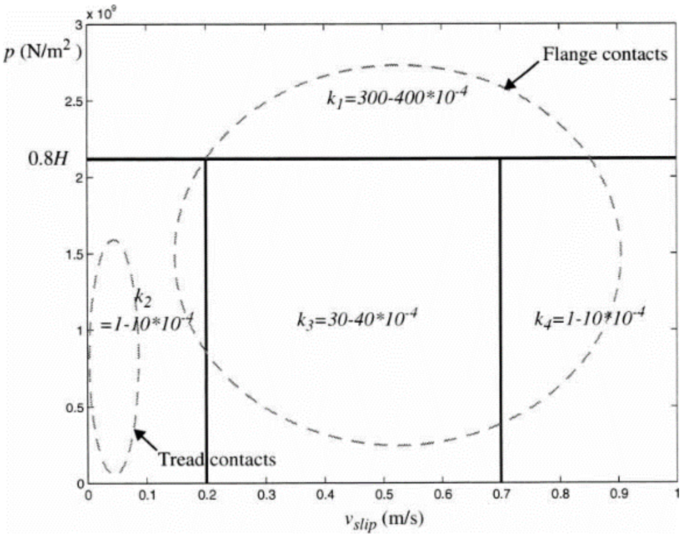

Fig. 10 Wear map for Archard's coefficient [47]

2.2.2. Energetic approach models

According to this approach, the wear rate can be connected to the frictional energy dissipated through creepage at the contact interface as shown in (2-2) where T are the creep forces and γ the creepages in the longitudinal and lateral directions.

$$T\gamma = T_x\gamma_x + T_y\gamma_y \tag{2-2}$$

In a BR Research has been observed that the wear rate in severe wear regime could be modelled more accurately considering the parameter $T\gamma / A$, where A is the area of the contact patch [47]. In the work of Braghin et al. [16] a twin-disc setup with R8T wheel steel on UIC60 900A rail steel has been used to obtained the experimental correlation between the wear rate and the work done at the contact interface normalized on the area $T\gamma / A$ by a constant K_i which depends on the wear regime:

$$\text{wear rate} = K_i \frac{T\gamma}{A} \tag{2-3}$$

where the wear rate is expressed in terms of material weight [μg] per distance travelled [m] per contact area [μg/m mm^2]. The values of K_i depend on the wear regimes mild, severe and catastrophic (see Fig. 5).

In this Ph.D. work the latter modelling approach has been chosen since the wide experience of the University of Florence in using this approach and its good behaviour proved during other works [1][2]. For this reason, the model will be discussed in detail in the following paragraph.

2.3. The current work: wear prediction model

With reference to Fig. 1 and Fig. 2, the wear model consists of three distinct phases:

- the local contact model which calculates the local contact variables;
- the wear evaluation which evaluate the removed material by wear;
- the profiles update necessary to obtain the new worn profiles.

The following subparagraphs will describe more in details these phases.

2.3.1. The local contact model

In the first one the local contact model, based on Hertz local theory and on simplified Kalker's algorithm FASTSIM [30], starting from the global contact variables calculated by the multibody simulation (global normal and tangential forces, global creepages and contact patch dimensions), evaluates the local contact variables (contact pressures p_n, $\mathbf{p}_t$ and local slip $\mathbf{s}$ within every discretization point of the contact patch) and divides the contact patch into adhesion area and creep area.
A new reference system is defined at the wheel-rail interface on the contact plane (i.e. the common tangent plane between the wheel and rail surfaces) where the x and y axes are the longitudinal and the transversal direction of the contact plane respectively (see Fig. 11).

The algorithm considers an elliptical normal pressure distribution according to Hertz theory and it is based on the proportionality hypothesis between the tangential contact pressure $\mathbf{p}_t$ and the elastic displacements $\mathbf{u}$ by means of the constant flexibility coefficient L:

$$\mathbf{u}(x,y)=L\mathbf{p}_t(x,y) \qquad L=L(\varepsilon,a,b,G,\nu) \tag{2-4}$$

The flexibility parameter is a function of the global creepages ε, the semi-axes of the contact patch a,b, the wheel and rail combined shear modulus G and the wheel and rail combined Poisson's ratio ν:

$$L=\frac{|\varepsilon_x|L_1+|\varepsilon_y|L_2+c|\varepsilon_{sp}|L_3}{\left(\varepsilon_x{}^2+\varepsilon_y{}^2+c^2\varepsilon_{sp}{}^2\right)^{1/2}} \tag{2-5}$$

with

$L_1=8a/(3GC_{11})$ $L_2=8a/(3GC_{22})$ $L_3=\pi a^2/(4GcC_{23})$

where $c=\sqrt{ab}$ and C_{ij} are the Kalker's parameters that can be found in literature. The local creepages $\mathbf{s}$ can be calculated by derivation considering both the elastic creepages and the rigid ones:

$$\mathbf{s}(x,y)=\dot{\mathbf{u}}(x,y)+V\begin{pmatrix}\varepsilon_x\\ \varepsilon_x\end{pmatrix} \tag{2-6}$$

where V is the longitudinal vehicle speed.

As written before, the contact patch is discretized in a grid of points in which the quantities p_n, $\mathbf{p}_t$ and $\mathbf{s}$ are evaluated. One of the fundamental feature of the algorithm is the elliptical contact area discretization using a grid with cells of Δx longitudinal length and Δy lateral width (see Fig. 11(a)).

In particular:

- the transversal axis (with respect to the motion direction) of the contact ellipse has been divided in (n_y-1) equal parts of magnitude $\Delta y=2b/(n_y-1)$ by means of n_y equidistant nodes;

- the longitudinal sections of the patch (long $2a(y)=2a\sqrt{1-y/b^2}$) have been divided in (n_x-1) equal parts of magnitude $\Delta x(y)=2a(y)/(n_x-1)$ by means of n_x equidistant nodes.

Basically, to each stripe of width Δy , corresponds a semi-axis $a(y)$ function of lateral position within the contact patch.

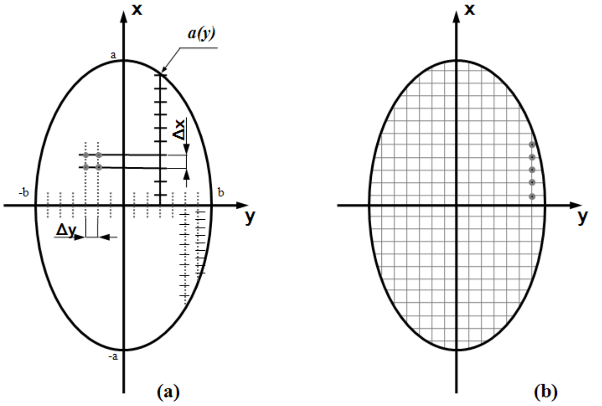

Fig. 11 Contact patch discretization: (a) not constant grid resolution, (b) constant dimension cells

Thanks to this strategy, grid resolution along longitudinal direction is not constant but increases near the lateral edges of the ellipse, where the lengths $a(y)$ are smaller. In face of a slight increase in computational time, this procedure provides more accurate results near the edges of the ellipse, where a constant resolution grid would generate excessive numerical noise. The choice of n_x and n_y values should guarantee a good compromise between precision and computational load: greater the values will be and more precision will be achieve but, on the other hand, with an increase in computational time.

After the contact patch discretization, the following step of the FASTSIM algorithm consists in the evaluation of both the contact pressure values p_n , $\mathbf{p}_t$ and the local creepages $\mathbf{s}$ in order to divide the contact patch in adhesion and slip zone, necessary to evaluate the volume removed by wear. The latter will be calculated only in the slip zone. Indicating the generic point of the grid with $(x_{i,}y_j)$, $1\le i\le n_x$ $1\le j\le n_y$, the normal contact pressure can be expressed as:

$$p_n(x_{i,}y_j)=\frac{3}{2}\frac{N^r}{\pi ab}\sqrt{1-\frac{x_i^2}{a^2}-\frac{y_j^2}{b^2}} \qquad (2\text{-}7)$$

where N^r is the normal contact force (output of dynamic simulation performed in Simpack), while the limit adhesion pressure $\mathbf{p}_A$ is:

$$\mathbf{p}_A(x_i,y_j) = \mathbf{p}_t(x_{i-1},y_j) - \begin{pmatrix} \varepsilon_x \\ \varepsilon_y \end{pmatrix} \frac{\Delta x(y_j)}{L} \tag{2-8}$$

thus, knowing the variable values in the point (x_{i-1},y_j) it is possible to pass to the following point (x_i,y_j) according to Coulomb's adhesion law:

$$\text{if} \qquad \left\|\mathbf{p}_A(x_i,y_j)\right\| \le \mu p_n(x_i,y_j) \Rightarrow \begin{cases} \mathbf{p}_t(x_i,y_j) = \mathbf{p}_A(x_i,y_j) \\ \mathbf{s}(x_i,y_j) = 0 \end{cases} \tag{2-9}$$

for the adhesion zone (slips are zero) and

$$\text{if} \qquad \left\|\mathbf{p}_A(x_i,y_j)\right\| > \mu p_n(x_i,y_j) \Rightarrow \begin{cases} \mathbf{p}_t(x_i,y_j) = \mu p_n(x_i,y_j)\mathbf{p}_A(x_i,y_j) / \left\|\mathbf{p}_A(x_i,y_j)\right\| \\ \mathbf{s}(x_i,y_j) = \dfrac{LV}{\Delta x(y_j)}\left(\mathbf{p}_t(x_i,y_j) - \mathbf{p}_A(x_i,y_j)\right) \end{cases} \tag{2-10}$$

for the slip zone.

Iterating the procedure for $2 \le i \le n_x$ and successively for $1 \le j \le n_y$ and assuming as boundary conditions $\mathbf{p}_t(x_1,y_j) = 0$ and $\mathbf{s}_t(x_1,y_j) = 0$ for $1 \le j \le n_y$ (i.e. stresses and creepages zero out of the contact patch), the distribution of $p_n(x_i,y_j)$, $\mathbf{p}_t(x_i,y_j)$ and $\mathbf{s}(x_i,y_j)$ can be calculated.

One can refer to literature for a more detailed description of the FASTSIM algorithm [30].

2.3.2. The wear evaluation

In this Ph.D. work the T-gamma approach for the wear evaluation according to [8][16] has been followed. It makes use of an experimental law to directly connect the power dissipated at the contact (measured by the Wear Index I_W) to the amount of material removed by wear (measured by the Wear Rate K_W). Among all the possible wear mechanisms occurring at the wheel-rail interface, such wear law takes into account abrasive wear and is based on an energetic approach. The two indexes are correlated by means of a heuristic law based on dedicated experimental wear tests [8][16]. Such tests have been performed under specific and controlled laboratory conditions which, sometimes, could differ from the reality due to system uncertainties, environmental conditions, use of lubrication systems, etc. In [8][16], the case of metal to metal contact is considered (R8T steel for the wheel and UIC60 900A for the rail, widely used in European and Italian network), using a twin disc test-rig arrangement under dry contact conditions. The test-rig was able to apply vertical and lateral loads on the discs and the sliding between the discs could vary in the range 0.2 – 20%. Finally, the temperature during the tests was kept constant. This experimental relationship allows to evaluate the specific volume of removed material on wheel and rail (expressed in $mm^3/(m \cdot mm^2)$) $\delta_{P^j_{wi(t)}}(x,y)$ and $\delta_{P^j_{ri(t)}}(x,y)$ (x and y indicate the coordinates of a generic point inside the contact patch) associated to the i-th contact points $P^j_{wi}(t)$ and $P^j_{ri}(t)$ on the j-th wheel and rail pair for unit of distance travelled by the vehicle (in m) and for unit of surface (in mm^2). More in details, the wear index I_W (a measure of frictional power dissipated at the contact for unit of area and normalized by the vehicle velocity), expressed in N/mm^2, is evaluated considering the local tangential contact pressure $\mathbf{p}_t$ and creepages $\mathbf{s}$:

$$I_W = \mathbf{p}_t \bullet \mathbf{s} / V \tag{2-11}$$

where V is the vehicle longitudinal speed. The wear index can be experimentally [16] correlated to the wear rate K_W, which is the mass of removed material (expressed in $\mu g/(m \cdot mm^2)$) for unit of distance travelled by the vehicle and for unit of surface. The experimental relationship between K_W and I_W is the following (see also Fig. 12):

$$K_W(I_W) = \begin{cases} 5.3 * I_w & I_W < 10.4 \\ 55.1 & 10.4 < I_W < 77.2 \\ 61.9 * I_W - 4723.7 & I_W > 77.2 \end{cases} \tag{2-12}$$

The law above also includes the fact that a big part of the frictional power dissipated at the contact transforms into frictional heat. In fact, the frictional power dissipated at the contact is directly correlated by the heuristic wear law to the material removed by wear measured experimentally. Consequently, only the part of the frictional power involved in the wear process is considered by the law and there is no risk of overestimating the wear on the contact surfaces.

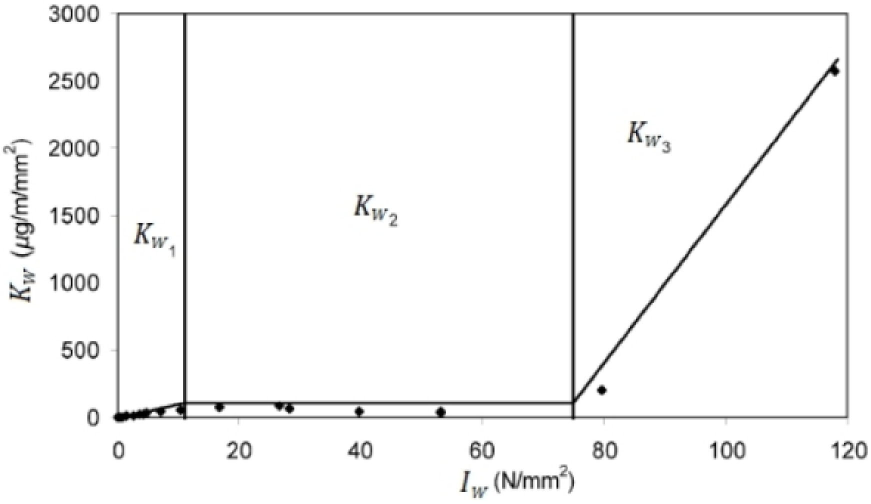

Fig. 12 Wear rate trend [8][16]

Once the wear rate $K_W(I_W)$ is known (the same both for the wheel and for the rail), the specific volume of removed material on the wheel and on the rail (for unit of distance travelled by the vehicle and for unit of surface) can be calculated (expressed in mm^3/(m·mm^2)):

$$\delta_{P^j_{wi(t)}}(x,y) = K_W(I_W)\frac{1}{\rho}$$

$$\delta_{P^j_{ri(t)}}(x,y) = K_W(I_W)\frac{1}{\rho} \tag{2-13}$$

where ρ is the material density.

2.3.3. The profiles update

After the worn material evaluation, wheel and rail profiles require to be updated before to be used as the input of the next discrete step of the process. The update strategy requires some integration and average operations in order to remove the numerical noise affecting the distributions $\delta_{P^j_i(t)}(x,y)$ and to calculate the total quantities of removed material due to wear $\Delta^w(s_w)$, $\Delta^r(s_r)$ (in mm), where s_w and s_r are the natural abscissas of wheel and rail profiles. Briefly, these operations can be summarized as follow:

- spatial integration along the longitudinal direction of all the wear contributions inside the contact patch and average over the whole longitudinal development of the wheel and of the rail;

- time integration of all the wear contributions coming from the dynamic simulation and sum on all the contact points;

- sum on the left and right wheel-rail pairs to get the total amount of rail wear (obviously this step is not required for the wheel).

By going into the detail:

- *Longitudinal integration*

All the wear contributions inside the contact patch are summed along the longitudinal direction and this quantity is averaged over the whole longitudinal development of the wheel and of the rail (by means of the factors $1/2\pi w\left(y_{wi}^{j}\right)$ and $1/l_{track}$):

$$\frac{1}{2\pi w\left(y_{wi}^{j}\right)}\int_{-a(\mathrm{y})}^{+a(\mathrm{y})}\delta_{P_{wi}^{j}(t)}(x,y)\mathrm{dx}=\delta_{P_{wi}^{j}(t)}^{tot}(y)$$

$$\frac{1}{l_{track}}\int_{-a(\mathrm{y})}^{+a(\mathrm{y})}\delta_{P_{ri}^{j}(t)}(x,y)\mathrm{dx}=\delta_{P_{ri}^{j}(t)}^{tot}(y) \tag{2-14}$$

where $w\left(y_{wi}^{j}\right)$ is the wheel radius evaluated in y_{wi}^{j} and l_{track} is the length of the simulated curve section.

- *Track integration*

This integration *over the track length* adds all the wear contributions coming from the dynamic simulation to calculate the depth of removed material (in mm=mm^3/mm^2) on wheel and rail:

$$\int_{T_{in}}^{T_{end}}\delta_{P_{wi}^{j}(t)}^{tot}(y)V(t)dt\approx\int_{T_{in}}^{T_{end}}\delta_{P_{wi}^{j}(t)}^{tot}(\mathrm{s}_w-\mathrm{s}_{wi}^{cj}(\mathrm{t}))V(t)dt=\Delta_{P_{wi}^{j}}(\mathrm{s}_w)$$

$$\int_{T_{in}}^{T_{end}}\delta_{P_{ri}^{j}(t)}^{tot}(y)V(t)dt\approx\int_{T_{in}}^{T_{end}}\delta_{P_{ri}^{j}(t)}^{tot}(\mathrm{s}_r-\mathrm{s}_{ri}^{cj}(\mathrm{t}))V(t)dt=\Delta_{P_{ri}^{j}}(\mathrm{s}_w) \tag{2-15}$$

The natural abscissas s_w and s_r of the curves $w(y_w)$ and $r(y_r)$ have been considered to have a better accuracy in the calculation of the worn profiles, especially in the flange zone and in the rail flank where the slope is steeper, (see Fig. 13).

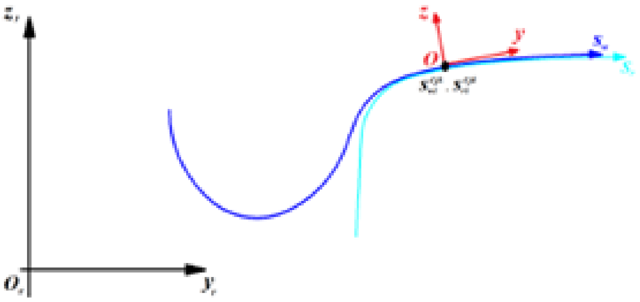

Fig. 13 Normal abscissa for the wheel profile

- *Sum on the contact points*

All the wear contributions of each contact point are summed as follows:

$$\sum_{i=1}^{N_{PDC}} \Delta_{P_{wi}^{j}}(s_w) = \Delta_j^w(s_w)$$
$$\sum_{i=1}^{N_{PDC}} \Delta_{P_{ri}^{j}}(s_r) = \Delta_j^r(s_r) \qquad (2\text{-}16)$$

where N_{PDC} is the maximum number of contact points of each wheel and of each single rail, respectively. The number of contact points that appear during the dynamic simulation changes in the time and it has been assumed that the contribution to wear associated to the fictitious points is zero.

- *Sum on the right and left wheel-rail pair to evaluate rail wear*

The sum on right and left vehicle wheel-rail pairs is calculated to properly get the total rail wear:

$$\sum_{j \in \text{left/right wheel}}^{N_w} \Delta_j^r(s_r) = \Delta_{l/r}^r(s_r) \qquad (2\text{-}17)$$

where N_w is the number of vehicle wheels. This operation is not required for the calculation of wheel wear.

- *Scaling*

Since normally travelled distances of thousands of kilometres are needed to obtain measurable wear effects, an appropriate scaling procedure is required to reduce the simulated track length with a consequent lighter computational effort.

Furthermore, the wheels wear out much faster than the rails. Consequently, it is necessary to implement different strategies to update the wheel and rail profiles: the total mileage km_{tot} travelled by the vehicle is considered for the wheel, which is then subdivided into constant steps of length km_{step} ; on the contrary, for the rail update, the total tonnage burden on the track M_{tot} (and then the total number N_{tot} of vehicle running on the line) is taken into account (see Fig. 14). As in the wheel case, the total number N_{tot} of vehicle operating on the line is subdivided into constant steps equal to N_{step} .

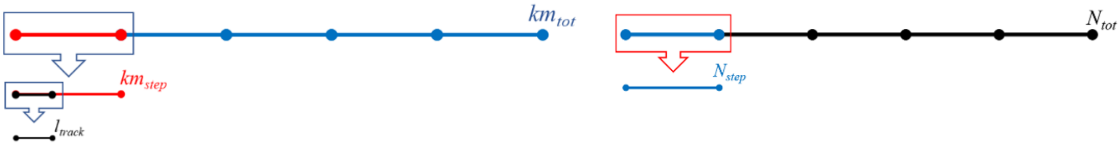

Fig. 14 Discretization of the mileage and the total vehicle number

In this research, an adaptive strategy has been chosen to update the wheel and rail profiles since it fits well in following the behaviour of the wear evolution that may present non-linear characteristics outside the discrete steps. The approach imposes a threshold value on the maximum of the removed material at each discrete step of the procedure. The evaluation of the discrete steps, represents the major difference between the update strategy of wheel and rail:

- The removed material on the wheel is proportional to the distance travelled by the vehicle. Thus, the material removed on the wheel has to be scaled according to the following law:

$$\Delta_j^w(s_w)\frac{km_{step}}{l_{track}} = \Delta_j^{wsc}(s_w) \qquad (2\text{-}18)$$

where km_{step} is calculated in an adaptive way setting a threshold value $D^{w}{}_{step}$ on the maximum of the removed material quantity on the wheel at each discrete step (see Fig. 14):

$$km_{step} = l_{track} * \frac{D^{w}{}_{step}}{\max(\Delta_j^w(s_w))} \tag{2-19}$$

where $\max(\Delta_j^w(s_w))$ corresponds to the maximum value of wear depth obtained from the simulation before the scaling operation and l_{track} is the mileage travelled by the vehicle during the dynamic simulations.

- Instead, for the rail, the wear is proportional to the total tonnage burden on the track M_{tot} and thus to the total number of vehicles operating on the line N_{tot} (see Fig. 14). Therefore, if N_{step} is the number of vehicles running in a discrete step, the quantity of removed material on the rail at each step will be:

$$\Delta_{l/r}^{r}(s_r) * N_{step} = \Delta_{l/r}^{rsc}(s_r) \tag{2-20}$$

where N_{step} is calculated in an adaptive way imposing a threshold value $D^{r}{}_{step}$ on the maximum of the removed material quantity on the rail at each discrete step:

$$N_{step} = \frac{D^{r}{}_{step}}{\max(\Delta_{l/r}^{rsc}(s_r))} \tag{2-21}$$

Therefore, the total tonnage burden on the track during the whole simulation is calculated multiplying the mass of the single vehicle M_v by the total vehicle number:

$$M_{tot} = N_{tot} * M_v \tag{2-22}$$

- *Profile update*

Finally, after a smoothing process on the removed material function, necessary to reduce the numerical noise, the new profiles $w_n(s_w)$ and $r_n(s_r)$ are gotten removing the worn material $\Delta^{wsc}_{j,sm}(s_w)$ and $\Delta^{rsc}_{r/l,sm}(s_r)$ along the normal direction (where the subscript sm indicates that the profiles have been smoothed and $\mathrm{n}^{\mathrm{r}}_{\mathrm{w}}$, $\mathrm{n}^{\mathrm{r}}_{\mathrm{r}}$ are the outgoing unit vectors for the wheel and rail profile) to the wheel and rail old profile $w_o(s_w)$ and $r_o(s_r)$:

$$\begin{pmatrix} y_w(s_w) \\ w_o(s_w) \end{pmatrix} - \Delta^{wsc}_{sm}(s_w)\mathbf{n}^r_w \Rightarrow \begin{pmatrix} y_w(s_w) \\ w_n(s_w) \end{pmatrix}$$

$$\begin{pmatrix} y_r(s_r) \\ r_o(s_r) \end{pmatrix} - \Delta^{rsc}_{sm}(s_r)\mathbf{n}^r_r \Rightarrow \begin{pmatrix} y_r(s_r) \\ r_n(s_r) \end{pmatrix} \tag{2-23}$$

The new updated profiles are then fed back as inputs to the vehicle model and the whole model architecture can proceed with the next discrete step of the process where a new dynamic simulation and a new profile updating procedure are carried out.

Because of the different scales of magnitude, the wear evolution on wheel and rail has been decoupled (see Fig. 15). In particular, since its variation due to wear is negligible in the considered time scale, the rail is supposed to be constant while the wheel wear evolves. On the other hand, each discrete rail profile comes in contact, with the same frequency, with each possible wheel profile. Then, the whole wheel wear evolution (from the original profile to the final one) has been simulated inside each rail step.

More specifically, in the first discrete rail step p_1, the wheel, starting from the unworn profile w_o^0, evolves on the unworn rail profile r_o up to produce the discrete wheel profiles w_o^1, w_o^2, . . ., w_o^n. Then the virtual rail profiles r_o^0, r_o^1, etc... obtained by running each different wheel profile w_o^1, w_o^2, . . ., w_o^n on the initial unworn rail profile r_o, are arithmetically averaged to obtain the updated rail profile r_1, used as input in the next discrete rail step. This procedure can be repeated *m* times in order to perform all the rail steps (see Fig. 15).

Then, the computational effort required by the simulation strategy is the following:

- To study wheel wear, inside each rail step p_j (*m* updates), the whole wheel wear loop w_o^i (with i from 1 to *n* steps of simulation) is simulated. The computational effort results in $n{\times}m$ steps both for the dynamic analysis (in Simpack software) and for the wear model necessary to calculate the removed material on the wheel (in Matlab).

- In the rail wear study the dynamic analyses are the same of the previous case because for each rail step the wheel profiles w_0^i are simulated on the r_j rails in order to obtain r_j^i and thus the updated rail profile r_{j+1} by means of an arithmetic mean. Therefore, no additional dynamical analyses are needed.

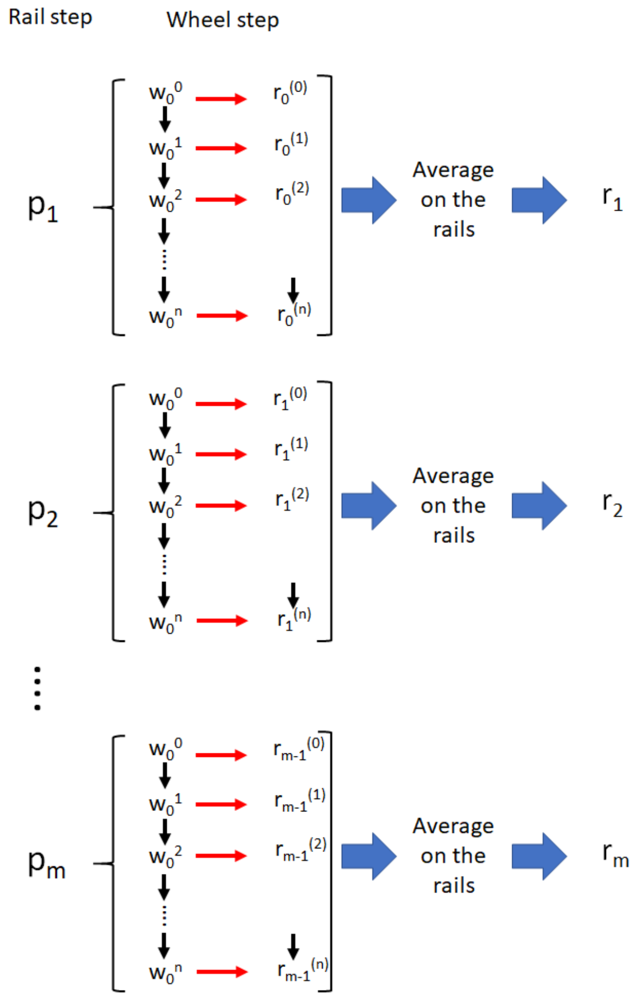

Fig. 15 Simulation strategy

3. Rolling contact fatigue: state of the art and current work

In this Chapter, firstly, the deterioration mechanism of the rolling contact fatigue will be discussed through a brief description of the main causes and modelling approaches proposed over the years. Then, the second part of the Chapter will be focused on the detailed description of the proposed model and on the experimental calibration of the RCF law.

3.1. RCF defects

To better understand the main causes behind this damage mechanism, a short preamble on what occurs at wheel-rail contact interface could be useful.

The train wheels have a conical shape. In this way it is possible to obtain a sort of differential effect while the vehicle is running through a curve. A rolling radius difference results from a lateral shift of the wheelset: the rolling radius of the inner wheel decreases and that of the outer increases with the consequence that the outer wheel would be roll faster than the inner one. Considering an isolate wheelset, this difference could be enough to compensate the difference in length between the rails and pure rolling condition are achieved. It means that no friction forces at wheel-rail contact will born. Combining more than a wheelset inside a bogie, each wheelset influences the others and the radially self-alignment in most cases is not possible resulting into a relative motion between the surfaces of wheel and rail. This sliding motion is known as creepage (defined as sliding velocity/vehicle speed) and leads to a generation of lateral and longitudinal creep forces at the contact opposite to relative motion. In general, a contact patch is divided in an adhesion where no slip occurs and a sliding zone where the tangential stress is higher since the friction coefficient is saturated (see Fig. 16). Obviously, the total transmitted force increases with the sliding area until the ratio of tangential to normal force reaches the coefficient of friction and the whole contact area is in sliding. As is well know from the Hertz theory, under the hypothesis of a non-conformal contact, the contact takes place over an elliptic area, due to the elasticity of the material, which depends on the normal applied load and profile geometry. Over this area a part of the contact will be sticking and part of it will be sliding (Fig. 16). This setting allows the establishment of a cyclic tangential stress between the two areas during the contact which summed up with the Hertzian loads, results in cyclic fatigue within the material, also known as Rolling Contact Fatigue. It may lead to crack formation, propagation, and, eventually, components failure.

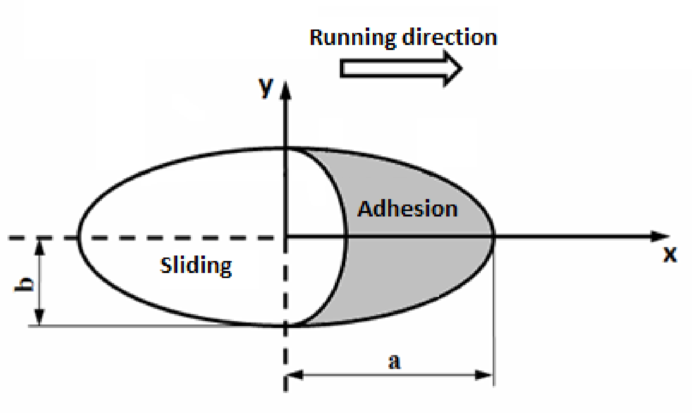

Fig. 16 Contact patch: adhesion and sliding zone

Rolling contact fatigue behaviour is a crucial aspect for safety since it leads to catastrophic and unpredictable breaks of the rail surface and derailment. The loss of a piece on the rail head of a few millimetres may be sufficient to cause a derailment. RCF is mainly affected by loads, sliding, properties of the steel and surface defects.

Many types of RCF defects have been reviewed over several years of investigation. A comprehensive and exhaustive review can be found in [48][49]. The main types of RCF defects can be summarized as follows:

- *Head checks*: it initiates at the surface on the rail head and it is caused by combination of normal and tangential stresses (see Fig. 17). High load and high friction are the conditions under which this happens. This exists primarily in switch and crossing work and on the high rail in curves.

- *Rail Gauge Corner Cracking*: thin cracks on the gauge corner of the rail observable most often on the outer rails of curves and sometimes on tangent rails (see Fig. 18). They grow as a result of high wheel-rail contact stresses combined with sufficiently large shear stresses due to slip between wheel and rail. As the crack grow up, the defect become longer and deeper and may eventually lead to pits and shells on the rail surface.

- *Tache ovales:* they develop inside the railhead from cavities formed by hydrogen, especially in welded zones (see Fig. 19).

- *Wheel Tread and Flange Cracking*: a wheel experiences many different load condition (different speeds and curves, traction and braking maneuver) compared to a rail. The highest creep forces on the wheels usually occur on the leading axle while it is running a curve. The rolling contact fatigue defect on wheel goes in parallel with that on the rail: an excessive cyclic shear stresses may cause a plastic flow and when the total strain exceeds the ductility limit, a crack appears. Different types of damage on wheel are visible in Fig. 20.

- *Wheel Spalling:* when a wheel slides on the rail the temperature at the wheel-rail contact increases, often rising the transition temperature of pearlitic steel (723°C). Then, due to wheel rolling motion, the contact patch cools very quickly leading to a formation of a white-phase martensite. This martensite is very brittle and cracks when the wheel rolls over it (see Fig. 21).

- *Rail and Wheel Shelling*: is the loss of large debris of metal due to the connection of surface or subsurface cracks with other cracks below the surface or caused by excessive loading (see Fig. 22).

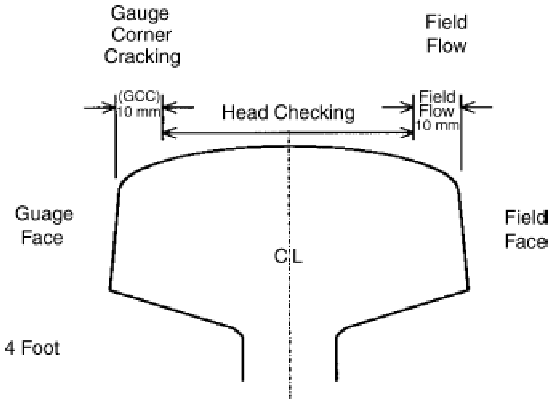

Fig. 17 Head Checking (HC) and gauge corner cracking (GCC) [48]

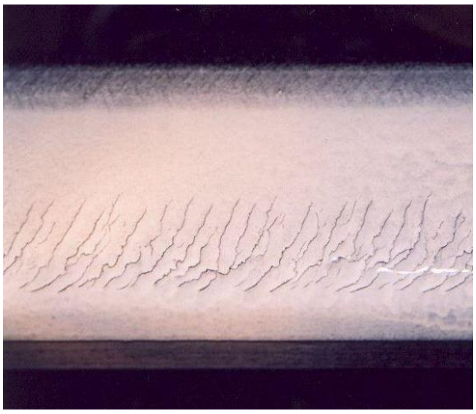

Fig. 18 Gauge Corner Cracking (GCC) [49]

Fig. 19 Breaks from a “tache ovale” [48]

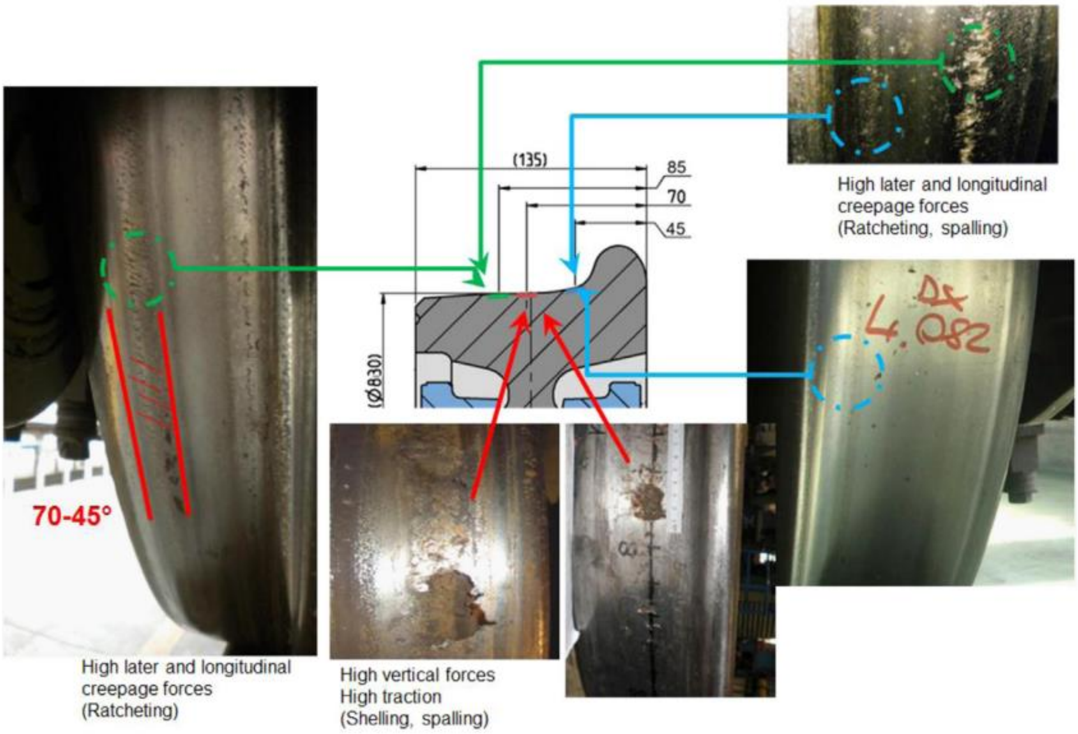

Fig. 20 RCF damage on wheel [48]

Fig. 21 Wheel spalling [48]

Fig. 22 Rail shelling [48]

3.2. RCF mechanisms

In the rolling contact patch takes place a transmission of high loads over a small contact area resulting in very high and cyclic stresses. A crack may initiate at the surface, just below the surface or inside the component if a pre-existing defect is present. If a crack initiates or not, it depends on the response of a material to cyclic loading.

3.2.1. Cyclic Fatigue and material responses

With reference to Fig. 23, a material loaded repeatedly may show four different responses or deformation levels [43] :

a) *Perfectly elastic:* if the maximum stress does not exceed the yield stress σ_Y . No plastic flow and permanent deformations occur, and the material may fail by High Cycle Fatigue.

b) *Elastic shakedown:* when the yield stress is exceeded, but the load is under the elastic shakedown limit σ_{el}, there is plastic flow but the response returns elastic after some cycles due to residual stresses and material hardening. Residual stress makes plastic flow less likely during following loading cycles. This effect is known as “shakedown” or “work hardening”. Then, the material may fail by High Cycle Fatigue also in this case.

c) *Plastic shakedown:* if the cycles of plastic stress-strain occur without accumulating plastic deformation (close cycles), also known as linear kinematic plasticity. The material will eventually fail by Low Cycle Fatigue.

d) *Ratchetting:* when the load cycle is above the plastic shakedown limit σ_{pl}, a plastic strain accumulation takes place every new cycle (non-linear cinematic hardening). Plastic ratchetting, basically a directional accumulation of strain, alters the microstructure of the material to the point that in the near-surface region it is severely deformed and subjected to swiftly variable triaxial stresses.

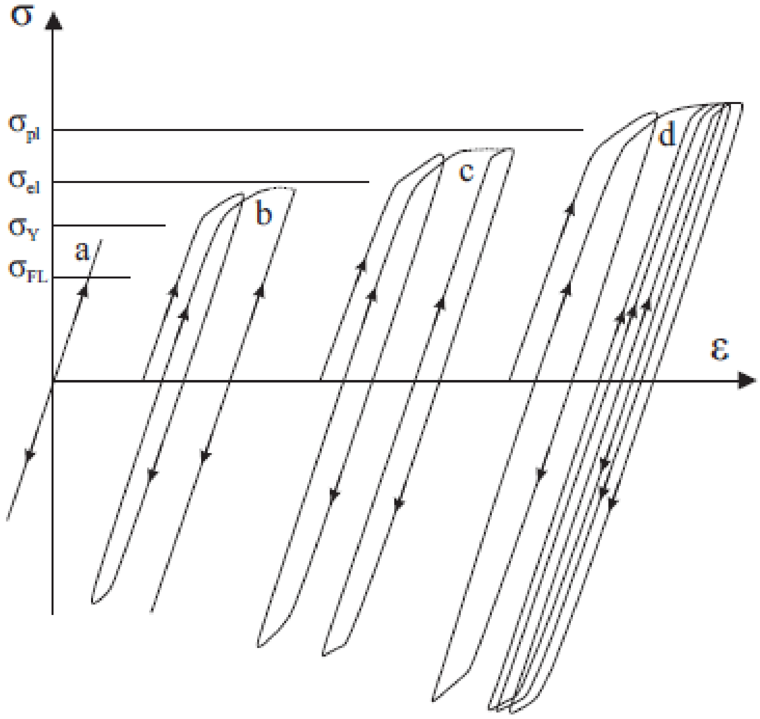

Fig. 23 Material response to cyclic loading [46]

Then, there is the so-called 'shakedown limit' for which, if exceeded, permanent plastic deformation occurs for each subsequent wheel revolution until surface cracking. This process is known as ratchetting.

The stresses coming from Hertzian and creepage forces, previously described, and tractive forces significantly increase the surface shear stresses and with them the probability of exceeding the shakedown limit, facing hardening and ratchetting.

3.2.2. Crack initiation

Rolling Contact Fatigue cracks generally originates from the surface or just underneath it, depending on the operating conditions and material properties. This is usually related to cyclic plasticization (stress above the elastic shakedown). The plasticization of the material in cyclic contact happens on different deformation levels: in ratchetting regime, unidirectional plastic deformations cumulate progressively as load cycle number increase. Under the conditions of high friction and high contact stress (see ratcheting region on the shakedown map in Fig. 24), the wheel and rail metal deforms in the direction of the applied stress and the accumulation of deformation leads to ratchetting of the surface. Although the effective strength of the material is increasing progressively because of strain hardening, it cannot strain indefinitely and a surface crack appears. Then, cracks nucleate inside the material when a critical accumulated plastic strain is reached. Now the cracks can grow parallel to the surface, giving rise to a phenomenon called “delamination wear”, or they can grow towards the core, determining the RCF phenomena. Cracks developed as a result of ratchetting usually grow down to a depth corresponding to one of the layers subjected to forward plastic flow. It is nearly always the case that micro-cracks originated from surface defects are present in railway materials since the early load cycles. They tend to develop near to the flange and in the external side of the tread and are the main cause of shelling: these cracks can be easily stopped by wear. Macro-cracks are the ones generated by cyclic plasticization and if shakedown limit is exceeded, these could be dominant and micro-cracks can be overlooked.

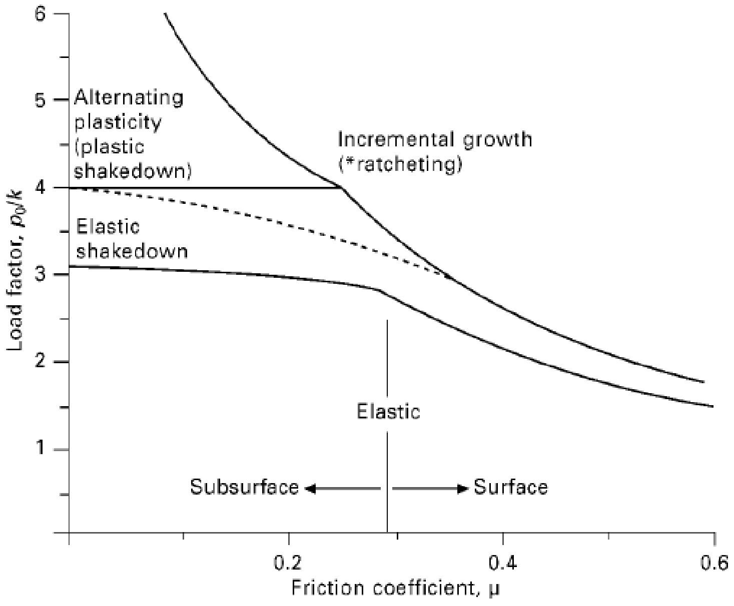

Fig. 24 Shakedown map [43]

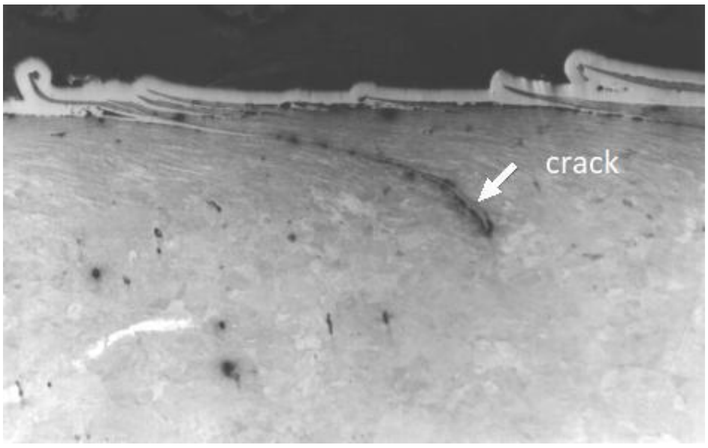

Fig. 25 Ratchetting and crack initiation [49]

3.2.3. Crack propagation

Once the crack nucleates due to rolling contact fatigue inside the material, its growth, driven by ratchetting, can be split into three phases [43]:

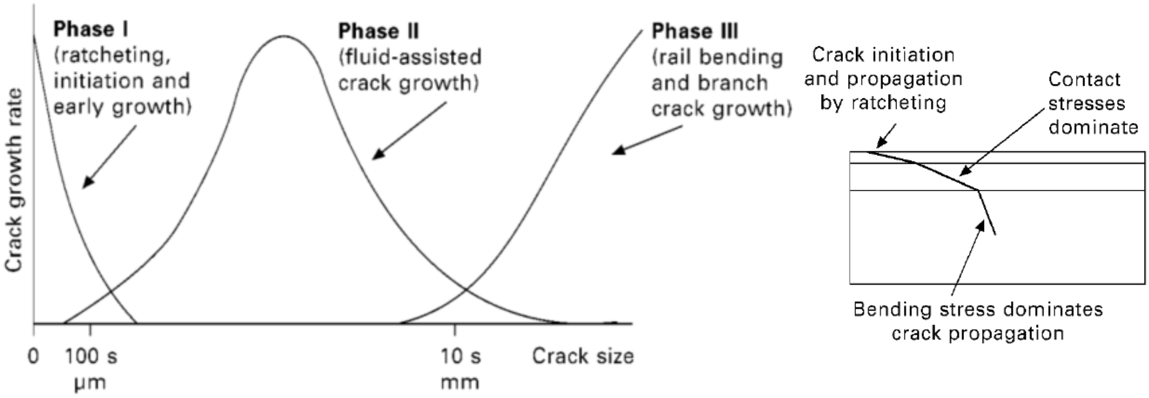

Fig. 26 Ratchetting and crack initiation [49]

- Phase I: defects are in the order of hundreds of microns in size and they are mainly localized in the deformed near-surface. The deformation process starts.

- Phase II: is characterized by the growth of the crack mainly under the effect of fluid entrapment (see Fig. 27). As crack become longer, stresses near to crack tip increase as the crack growth rate. Overcome a certain critical length, the tip of the longest crack moves away from the higher contact stress zone leading to a reduction of crack growth rate.

- Phase III: the crack growth rate increase since once the crack is large its propagation is driven by bending stresses.

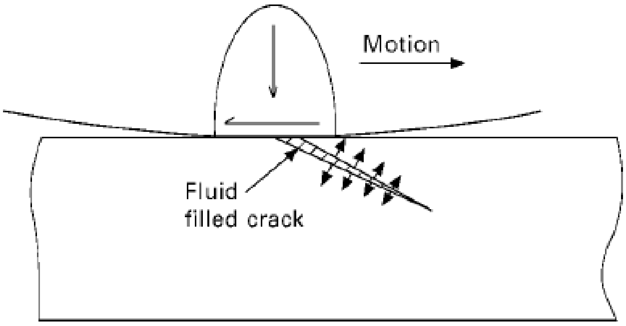

Fig. 27 Fluid entrapment [49]

3.2.4. Wear and RCF interaction

Wear and RCF are competitive mechanisms: wear remove surface layers where cracks are growing. However, this competition is very complex, involving other phenomena, as material hardening, liquid body trapping, residual stresses. With reference to Fig. 28(a) the crack is truncated as more and more material is removed by wear. If the wear rate is higher than the crack growth, than it is most likely that every crack will be worn away. This equilibrium between wear and rolling contact fatigue is the basis of the “magic wear rate” where crack formation is compensated by wear [49]. In Fig. 28(b), a low and a high wear rates are considered.

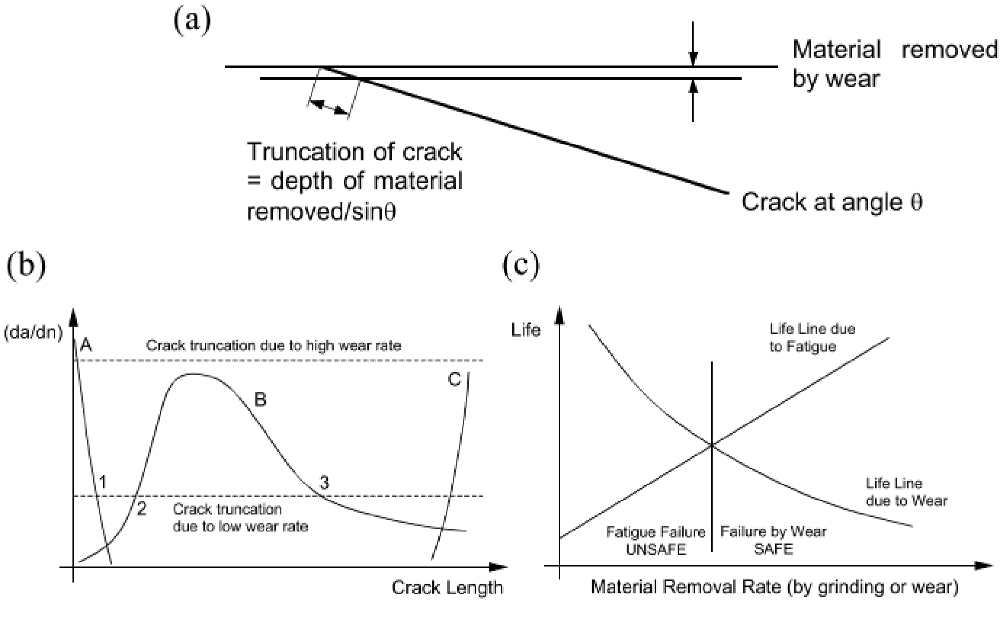

Fig. 28 Wear vs fatigue. a) crack truncation; b) grow rate vs crack length; c) rail life vs removal rate [49]

If the wear rate is high, most cracks will be worn off before proceeding to Stage A, where cracks are driven by ratcheting. If the wear rate is low, crack may progress to Point 1, where truncation rate and growth rate are equals. If contact condition changes, it is possible that the crack may be could pass from point 1 to 2 and propagate through stage B until point 3 where crack length at which the growth rate declines is reached. If the wear rate falls below the intersection of Stages B and C the crack can move to Stage C, leading to a component failure. In Fig. 28(c) wear and fatigue life curves are plotted together. A wear failure is preferred, from a safety point of view but an excessive wear is problematic for wheel and rail profiles, resulting in higher contact stresses and maybe in higher wear and more RCF problems. The wear rate may be reduced using harder rails and lubrication. However, this means brittle material, more prone to crack initiation, and the presence of fluid that enhance the crack propagation.

3.3. RCF modelling approaches

Several models for this process have been developed over the years [10][14][17][20][21][22] but two main approaches can be found: models based on finite element analysis and models exploiting empirical laws. Despite their high accuracy, the models of the first group [9][10][11][12] are critical in terms of computational efficiency and are too complex to be used in large scale multibody dynamic simulations of railway networks. Finite element models are used to determine the stress intensity factors for the different modes of crack growth but, as explained in [13], this is a challenging task since the multi-axial loads and the changes in direction of the principal stresses.

Concerning the second group, in general, two lines of research are present in the literature to model crack initiation and growth. The first one makes use of the "shakedown limit", a popular model for RCF initiation, to calculate the tangential stresses above which the crack appears. Ekberg et al. [18][17] propose a surface fatigue index (*FIsurf*) depending on the load factor k/p_0 (where p_0 is the maximum contact pressure and k the material yield stress in shear) and on the friction coefficient μ (see also Fig. 24). If $FIsurf>0$ a crack initiates. On a shakedown diagram, *FIsurf* can be seen as the horizontal distance from working point to the shakedown limit (see Fig. 29). If contact conditions are above the shakedown limit, then RCF can be appear. A disadvantage of this approach is that the contribution of wear is not taken into account and it needs to be coupled with a wear model to combine these two damage mechanisms.

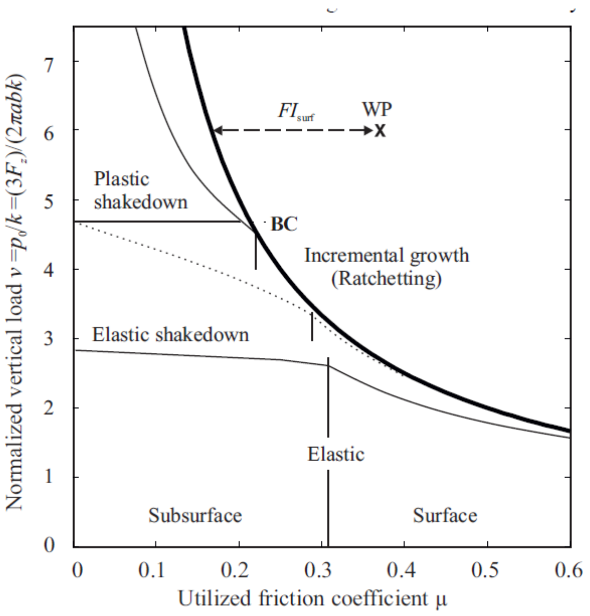

Fig. 29 FIsurf on the shakedown diagram [18]

Another method to determine crack initiation is the Whole Life Rail Model - WLRM - by Burstow [17] preliminary developed for the rail but used also for wheels. This method adopts a frictional energy based approach (in a similar way to some wear models), including the effect of wear on RCF damage. Burstow has developed a RCF damage model that combines the longitudinal and lateral creep force and creep (as in equation (2-2)) to calculate $T\gamma$. Then the RCF damage depends on the values of $T\gamma$. With reference to Fig. 30 for $T\gamma<15\ \mathrm{N}$ no surface damage occurs. For $15\ \mathrm{N}<T\gamma<65\ \mathrm{N}$ RCF damage increases linearly with $T\gamma$. For $T\gamma>65\ \mathrm{N}$, wear begins to prevail on RCF damage. For $T\gamma>175\ \mathrm{N}$, the wear rate is higher than the crack growth rate and no RCF damage occurs. The main disadvantage of this model is that the values of the damage function has been calibrated for a particular type of rail material in service on the Network Rail infrastructure, so a new recalibration may be necessary to apply the model to other applications. The main advantage is that includes the effect of wear on RCF.

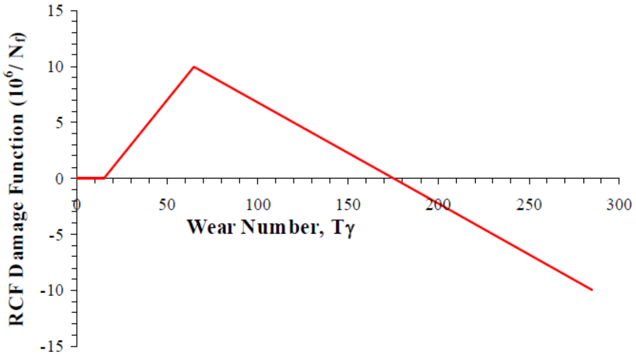

Fig. 30 WRLM damage function [17]

The approaches described above have the main disadvantage that they are not able to evaluate the crack length/depth and, consequently, the damage level; they only determine if the RCF damage occurs. In developing of a tool for wheel and rail damage assessment, a RCF prediction model to determine crack initiation and a fatigue based model which correlates the RCF damage to crack dimensions should be coupled. This RCF prediction tool will be less accurate than the model where the crack growth is modelled by FEM but faster, allowing to be implemented in combination with vehicle dynamics simulations.

As described in 3.2.3, crack propagation can be divide in three phases and two modelling approaches can be found in literature to describe surface initiated crack growth: *fracture mechanics* and *fatigue damage approach*.

According to fracture mechanics theory, a crack propagates in three different modes [50][43] as shown in Fig. 31: opening, shearing, tearing. In mode I the applied load pulls apart the crack faces is the tensile opening mode, while in mode II faces are sheared backwards and forwards and in mode III faces are sheared sideways. A crack on a rail will experience a combination of these, although most cracks are modellable with the first two modes. Which mode is dominant depends on the size, if a fluid entrapment is present and if a rail or a wheel is considered. The crucial parameter in crack growth's fracture mechanics is the stress intensity factor (SIF), which takes account of the stresses applied, the body shape and the crack shape.

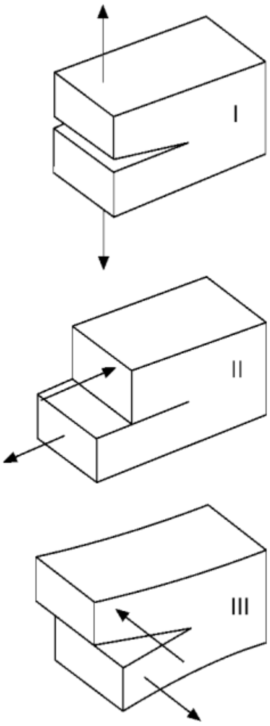

Fig. 31 Fracture mechanics mode [43]

This stress intensity factor must then be converted in a growth rate through a crack growth law. In Paris's crack growth law, the growth of a crack under cyclic loading is:

$$\frac{da}{dN} = C\Delta K^{m} \quad (3\text{-}1)$$

where $\frac{da}{dN}$ is the growth rate (change in crack length per load cycle), ΔK is the stress intensity factor and C and m coefficients depending on materials. In [52] crack growth law has been developed after extensive testing using biaxial fatigue specimens of normal grade rail steel cut from the rail web obtaining:

$$\frac{da}{dN} = 0.000507(\Delta K_{eq}^{3.74} - 4^{3.74}) \quad (3\text{-}2)$$

where

$$K_{eq} = \sqrt{\Delta K_{I}^{2} + \left[\left(\frac{614}{507}\right)\Delta K_{II}^{3.21}\right]^{\frac{2}{3.74}}} \quad (3\text{-}3)$$

The stress intensity factor includes mode I (opening) and II (shearing) since these modes are predicted to act on the crack during wheel passage of a contact.

The fatigue damage approach [14][15][18] is based on a relationship (Basquin) which correlates the applied stress amplitude σ_a and the number of cycles to failure N_f:

$$\sigma_a = \alpha(N_f)^{\beta} \quad (3\text{-}4)$$

where α is the fatigue strength coefficient and β the fatigue strength exponent or Basquin exponent and are material parameters.

The fatigue damage for one single load cycle can be defines as follows:

$$D_i = 1/N_f \quad (3\text{-}5)$$

And substituting in (3-4) the damage for one cycle can be estimated. Then, to accumulate the damage the Palmgren-Miner rule is used:

$$D = \sum_{i=1}^{\text{n load cycle}} D_i \qquad (3\text{-}6)$$

which gives the total damage after n load cycles. If failure ($D = 1$) is assumed to be a certain crack length, the crack length can be calculated.

3.4. The current work: RCF prediction model

The rolling contact fatigue is a damage caused by repeated cyclic loading and unloading together with creep forces from curving, traction and braking that lead to crack initiation and propagation. Cracks may grow up to wheel or rail failure (increasing the maintenance costs), broken rails and derailments. Many previous studies [17][18][19] have shown as shear stresses and forces (resulting from sliding caused by nominal radius difference between inner and outer wheels and by the yaw angle of the wheelset when a train is running through a curve) are the main cause of cracks appearance and growth.

In this Ph.D. work, the shakedown theory and a “fatigue damage” approach [16][19] has been used to incorporate the RCF model into the wear model. The shakedown theory allows to separately evaluate wear and RCF damage, offering a more complete and exhaustive assessment of wheel and rail life. The main advantage of a fatigue damage approach compared to a fracture mechanics [23] is the significantly improved numerical efficiency (this approach can be also implemented into vehicle multibody models). The main disadvantage is that it is valid only for small cracks, because it ignores that the crack growth rate depends on the crack size. This issue may be overcome by setting a smaller and more refined discretization step of the whole iterative procedure (see Fig. 1). In the framework of the “fatigue damage” approach, a Basquin - like relationship to link the damage (in terms of crack initiation [23][24][25] and propagation [18][19]) to the load cycles have been developed. More in details, such RCF law links the shear stress and the load cycles to the crack length and has to be properly tuned through suitable test campaigns on test rigs. The proposed RCF model, based on such law, is able to predict the possible crack initiation and propagation (in terms of depth and length) along the whole wheel and rail profiles and, consequently, the spatial position of the possible cracks on the wheel and on the rail.

From an analytic viewpoint, as regards the crack propagation [19], the following relationship between the predicted crack length $c_{plP_i^j(t)}$ related to a single load cycle (in mm; the subscript pl indicates the predicted length, i.e. the length calculated by means of the RCF model) and the stress magnitude

$\sigma_t(y)$ (in MPa, at the time t and for the *i-th* contact points $P_{wi}^j(\mathrm{t})$ and $P_{ri}^j(\mathrm{t})$ of the j-th wheel and rail pair) has been considered:

$$c_{pP_i^j(t)}(y) = \frac{1}{\alpha(\mathrm{a}\,\sigma_t(y))^{\beta}} \tag{3-7}$$

where α and β are parameters to be calibrated and $\mathrm{a} = 1\ \mathrm{MPa}^{-1}$. According to (3-7), $c_{plP_i^j(t)}$ is the predicted contribution to the total crack length of one single load cycle. The cumulative effect of all the load cycles born by system during its life will be taken into account in the following of the procedure (see the section “Track Integration”).

Such relation will be tuned by means of specific fatigue tests carried out in the laboratory of the Tribology Research Institute of the Southwest Jiaotong University, using two rolling-sliding test machines (see section 3.5).

On the other hand, concerning the crack initiation [24][25], the stress index defined in (3-8) has been used to calculate the stress magnitude $\sigma_t(y)$ at each point of the discretized contact patch:

$$SI(x,y) = \max\left(\sqrt{p_{tx}(x,y)^2 + p_{ty}(x,y)^2} - k, 0\right) \tag{3-8}$$

where $p_{tx}(x,y)$ and $p_{ty}(x,y)$ are the components of the tangential pressure $\mathbf{p}_t = \left(p_{tx}(x,y), p_{ty}(x,y)\right)^T$ (the same used in the wear model) and k is the yield limit in shear of the material. Damage only occurs when $SI(x,y) > 0$ (N/m^2). The tangential pressures $p_{tx}(x,y)$ and $p_{ty}(x,y)$ correspond to the τzx and τzy components of the stress tensor evaluated at the wheel-rail interface (with the z-axis orthogonal to contact plane). Finally, the maximum value of $SI(x,y)$ in the longitudinal running direction (x direction) is taken as stress magnitude $\sigma_t(y)$:

$$\sigma_t(y) = \max_{\mathrm{x}}(SI(x,y)) \tag{3-9}$$

The RCF model is implemented in parallel to the evaluation of the material removed by wear and its inputs are the same of the wear model: contact stresses, contact creepages and calculated wear. The influence of wear on the crack growth is taken into account at the end of the RCF calculation. More specifically, the two models run in parallel and interact at the end of each process step, combining the depth of removed material by wear and the crack depth to correctly consider the effect of the wear rate on the crack growth (see equation (3-18) at the end of this section).

After obtaining the stress magnitude $\sigma_t(y)$, the same procedure used in the wear model for the wheel and rail profiles update [1][2] has been exploited in the RCF model to update the crack length and depth at each step of the whole iterative procedure (see Fig. 1). In particular the procedure consists of the following steps:

- *Average on the wheel and rail longitudinal length*

The predicted crack length is averaged over the whole longitudinal development of the wheel and of the rail by means of the factors $1/2\pi w\left(y_{wi}^j\right)$ and $1/l_{track}$:

$$\frac{1}{2\pi w\left(y_{wi}^j\right)} c_{pP_i^j(t)}(y) = c_{pP_{wi}^j(t)}(y)$$

$$\frac{1}{l_{track}} c_{pP_i^j(t)}(y) = c_{pP_{ri}^j(t)}(y) \tag{3-10}$$

where $w\left(y_{wi}^j\right)$ is the wheel radius evaluated in y_{wi}^j and l_{track} is the length of the simulated track. It is equivalent to the complete track length if the whole length of the railway/tramway network is considered or to the length of a curve if the study is focused on a single specific curve. According to this assumption, the crack distribution on the wheel and on the track is supposed to be uniform in the longitudinal direction. In other words, the probability of crack appearance and the growth dynamics of the crack are basically the same along the longitudinal direction.

- *Track integration*

The track integration sums all the contributes to the crack length coming from the dynamic simulation (integration on the whole track length l_{track}):

$$\int_{T_{in}}^{T_{end}} c_{pP_{wi}^j(t)}(y)V(t)dt \approx \int_{T_{in}}^{T_{end}} c_{pP_{wi}^j(t)}(\mathrm{s}_w - \mathrm{s}_{wi}^{cj}(\mathrm{t}))V(t)dt = C_{pP_{wi}^j}(\mathrm{s}_w)$$

$$\int_{T_{in}}^{T_{end}} c_{pP_{ri}^j(t)}(y)V(t)dt \approx \int_{T_{in}}^{T_{end}} c_{pP_{ri}^j(t)}(\mathrm{s}_r - \mathrm{s}_{ri}^{cj}(\mathrm{t}))V(t)dt = C_{pP_{ri}^j}(\mathrm{s}_r) \tag{3-11}$$

where s_w and s_r are the natural abscissas of the profiles $w(y_w)$ and $r(y_r)$ while s_{wi}^{cj} and s_{ri}^{cj} are the natural abscissas of the contact points. This track integration allows to take into account all the load cycles born by the system.

- *Sum on the contact points*

To have as output a single crack distribution along the wheel and rail profiles, all the RCF contributions of each contact point of the j-th wheel-rail pair are summed as follows:

$$\sum_{i=1}^{N_{PDC}} C_{pP^j_{wi}}(s_w) = C_{Lj}^{\;w}(s_w)$$

$$\sum_{i=1}^{N_{PDC}} C_{pP^j_{ri}}(s_r) = C_{Lj}^{\;r}(s_r) \tag{3-12}$$

According to this assumption, all the contact points of each wheel-rail pair contribute the same way to the crack growth.

- *Average on the wheel-rail pairs to calculate the rail crack length*

As regards the rail, since all the wheels contribute to the rail RCF damage, the sum over the number of vehicle wheels is performed, obtaining the total crack length for the right and left rail side (subscript *r/l*):

$$\sum_{j \in \text{right/left side}} C_{Lj}^{\;r}(s_r) = C_{Lr/l}^{\;r}(s_r) \tag{3-13}$$

This assumption implies that all the wheel-rail pairs contribute the same way to the crack growth on the rail.

Once the average crack length is calculated, the crack depth $C_{Dj}^{\;w}(s_w)$ and $C_{Dr/l}^{\;r}(s_r)$ can be evaluated through the following experimental relationship between the measured crack surface length C_L and the crack depth C_D:

$$C_L = f \cdot C_D \tag{3-14}$$

where the value of the scaling factor, experimentally evaluated during the tests, is approximately $f = 9$. Considering this experimental relationship, it is now possible to calculate the predicted crack depths (in mm) both for the wheel and for the rail:

$$C_{Dj}^{\;w}(s_w) = C_{Lj}^{\;w}(s_w) / f \qquad \text{3-15)}$$

$$C_{Dr/l}^{r}(s_r) = C_{Lr/l}^{r}(s_r) / f$$

The calculation of the crack depths in (3-15) is performed according to the simplified approach proposed in [14][15].

- *Scaling*

The same scaling procedure introduced in the wear model [1][2] is used to reduce the simulated track length and the consequent computational effort:

$$C_{Dj}^{w}(s_w)\frac{km_{step}}{l_{track}} = C_{Dj}^{wsc}(s_w)$$

$$C_{Dr/l}^{r}(s_r) * N_{step} = C_{Dr/l}^{rsc}(s_r) \qquad (3\text{-}16)$$

where km_{step} is the travelled distance inside each wheel discrete steps in which the total travelled mileage km_{tot} is subdivided and N_{step} is the number of vehicles moving in a rail discrete step (see Fig. 14). Both km_{step} and N_{step} are calculated in an adaptive way by imposing suitable threshold values $D^{w}{}_{step}$ and $D^{r}{}_{step}$ on the maximum thickness of material removed by wear on the wheel and on the rail at each discrete step. To this end, the following relationships have been used:

$$km_{step} = l_{track} * \frac{D^{w}{}_{step}}{\max(\Delta_j^{w}(s_w))}$$

$$N_{step} = \frac{D^{r}{}_{step}}{\max(\Delta_{l/r}^{r}(s_r))} \qquad (3\text{-}17)$$

where $\max(\Delta_j^{w}(s_w))$ and $\max(\Delta_{l/r}^{r}(s_r))$ are the maximum values of wear depth before the scaling operation.

- *Effect of wear on RCF*

Finally, after a smoothing process (the subscript sm indicates that the crack depth has been smoothed), the difference between crack and wear depths is calculated to consider the effect of wear. The cracks are considered worn off when this difference assumes negative values:

$$C_{D\,j}^{U\;w}(s_w) = \max(C_{D_{sm}\,j}^{wsc}(s_w) - \Delta_{sm}^{wsc}(s_w), 0)$$

(3-18)

$$C_{D\,r/l}^{U\;r}(s_r) = \max(C_{D_{sm}\,r/l}^{rsc}(s_\mathrm{r}) - \Delta_{sm}^{rsc}(s_r), 0)$$

The accumulated crack depth at the end of the whole iterative process is finally calculated by adding up the crack depths obtained for each discrete step of the procedure:

$$C_{TOT\;\mathrm{j}}^{\;w}(s_w) = \sum_{ns_w} C_{D\,j}^{U\;w}(s_w)$$

(3-19)

$$C_{TOT\;r/l}^{\;r}(s_r) = \sum_{ns_r} C_{D\,r/l}^{U\;r}(s_r)$$

where ns_w and ns_r are respectively the number of discrete wheel and rail steps of the procedure according to profile update strategy.

3.5. RCF law characterization

In order to characterize the RCF damage law of wheel and rail, specific fatigue tests has been carried out in the laboratory of the Tribology Research Institute of the Southwest Jiaotong University, using two scaled rolling-sliding test machines: the MMSA-2A test rig and the JD-1 test rig.

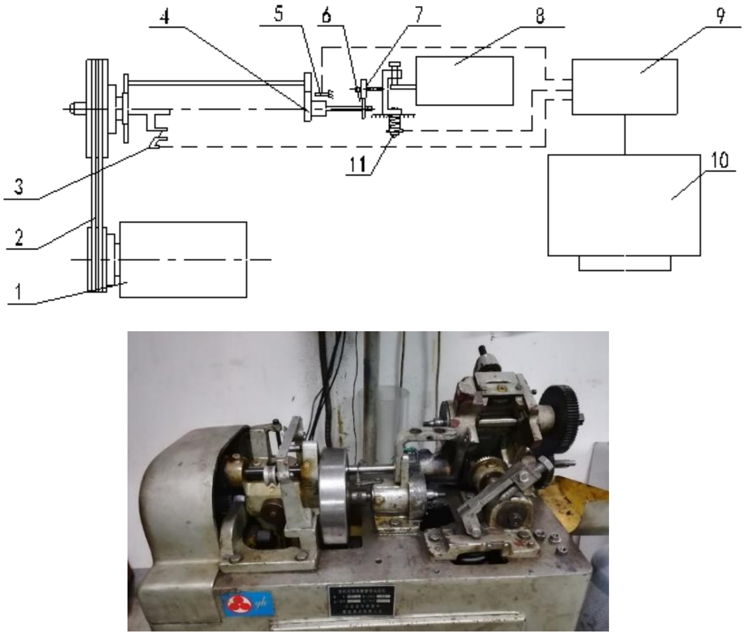

Fig. 32 MMSA-2A test apparatus: 1. DC motor; 2. Drive belt; 3. Torque sensor; 4. Drive shaft gears; 5. Photosensor; 6. Wheel roller; 7. Rail roller; 8. Driven shaft gears; 9. Controller; 10. Computer; 11. Load sensor

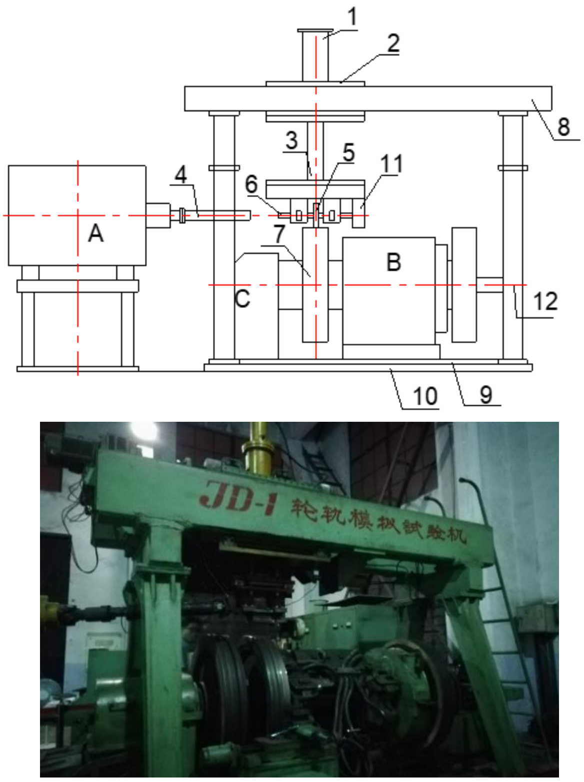

Fig. 33 JD-1 test apparatus: 1.Normal loading cylinder; 2.Loading carriage; 3.Spindle and yoke; 4.Univesal shaft; 5.Wheel roller; 6.Wheel shaft; 7.Rail roller; 8.Lateral loading cylinder; 9.Turning plate; 10.Base plate; 11.Magnetic powder brake; 12.Speed measuring motor; A,B.ZQDR-204 DC motor; C.Gear box

The MMSA-2A experimental apparatus (see Fig. 32) is a rolling-sliding wear testing machine composed of a wheel and a rail specimen of 40 mm in diameter, powered and controlled by a DC motor. The slippage (range 0% - 5%) between the wheel/rail rollers can be varied by changing the transmission gear pairs which transmit the power from the driving shaft to the driven shaft. The upper specimen is fixed in a swinging bracket where a normal force (from 0 to 2000 N) can be applied and adjusted by a compressed spring; the normal force is measured by a force sensor. A torque sensor (3) and a load sensor (11) measure the tangential and normal forces on the wheel/rail and the instant friction coefficient can be calculated exploiting the signals captured by these sensors. The JD-1 wheel/rail simulation facility (see Fig. 33) is made up of a small roller with a diameter of 68 mm as wheel roller (5) and a larger roller with a diameter of 1050 mm as rail roller (7). The two rollers, driven by independent electric motors, are hydraulically loaded in vertical direction. Thanks to a further hydraulic actuator is possible to apply a lateral force to reproduce the lateral force acting on the wheel and to simulate curve negotiation (range 0 – 2000 N). The tangential force between the rollers is obtained by the magnetic powder brake (11) installed on the wheel roller shaft (6). By changing the power of magnetic powder brake, it is possible to simulate different tangential forces. The forces on the wheel/rail interface (normal, tangential and lateral forces) are measured and recorded by means of three force sensors. The chemical compositions of rail and wheel rollers in weight percentage are shown in Table 1.

Two types of tests (see Table 2) were designed to determine the RCF law constants α and β necessary to describe the crack growth. In the first one, performed on the MMSA-2A test rig, the number of cycles ranged from 120 000 to 480 000 cycles while the normal load and contact stress were kept constant and equal to 1003 N and 850 MPa. The slippage at this stage of the research work is fixed and equal to 0.91% but, during the upcoming new test campaigns, it will be varied to consider its influence on crack initiation and propagation.

The second test was performed on the JD-1 apparatus (see Fig. 33) imposing a constant number of cycles (10^6 cycles) and varying the contact stress from 1000 MPa to 1600 MPa. All the experiments were carried out with dry surfaces and in ambient conditions. In both the tests the crack length L and depth h (according to Fig. 34) were measured by optical microscope (OM) and scanning electron microscope (SEM). In Fig. 35 a crack observed by OM on the wheel roller after 480 000 cycles is shown by way of example.

For each test an appropriate number of samples has been considered: the results have been processed following a statistical approach resulting in a normalized standard deviation of about 19%, acceptable for this kind of measurements. Even if normalized standard deviations of about 20% are not so low in absolute, they are quite satisfying for this kind of applications. In fact, due to the complexity of the phenomenon and of the measurement system, quite often normalized standard deviations of 30% - 50% may occur as well.

Table 1 Chemical compositions of the specimens

	C	Si	Mn	P	S
Wheel	0.56-0.6	≤0.40	≤0.80	≤0.020	≤0.015
Rail	0.65-0.75	0.10-0.50	0.80-1.30	≤0.025	≤0.025

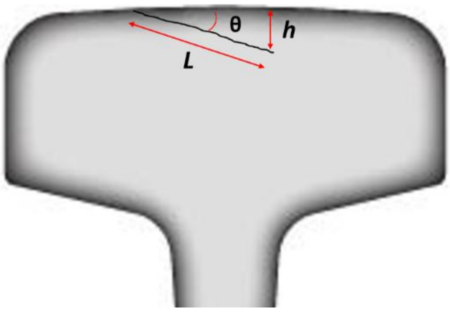

Fig. 34 Crack dimensions

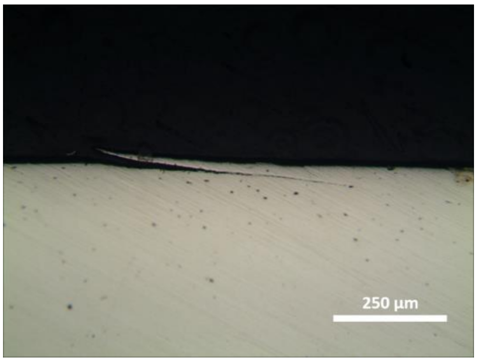

Fig. 35 Crack on wheel roller after 480 000 cycles

Table 2 Experimental tests performed

	Test 1	**Test 2**
Test apparatus	MMS-2A	JD-1
Contact stress	Constant (850 MPa)	Variable (1000 to 1600 MPa)
N° cycles	Variable (120 000 to 480 000)	Constant (10^6)
Contact conditions	dry	dry

Basing on the data coming from the experimental campaigns on test rigs described in this section and by using suitable least square based best fitting techniques [79], the following optimized values of the unknow parameters α and β have been obtained:

$$\alpha = 8.9\times10^5\ \text{mm}^{-1},\ \beta = -1.02$$

Since this kind of procedures is quite standard, it has not been described in detail here.

4. Corrugation: state of the art and current work

Rail corrugation has been a problem in the railway field for decades. In fact, trains passing on corrugated rails give rise to noise, ground-borne vibrations and more general dynamic loading, which increases damage of components of both vehicle and track.

In this paragraph, the corrugation phenomenon will be described together with the causes and characteristic of all type of corrugations observed to this day. Moreover, a description of the main commonly adopted treatments can be found. Then, an explanation of all the theoretical concepts behind the model developed during this Ph.D. work and the method adopted to implement them will been given.

4.1. Corrugation mechanisms and classification

During the years several studies and research have been carried out on this topic highlighting as corrugation arises from a variety of different causes and continue to be an important issue in railway field since no definitive solution has yet been found. From different research, it could be stated that corrugation usually appears on the low rail in narrow curves and partially in tangential tracks at traction or braking sites [51][57][74].This phenomenon is furthermore self-exciting: the dynamic behaviour of vehicles causes a change in the rail surface, which, in turn, excites the vehicle-track system in the same manner it has caused the irregularity, since vehicles speed is usually consistent on a certain section of the track. Both corrective and preventive maintenance of the vehicle track system is expensive, and vibrations bother passengers and people nearby the railway track.

The most important research about rail corrugation description is reported in the paper published in 1993 by S. L. Grassie and J. Kalousek [58] and its review of 2009 [59] where the Authors provided a classification of different rail corrugation.

The global mechanism which leads to corrugation growth is illustrated in Fig. 36. While the vehicle is running, vibrations from various sources as irregularities, friction or traction, may excite the system in a particular frequency range that may lead to a resonance of specific vibration modes of the system track-vehicle. In resonance condition, the contact parameters as normal and tangential forces fluctuate and acts as input to a so-called “damage mechanism” which results in a change in the initial longitudinal rail profile. The most common damage mechanism on almost all types of railways is wear. Other less common damage mechanisms are plastic bending of the rail, which occurs when the rail is bent beyond its yield point (rather like a wire coat hanger) and plastic flow. Since the dynamic forces are related to wear rate, the latter fluctuates in turn. These fluctuation of the instantaneous wear rate results in a different longitudinal wear status of the rail called corrugation. These initial excitations are the so-called "wavelength-fixing mechanism". This mechanism "fixes" not only the wavelength (their frequencies directly impact on the corrugation wavelength) but also the position of the eventual corrugation along the track. Many theories exist about the cause which brings to the excitation of wavelength-fixing mechanisms. The most studied is that of initial rail irregularities always present after the manufacturing process. The second one is related to wheelset-rail system instability caused by the behaviour of the contact interaction when the creep forces are near saturation as stick and slip. The latter is a continuous periodic passage of the contact condition from rolling to slipping. This behaviour leads the global creepage, as well as the creep forces, to oscillate at the same frequency, thus becoming a wavelength fixing mechanism.

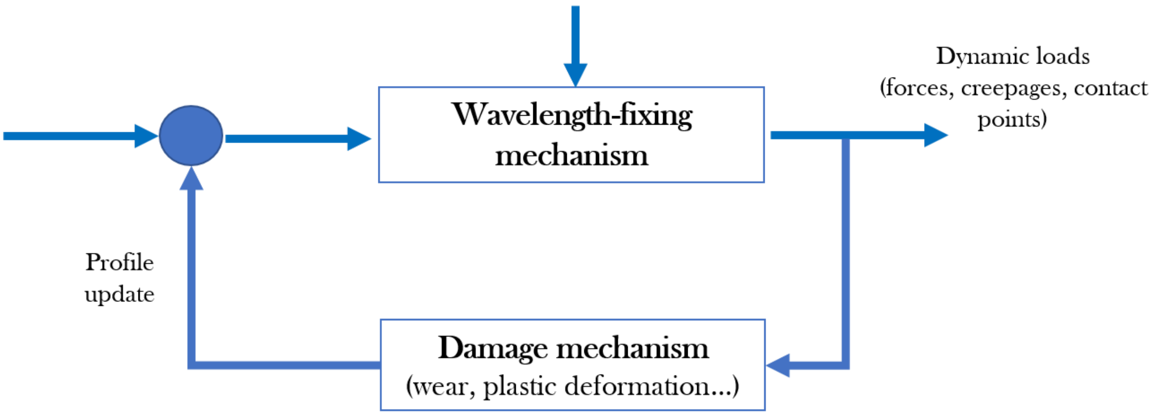

Fig. 36 Wavelength-fixing mechanism

In [58] Grassie classified the most common types of corrugation observed in function of their wavelength-fixing and damage mechanisms. Since all kinds of corrugation are basically constant-frequency phenomena, in Table 3 the approximate frequency range associated with the wavelength-fixing mechanism is also reported. Their wavelength can be calculated as:

$$\lambda = v / f \qquad (4\text{-}1)$$

where v is the speed of vehicles that cause the corrugation and f is the frequency of the related wavelength-fixing mechanism.

The identification of this frequency is a useful instrument to evaluate the type of corrugation observed on the track. Even a simple measurement with a ruler and knowing the line speed in the track section affected by this phenomenon could be a good starting point to identify the type of corrugation.

In the following a short description of the different types of corrugation observed to this day and their cause are described, according to [58].

Table 3 Types of corrugation, characteristics and treatments

Type	Wavelength-fixing mechanism	Where?	Typical frequency (Hz)	Damage mechanism	Treatments	
					Demonstrably successful	Should be successful
Pinned–pinned resonance (roaring rails)	Pinned–pinned resonance	Straight track, high rail of curves	400–1200	Wear	Hard rails, Control friction	Increase pinned–pinned frequency so that corrugation would be <20mm wavelength
Rutting	Second torsional resonance of driven axles	Low rail of curves	250-400	Wear	Friction modifier, hard rails, reduce cant excess, asymmetric profiling in curves	Reduce applied traction in curving, improve curving behaviour of vehicles, dynamic vibration absorber
Other P2 resonance	P2 resonance	Straight track or high rail in curves	50–100	Wear	Hard rails, highly resilient trackforms	Reduce unsprung mass
Heavy haul	P2 resonance	Straight track or curves	50–100	Plastic flow in troughs	Hard rails	Reduce cant excess when corrugation is on low rail
Light rail	P2 resonance	Straight track or curves	50–100	Plastic bending	Increase rail strength and *EI*	Reduce unsprung mass
Track-form specific	Trackform specific	Straight track or curves	-	Wear	Hard rails, friction control	Avoid “peaky” resonances, improve steering

1. "Roaring rails" or "pinned–pinned resonance" corrugation

Pinned–pinned resonance corrugation also named as "Roaring rails", occurs primarily in straight track and gentle curves, where minimal flange contact occurs. It is more frequent on the high rail and is commonly associated also with relatively light axle load traffic (i.e. <20 t). Example from the UK main-line railway are shown in Fig. 37. As can be observed from this figure, this type of corrugation appears as periodic bright running band (or bands) that lies along the rail surface A short wavelength corrugation of this amplitude would be enough for a loss of contact in the troughs so that a wheel would hammer along the track contacting only the corrugation peaks. The magnitude of impacts in such cases can be several times the static wheel load leading to a rapid deterioration of ballast, sleepers and fastening components.

Fig. 37 "Pinned–pinned resonance" corrugation with modulation over sleepers

The wavelength-fixing mechanism associated is represented by the pinned–pinned resonance of the rail, vibrating as if it were a beam that was almost pinned at the sleepers (or periodic rail fastenings). The frequency of this resonance is:

$$f = \frac{\pi}{2L^2}\sqrt{\frac{EI}{m}}\left(1-\frac{1}{2}\left(\frac{\pi r_g}{L}\right)\left(1+\frac{2(1+\upsilon)}{K}\right)\right) \qquad (4\text{-}2)$$

where m and EI are the rail mass per unit length and bending stiffness, respectively, L is the sleeper spacing, r_g is the radius of gyration and K is the shear constant of the cross section.

Corrugation is worse over sleepers because the support appears dynamically stiff and vertical dynamic loads are correspondingly greater. Since the dynamic loads at the frequencies of interest are high on corrugation peaks and low in the troughs, slip and wear of the troughs are encouraged. The pinned–pinned resonant frequency is higher respect to the frequency of other wavelength-fixing mechanisms and accordingly gives the shortest wavelength for a given train speed.

2. “Rutting” corrugation

This type of corrugation occurs primarily on the inside rail in curves, see Fig. 38, when the traction ratio (ratio between the tangential to normal force) on one wheel (usually the outer wheel of the leading wheelset) is close to the friction limit, so that it drives the opposite wheel in the wheelset in a roll-slip unstable oscillation. Although, it may also occur in straight track where traction or braking actions are particularly high. Applied traction increases the tangential force on the outer leading wheel and reduces it on the lower leading wheel, thereby increasing the difference in tangential force across the wheelset and exacerbating the stick–slip oscillation. Welds and joints and more in general all the discrete irregularities are common triggers for corrugation and often fix the position of corrugation along the rail. Rutting defect presents a uniform wavelength and can develop quickly to a depth of tenths of a millimetre.

Fig. 38 Rutting” on the inside (low) rail in a curve

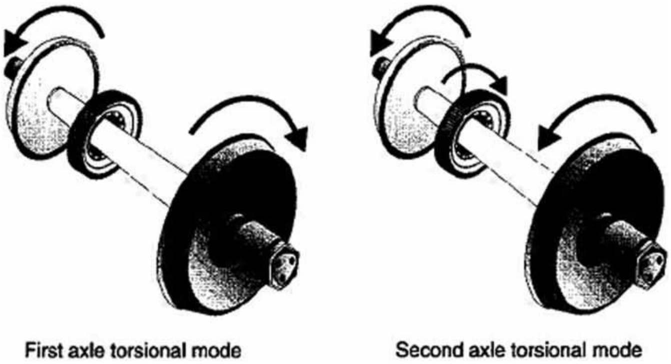

Fig. 39 Torsional resonances of wheelset [58]

The cause of rutting is the second torsional resonance of the wheelset as illustrated in Fig. 39. The frequency of the second torsional resonance is commonly about 250–400 Hz. The damage mechanism for rutting is quasi-periodic wear, with high peaks corresponding to the slip phase of a roll–slip oscillation.

3. Other P2 resonance corrugation

By its definition, the wavelength-fixing mechanism of this type of corrugation is the P2 resonance, which is the resonance of the unsprung mass on the track stiffness and also one of the most prominent and frequent cause of corrugation on a wide variety of railways. The damage mechanism is wear.

Fig. 40 "P2 resonance" corrugation on ballasted track, highlighted by grinding

In both ballasted and non-ballasted track, the P2 resonance can cause long wavelength corrugation that is clear when highlighted artificially by rail grinding (Fig. 40), but is otherwise difficult if not impossible to see with the naked eye. The difficulty of both seeing and measuring such long wavelength corrugation may well have led to its relative neglect. The frequency of both the P2 resonance and the first torsional resonance of wheelsets is commonly in the range 50-100 Hz, so it is unsurprising that severe corrugation can result where both resonances are excited. Corrugation that has arisen from a resonance in this frequency range is a particular problem on metros because the relatively low frequency "rumble" is transmitted well into buildings and occasional amplified by structural resonances that occur at similar frequencies.

4. Heavy haul corrugation

"Heavy haul" corrugation is a type of corrugation that exists on heavy haul railways. The wavelength-mechanism is the P2 resonance and the damage mechanism is gross plastic flow as result of excessive contact stresses, given by the superimposition of the dynamic loads and the high static loads. For this type of corrugation, irregularities such as welds and joints, are the common triggers which excite the P2 resonance. The treatment adopted is the use of hard rail to resist plastic flow combined with routine rail grinding to reduce irregularities that excite the P2 resonance. Heavy haul corrugation may occur both on the high and the low rail.

5. Light-rail corrugation

"Light-rail" corrugation has many aspects in common with heavy haul corrugation. As heavy haul corrugation, the treatments proposed in Table 3 are satisfactory, thus, it is briefly described here. Like heavy haul corrugation the wavelength fixing mechanism is the P2 resonance, but the principal difference is that the damage mechanism is plastic bending on the rail, so the corrugation can be measured both on the rail head and the rail foot. This phenomenon is particularly associated with light railway lines, where the load required to cause plastic bending of the rail is lower than that required to cause plastic deformation of the of the work-hardened surface layer of the rails. Modern rail steels and more robust rail sections have a sufficiently high bending strength to resist damage by this mechanism.

6. Trackform specific corrugation

Some trackforms are associated with rapid corrugation formation, while corrugation on others occurs less quickly. A common characteristic of trackforms on which corrugation occurs preferentially is a pronounced resonance. For example, some non-ballasted trackform has given rise to corrugation. The wavelength-fixing mechanism in this case is the lightly damped resonance of a large, resiliently supported baseplate on the resilience of the railpad, at a frequency of about 400 Hz. For this generic type of corrugation, the damage mechanism is wear.

4.2. Corrugation treatment

In Table 3 the treatments used today to mitigate the different types of corrugation are listed. If a treatment is a preventative measure, a cure of an existing problem, or simply reduce the severity of corrugation depends on several factors. The classical and most common treatment for corrugation defects is rail grinding, which is mainly considered as a palliative since it has no potential of preventing its reappearance. In fact, if corrugation is caused by railhead irregularities, the removal of them often delay the occurrence of corrugation sufficiently to be considered the grinding an extremely satisfactory treatment even if it does not eliminate the mechanism that causes the corrugation. Other treatments include rail head hardening which increases the yield strength of the rail material. Another typical solution is the use of friction modifiers (FM) which avoid a negative slope in the contact force-creepage curve. In the following a short description of the main solutions used to mitigate the corrugation will be given.

1. Reprofiling and removal of corrugation

Considering the underlying mechanism of the defect (Fig. 36), the reduction of railhead irregularities is a basic treatment of all types of corrugation. Where the damage mechanism is wear, reprofiling is more of a treatment than a cure, although an extremely successful one if it is administered satisfactorily. Corrugation would recur relatively slowly on the rail with minimal roughness and periodicity but can grow particularly quickly if the grinding signature excites a possible wavelength-fixing mechanism. European standard now exists that states objective limits on the longitudinal irregularities that should remain on a rail after reprofiling [60].

2. Hard rails

Hard rails are a treatment of all types of corrugation. A sufficient yield strength of rails can preserve to plastic flow and be therefore a treatment of heavy haul corrugation, while a high bending strength avoids light rail corrugation. Then, corrugation by these mechanisms may be totally eliminated simply by satisfactory rail selection.

3. Control of friction

Friction influence significantly all types of corrugation in which wear is the damage mechanism, since higher the coefficient of friction is greater the wear rate will be. Especially, in a dry environment, as in tunnels in subway applications, the friction coefficient can reach also values of 0.6, with severe consequences for wear. Many “friction modifiers” are commercially available to control the coefficient of friction to levels of about 0.35 offering a successful method of controlling all types of corrugation for which wear is the damage mechanism. The treatment is particularly effective for “rutting”, which results from a roll–slip oscillation of the wheel on the rail since these substances limit the reduction of friction with sliding speed, thus eliminating the potential instability associated with a falling friction characteristic.

4. “Improved steering” and reduction of tangential loads

Curves are particularly susceptible to corrugation consequently of the high tangential forces that arise from steering, particularly in combination with applied traction. Accurate track design, vehicle or wheel and rail profiles can be some solutions to reduce these forces. Since contact forces are particularly damaging in presence of excessive cant, a smaller cant not only results in more similar tangential forces on opposite wheels in a wheelset but also reduces the tangential force on the low rail reducing stick–slip oscillation. A larger rolling radius difference are an effective method of reducing curving forces and corrugation in curves. However, wheel and rail profiles that increase rolling radius difference encourage contact along the gauge shoulder and gauge corner of the rail, thereby increasing contact stresses. Consequently, such profiles need to be designed carefully taken into account vehicle dynamic behaviour as well as wheel and rail damage.

5. Trackform

A trackform should have a low P2 resonance and high damping of any resonant behaviour that cannot be avoided to reduce the possible corrugation growth. “Roaring rail” corrugation appears to be an unavoidable consequence of track that is supported periodically: theoretically a continuous support should reduce the severity of roaring rail corrugation but the track tends to be relatively stiff, thereby increasing the likelihood of P2-resonance corrugation. It is also more difficult to control track geometry during construction.

6. Wheelsets

There is some evidence that rutting is greatly reduced when the wheelset is torsionally resilient, as occurs with some types of resilient coupling of driven axles. The opportunity still exists to develop a torsional dynamic vibration absorber for an operating vehicle to attenuate rutting corrugation, as proposed in reference [54].

7. Traffic

All types of corrugation observed are substantially constant-frequency phenomena. Consequently, a constant speed of trains and a not varied traffic encourage the growth of consistent wavelength of any corrugation that results from excitation of a particular wavelength-fixing mechanism. A true mixed traffic on the line, with a mix of both vehicle type and train speed, is an ideal antidote to corrugation formation.

4.3. Corrugation modelling approaches

Rail corrugation has been observed and described for years but studies that consider the numerical prediction of long-term growth of rutting corrugation are not so frequent [57][58][59]. A complete summary on rail corrugation studies over the years can be found in

[61] where an exhaustive review on studies in the 1970s, classification of rail corrugation, short-pitch corrugation and studies in Japan in recent years is given.

In the work of Tassilly and Vincent [62][63] a rutting corrugation with wavelength 3 - 60 cm was detected on the low rail of small radius curves on a RATP track. Through a linear frequency-domain model, it has been noticed the influence of the first symmetric and first antisymmetric bending eigenmodes on the wear rate of the leading wheelset and for the trailing wheelset the first antisymmetric torsional eigenmode dominated the response. More recently, Saulot et al. [64] investigated rutting corrugation at RATP focusing on the tribology of the contact which triggers the corrugation. Experimental tests were conducted on the full-scale test rig of Lucchini Sidermeccanica and Politecnico di Milano [65] reproducing the corrugation growth and identifying the cause of the corrugation at RATP with the high lateral creepage and creep force developed at the leading wheelset.

Many studies can be found on corrugation in North American metro systems: Kalousek and Johnson investigated the damage on Vancouver mass transit system [66] and rutting corrugation on five different metro systems in the USA have been analysed by Grassie and Elkins [51]. Suda and Matsumoto have been carried out several experiments and developed numerical models during the years. Rutting corrugation on the Yamanote metro line in Tokyo has been investigated in [69][70] and on a 160 m radius curve in [71] using a simple six dof (degrees of freedom) mathematical model, considering the wheelset torsional flexibility with a rotational spring. The stick-slip oscillation caused by a coupling of the torsional eigenmode of the wheel axle and the vertical vibration of the wheelset on the stiffness of the Hertzian contact spring was discovered to be the wavelength-fixing mechanism. The general trend in the last ten years, was the use of time-domain approaches to consider the high non linearity of the dynamic vehicle-track system. The study of Kurzeck and Hecht, presented in [72][73], investigated vibrations with a frequency of 80 Hz occurring at a light rail vehicle in Stuttgart in curves with radii between 50 and 200 m. The aim of this investigation was to identify the oscillation and transmission mechanism, and the dominant parameters within this. As the cause could not be clearly identified from the measurements, a multi-body simulation in the time domain was used. The model consists of both vehicle and track and it considered the structural dynamics of the wheelset and bogie frame up to 200 Hz. The system was modelled using the commercial multibody software Simpack. A friction induced vibration, involving the first bending mode of the leading wheelset and the P2 resonance, was discovered to be the cause of corrugation.

Frequently, simplified contact models are employed in simulation of long-term corrugation growth, both for the computational load needed for the dynamic vehicle-track interaction solution and for the calculation of wear. Recently, some researchers start to use non-Hertzian and non-steady contact models for the wear calculation [74][75][76][77].

Firstly in Torstensson's work and then in Carlberger's studies [76][77], corrugation on small radius curves was examined developing a time-domain model for the prediction of long-term growth of rail roughness. Dynamic vehicle-track interaction in a broad frequency range (at least up to 300 Hz) was simulated using the commercial software Simpack. Wheelset structural flexibility has been accounted for by using modal parameters calculated with a finite element model while the flexibility of the track is accounted by means a simple beam model. A non-Hertzian and non-steady wheel-rail contact, and the associated generation of wear was calculated in a post-processing step in the software Matlab: Archard's law was applied to model the sliding wear. The numerical results were compared with measurements from a curve of Stockholm metro network. The predictions showed corrugation growth to be generated by the leading wheelset of passing bogies at wavelengths approximately corresponding to those observed on the reference curve of the Stockholm metro. The corrugation wavelengths were related to coupled vibrations of the vehicle–track system involving wheelset bending eigenmodes. In the Torstensson's research rutting corrugation on small radius curves (the same reference curve as Carlberger) was studied [74][77]. The specific type of corrugation called rutting on the low rail was both analysed through field measurements and modelled using a numerical time-domain vehicle-track model. On the reference curve, rutting corrugation with wavelengths 5 cm and 8 cm was linked to vibrations of the leading wheelsets of passing bogies in their first and second bending eigenmodes. The developed time-domain model used a non-Hertzian and non-steady wheel-rail contact model. The model has been validated in the frequency range below approximately 250 Hz. Predictions showed a large dependence of the friction on the development of corrugation. For friction below 0.3 almost no corrugation growth was predicted. This is in agreement with results from field tests where a friction modifier was applied on the reference curve. Furthermore, it was predicted and confirmed by observation that the corrugation develops towards a constant amplitude. This phenomenon was attributed to a decreasing phase difference between the calculated wear and the accumulated rail irregularity. Also in this work, the flexibility of the track is accounted by means simple beam models.

4.4. The current work: corrugation prediction model

Simulating the evolution of corrugation on rails requires, basically, a dynamic analysis of the vehicle running along the track and a long-term damage model (see Fig. 2). In a dynamic simulation, the multibody model and the contact model work together: the first one evaluates the kinematic variables and the contact model evaluates the forces acting on wheel and rail. Knowing the dynamic behaviour of the vehicle, particularly the forces acting on the rail, is essential for the calculation of the amount of removed material from the rail surface and then for the evaluation of corrugation defect. In fact, once the dynamic analysis is carried out, the global contact variables are passed to the damage block which evaluates, in a post-calculating step, the worn rail surface to pass back to the multibody model, because of wear due to vehicle passages, in an appropriate coordinate system. All phases of the damage block (local contact model, wear model and profiles update) are implemented in Matlab environment. During service, vehicle wheels change their profile, because of wear leading to a change in the contact conditions. Unlike the other modelling approach described in 4.3, in the present model this effect is considered and thus the variability of wheel profiles in the simulation of corrugation growth has been included. In this way the dynamic vehicle-track interaction is influenced by the real change in rail and wheels surface during the cyclic process. Moreover, measured wheel profiles are included in the simulation procedure which follows a discrete process allowing to reduce the number of simulation steps and thus computational times. The time scale characteristic of the rail corrugation evolution, is much greater than wheel wear evolution, causing the same probability that each discrete rail surfaces comes in contact with each possible wheel profile. For this reason, for each rail surface, the whole wheel wear evolution (from the original one to the final worn profile) is simulated. Wheel profiles are loaded in Simpack similarly to ones which describe the rail surfaces: each wheel profile is described with two vectors representing the z-coordinate as a function of the lateral y-coordinate.

The adopted simulation strategy, similar to that described in 2.3.3 is clarified in Fig. 41: starting from a new rail surface, for each wheel measurement set $\mathrm{w_i}$ $(i = 1, \dots n)$, a simulation is carried out, referred as "wheel step". In the rail step, in which the rail surface is considered constant, the scaling procedure described in the previous section is used for every single wheel step; the number of trains is calculated as well. The output of each i wheel step is a corrugated rail surface, referred as $\mathrm{r}_i^{(0)}$, where the apex indicates the rail surface used in the dynamic simulations (0 represents the initial rail surface). After calculating every single rail surface in the first rail step, these ones are arithmetically averaged to obtain the first corrugated rail surface, indicated as r_1: this surface is passed back to the dynamic model, so it can be used in the second rail step. Thereafter, the model again carries out simulations for each of the i wheel step (with the same measurement sets) keeping the rail surface constant. After the output profiles $\mathrm{r}_1^{(1)}, \mathrm{r}_2^{(1)}, \ldots \mathrm{r}_n^{(1)}$ are evaluated, the r_2 rail surface is obtained. A series of rail step is then carried out to obtain the corrugated surfaces $\mathrm{r}_3, \mathrm{r}_4, \ldots \mathrm{r}_m$. The averaged train passages are accumulated, rail step after rail step: when the accumulated number of trains is more than the required one, the simulation procedure is stopped, and the final corrugated surface is obtained.

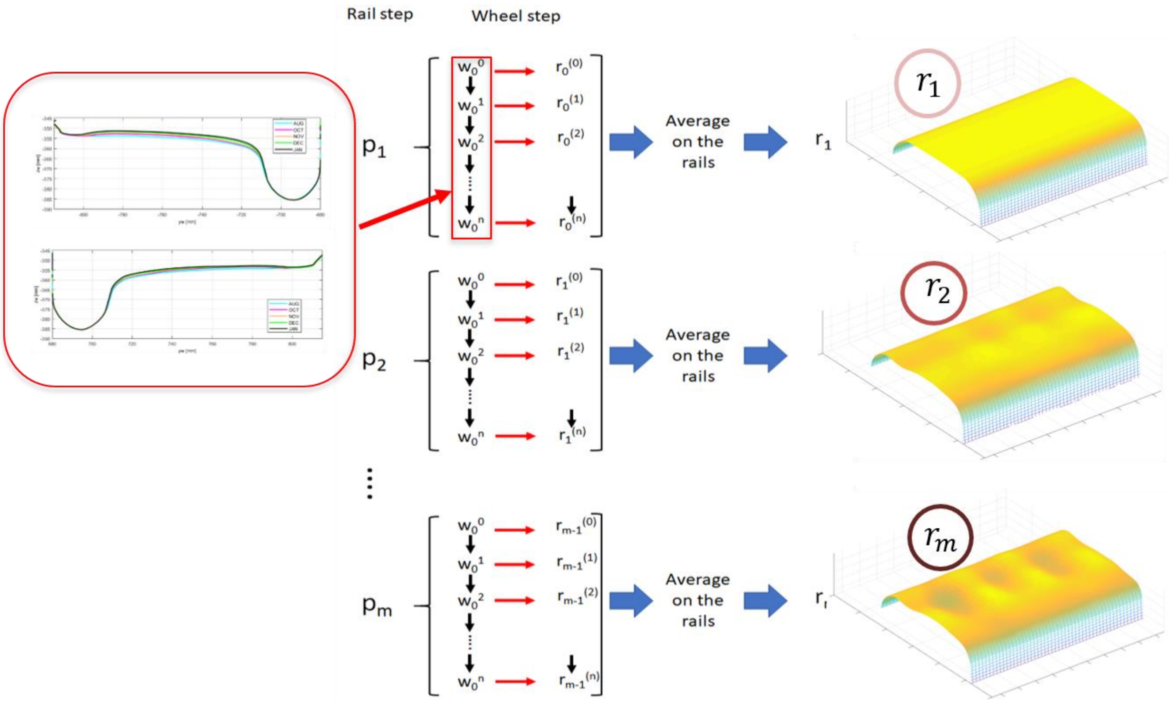

Fig. 41 Simulation strategy

4.4.1. The contact model

The commercial multibody software Simpack used to model the vehicle and the track, includes a wheel/rail contact module which allows the resolution of wheel-rail contact. To achieve a faster and a computationally efficient solution (but obviously more approximate), has been used the contact tool implemented within the multibody software.

Usually a contact model is made up of three main steps: the contact point search, the normal and tangential problem resolution. For the evaluation of the contact quantities in these three phases, is essential knowing the kinematic variables of the bodies in contact. In fact, the multibody model and the contact model work in a loop: once the contact variables are evaluated, the multibody model calculates the kinematic variables to be given to the following time step. In Simpack Rail, there are already available several contact models already implemented, based on the well-known theories of contact mechanics, which work on-line during the dynamic simulations. In the contact points search, the number and the exact position of the contact points are evaluated: these ones represent the points where normal and tangential forces are applied. For the contact points detection, the "equivalent elastic method" is chosen in Simpack [78]. In this method, the number of contact points and their location are determined from the intersection of the three-dimensional contact surfaces of wheel and rail accounting for the wheelset yaw angle. The algorithm determines where the rail profile and the wheel profile interpenetrate geometrically: these are considered as the actual contact patches, because, the fact that the contact area is smaller than the interpenetration surface area is deliberately ignored. To reduce the calculation effort, the actual contact patch shape is converted into an equivalent ellipse whose width and length are set equal to the maximum width and length of the interpenetration area. An equivalent penetration is determined as the penetration of a circle segment that has the same width and cross-section area as the actual interpenetration. Instead, the equivalent penetration is artificially increased by a constant factor, to make it consistent with the interpenetration patch area. Using the equivalent semi-axes and new penetration, the contact forces can be easily determined by means of the Hertzian formulas [31] and using FASTSIM algorithm [30][31] for normal and tangential directions respectively. The forces are applied at the so-called contact reference point, which is located at the area centre of gravity of the actual interpenetration cross-section area. Using Hertz's theory, the contact model evaluates the global normal force and the normal pressure distribution inside the patch can be easily evaluated. Once global creepages are known, FASTSIM algorithm evaluates tangential pressure distribution and local creepages: knowing the tangential pressure distribution, the global tangential force acting in the contact point, can be evaluated.

4.4.2. Track model

The input track model represents the benchmark curved segment, which has shown a severe corrugation growth on the low rail. The reference system defined in the multibody software for the description of rail surfaces is shown in Fig. 42. The reference system is placed with the y axis representing the top the rail of the ideal track (with any kind of irregularity), with the origin placed in the centreline. The x-coordinate points towards the running direction and is tangent to the centreline, the z-axis points downwards. In Simpack, the profiles are described as vectors with the vertical z-coordinate as a function of lateral y-coordinate. To describe the rail surfaces, a series of different rail profiles function of the curvilinear s_{lon} coordinate are implemented to model the track (see Fig. 43).

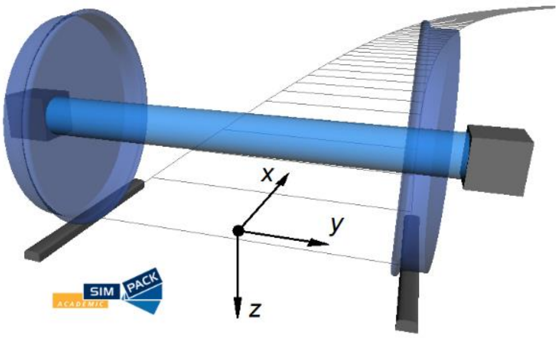

Fig. 42 Track reference system

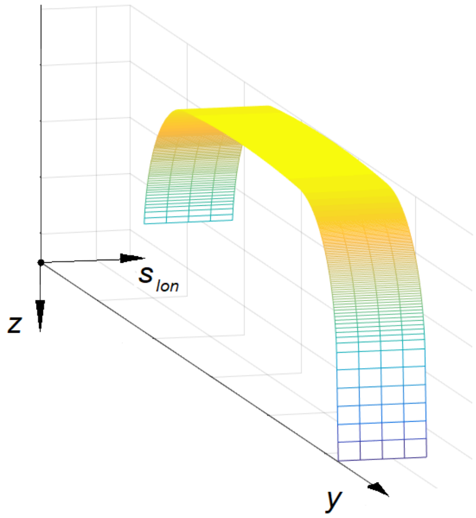

Fig. 43 Rail surface description

Since corrugation starts to growth because of initial irregularities present on the rail surface if the track model had a constant rail profile along the longitudinal direction, rail corrugation couldn't be pointed out in the simulation results. For this reason, it is needed to add an initial rail irregularity to the track model, which represents the rail roughness measured after a grinding process. Moreover, since wear is evaluated in the circular section of the track, where a steady-state running behaviour is reached, it is reasonable to consider only a small section of the curve for the evaluation of the removed material. In fact, considering a longer section of the track, results would be similar, since the vehicle behaviour is consistent along this portion of the curve. In Fig. 44 lateral forces (along the y-coordinate) acting on wheels of the leading wheelset (first in the running direction), in the case where no initial irregularity is added are shown. The section where wear is evaluated is pointed out in the graph: where it starts, steady-state-curving behaviour is fully reached, namely at 220 m.

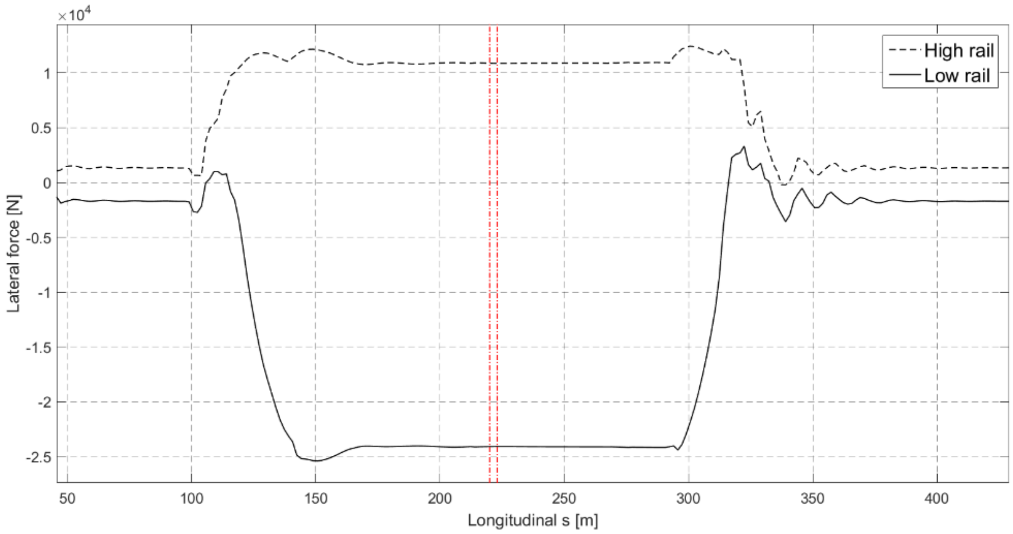

Fig. 44 Lateral forces acting on the first leading wheelset wheels, expressed in the track coordinate system

In this portion of track the initial rail irregularity is added by translating the rail profile along the z-coordinate, according to measured initial irregularity. A small step size compliant with the wavelength of the defect has been used to update the rail profile inside the section of the curve where the development of corrugation has been investigated. Outside this section, the rail profile is described by using a new rail profile.

4.4.3. Damage model

The part named "corrugation model" in Fig. 2, consists of the local contact model, the wear evaluation and the profile update as in the part of the tool for wear and RCF estimation. Since only global variables can be exported from Simpack to the damage block, the local contact model must re-evaluate normal pressure distribution, tangential pressure distribution and local creepages, using Hertz's local theory and FASTSIM algorithm. Then, the distribution of removed material (hypothesizing the contact in dry conditions) is calculated on the rails surface using the experimental law described in 2.3.2. Finally, rail profiles are updated: the new profiles are the outputs of one discrete step of the whole model loop and must be passed back to the dynamic model in order to continue the corrugation growth cycle described in Fig. 2 and to simulate the vehicle dynamics with the new updated profiles of rail and wheel.

4.4.3.1. The local contact model

As previously mentioned, in Simpack, each of the rail profiles which describes the rail surface along the longitudinal s_{lon}, is represented as a series of points $z_i = f(y_i)$, with $i = 1,2,\dots,n$. The y_i points are equally spaced on the y axis. For wear calculation, it is better to express these points in a parametric form, changing the coordinate system (of every single rail profile):

$$\begin{cases} y_i = f(s_i) \\ z_i = f(s_i) \end{cases} \tag{4-3}$$

Using this form, with the same number of points (evenly spaced), it is possible to guarantee a constant resolution along the curve describing the rail profile, as shown in Fig. 45. The number of points was reduced in order to well clarify this concept. In the simulations, the distance between two points s_i and s_{i+1} is chosen 0.1 mm. This new curvilinear coordinate will be referred as lateral *s*-coordinate s_{lat}. This is particularly useful, since wear must be removed along the normal direction to the rail surface. Then, the algorithm starts evaluating contact pressures for the contact point $P_{ri}^{j}(t)$ with $j = 1,2 \dots n_w$, $i = 1,2 \dots n_p$ (n_w is the total number of wheel-rail pairs and n_p is the maximum number of contact points per wheelset). A generic node of the contact patch is referred as (x, y).

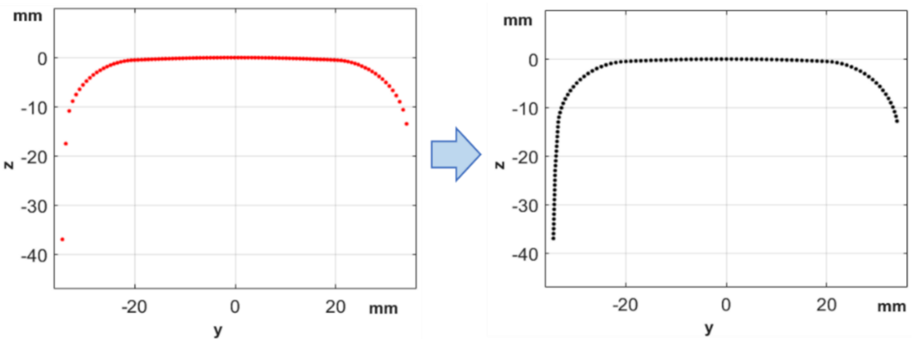

Fig. 45 Discretization od rail profile along curvilinear lateral abscissa

4.4.3.2. The wear evaluation

Basically, the estimation of removed material is the same described in 2.3.2. Knowing the tangential pressure distribution inside the contact patch, it is possible to calculate the amount of material to be removed from the rail $\delta_{P^j_{ri(t)}}(x,y)$, using the law described in in 2.3.2. This quantity, given for unit of travelled distance, in the generic node of the contact patch $P^j_{ri}(t)$ is expressed as (mm^3/(m mm^2) = mm/m). Particular attention must be brought to the time discretization: in fact, each quantity exported from Simpack is expressed as a discrete function of time t_k, with $k = 1,2 \ldots t_{tot}$. The amount of removed material at time instant t_k (in mm), is the product of $\delta_{P^j_{ri(t)}}(x,y)$ and the distance travelled by the contact point $P^j_{ri}(t)$ in the time interval $\Delta t_k = t_{k+1} - t_k$:

$$\delta_{P^j_{ri}(t_k)}(x,y) = \delta_{P^j_{ri}(t_k)}(x,y) \cdot \Delta S_k = \delta_{P^j_{ri}(t_k)}(x,y) \cdot V_{lon} \Delta t_k \qquad (4\text{-}4)$$

If the time interval is too large, the amount of wear $\delta_{P^j_{ri(t)}}(x,y)$ would produce a hole in the rail surface in $P^j_{ri}(t)$ with no physical meaning. For this reason, the time interval Δt has been chosen so that ΔS is of the same order of magnitude of the distance between two adjacent node of the contact patch along the running direction. Once the quantity of removed material is known inside the contact patch, it is stored on a grid representing every point of the discretized rail surface, as shown in Fig. 46. One element of the grid represents a certain position on the rail surface of generic coordinates (s_{lat}, s_{lat}) lateral and longitudinal respectively. Two grids, one for each rail, are chosen to represent the accumulated wear: difference in length between high and low rail is neglected, thus, the longitudinal *s*-coordinate represents the length from where the considered track begins as well as the distance from the origin of each rail. These grids will be referred as “main grids” in the following.

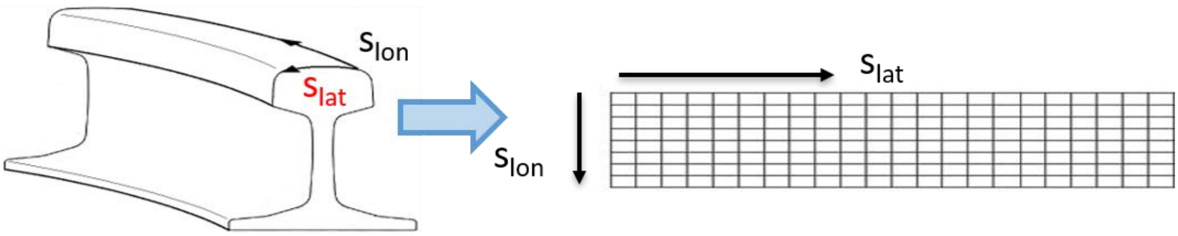

Fig. 46 Rail “main grid”

The discretization of this grid is the same to that used for the rail surface description, thus each element on the grid has the same position of a point used to describe the rail surface, therefore, once the total amount of wear to be removed from the rail surface is known, each point of the rail surface can be translate along its normal direction, without further interpolations.

Since the contact patch is considered planar and knowing $P_{ri}^{j}(t)$, the amount of wear in each node of the contact patch can be easily expressed in the new curvilinear coordinate system (s_{lat}, s_{lat}):

$$\delta_{P_{ri(t)}^{j}}(s_{lat}, s_{lon})$$

However, nodes in the contact patch are not distributed on a grid, as shown in Fig. 47. Therefore, an interpolation on the main grid is required. Since interpolating the patch wear on the main grid for each of the n_w wheelset, for each n_p contact point and for each t_{tot} time instants is time consuming, to reduce the computational load, an interpolation is firstly carried out on a smaller grid.

This "small" grid is discretized equally to the main one: the position represented by each of its element is the same to that represented by the corresponding ones, on the main grid. The small grid is like a "cutting" of the main one, wide enough to enclose the contact patch. During this interpolation, the volume of the removed material is preserved, as shown in Fig. 48: the points represent the wear in the nodes of the contact patch, while the coloured part represents wear stored in the small grid.

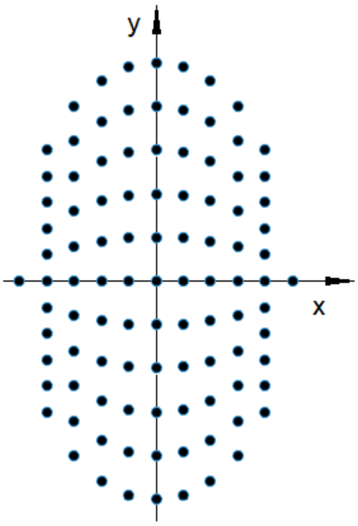

Fig. 47 Distribution of nodes inside the contact patch

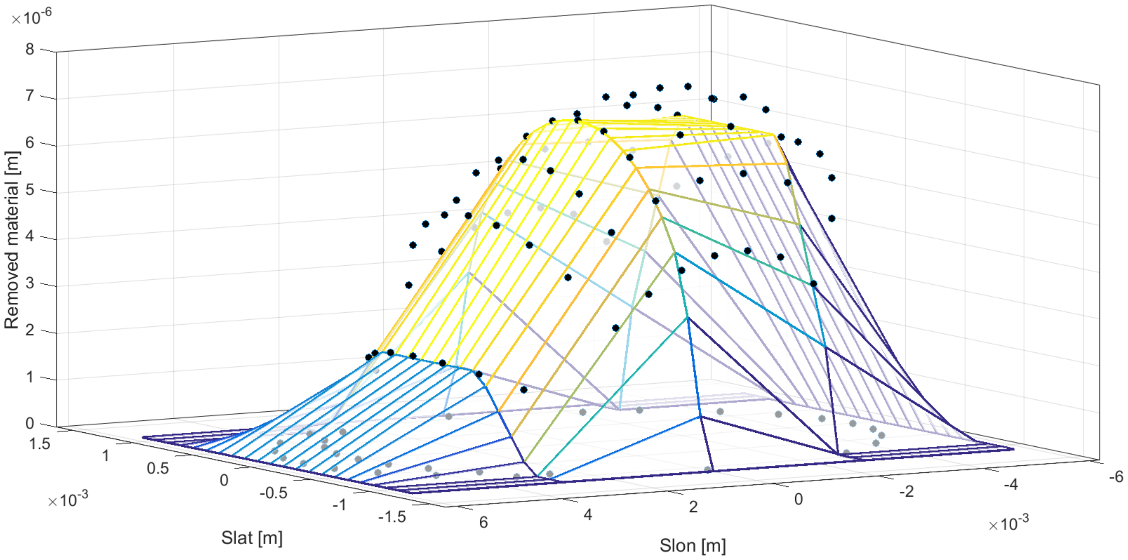

Fig. 48 Interpolation on the "small grid"

The interpolated quantity will be referred as:

$$\Delta_{P_{ri(t)}^{j}}(s_{lat}, s_{lon})$$

The wear on the small grid is easily added to the main one, since it does not require any further interpolation:

$$\sum_{k}^{t_{tot}}\sum_{j}^{n_w}\sum_{i}^{n_p}\Delta_{P_{ri(t)}^{j}}(s_{lat}, s_{lon}) = \overline{\Delta}(s_{lat}, s_{lon}) \tag{4-5}$$

This represents the wear due to one vehicle passage.

Because of numerical noise, a smoothing of the accumulated wear is necessary: rough surfaces in fact, once updated, would cause problems in the evaluation of the contact forces, inside the contact model. The smoothing procedure must obviously conserve the volume of removed material.

$$\Im\left(\overline{\Delta}_r(s_{lat}, s_{lon})\right) = \Delta_{sm}(s_{lat}, s_{lon}) \tag{4-6}$$

4.4.3.3. Profile update

The amount of wear stored in the main grids represents only the damage due to one vehicle passage. Although the benchmark curve has shown severe effects of rail corrugation due to wear, however, it takes thousands of train passages to switch from a post-grinding condition to a condition in which maintenance is necessary, according to the specification requirements. Thus, it is clearly impossible to simulate every single train passage: the same scaling procedure described in 2.3.3 has been adopted excluding the longitudinal integration.

5. Test case: tramway application

The proposed damage tool has been initially tested considering a tramway application. In the following paragraphs a detailed description of simulated scenario illustrating the track layout, the vehicle main characteristics and its mission profile, essential inputs for the damage tool, will be given. In this test case, the aim was to evaluate the wear evolution and RCF crack growth assessment to compare the obtained results against experimental data. Concerning the RCF, since the law coefficients have been validated against specific experimental laboratory tests performed under strictly controlled conditions, the model trustworthiness is assured. Considering wear, since the wear model is based on an experimental relationship found in the literature, a validation against wheel measurements acquired on field has been carried out to assess the model reliability. The control parameters capable of estimate the wear evolution on the wheel and rail will be defined, and the experimental data and their processing will be introduced. Then, the wear assessment of the most critical curve in the line will be investigated using measured data obtained from an innovative measuring procedure which use a 3D optical scanner. Finally, a sensitivity analysis was carried out to evaluate the response of the model to some of the solutions adopted to mitigate the problem of wear and RCF.

5.1. Simulated Scenario

The entire Tram Line 1 of the city of Florence that connects the railway station Santa Maria Novella to the suburban area of Florence is the reference track (see Fig. 49). With an approximate length of 7.4 km and 14 intermediate stops, it is equipped with the standard track gauge (1435 mm) and a 60R2 rail profile (see Fig. 50). It is characterized by very narrow curves (also less than 50 m radius) that deeply affects the wheel and rail life. The whole network has been reconstructed and modelled in Simpack environment starting from the track data provided by the partners.

The chosen benchmark vehicle is a tramway vehicle (see Fig. 51) designed by Hitachi Rail, which operates on the previous described line. It is an independent wheels and articulated tram, built on Sirio platform and it is equipped with 3 bogies (two motor and the central one trailer) and five coaches (two motor with cabin, one trailer and two hanging). The general layout of the Sirio vehicle and the nomenclature used are shown in Fig. 51 and Fig. 52. The main vehicle dimensions are summarized in Table 4.

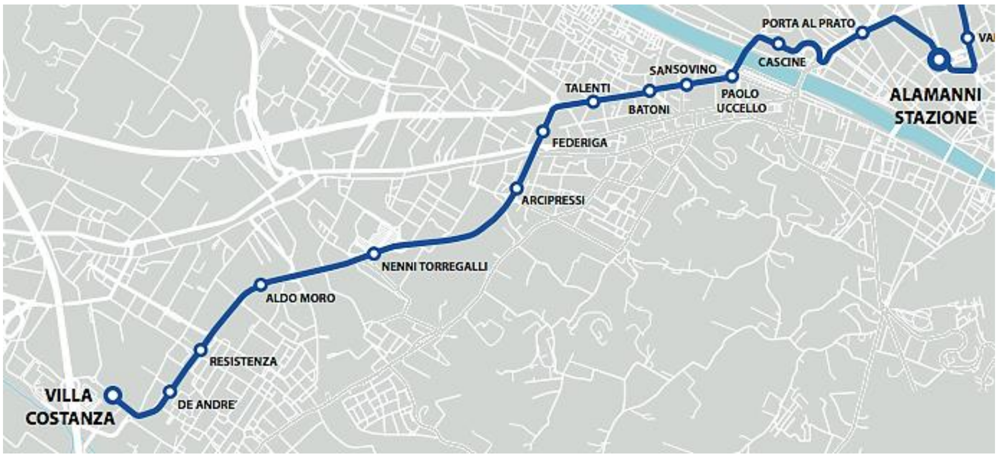

Fig. 49 Tramway Line 1

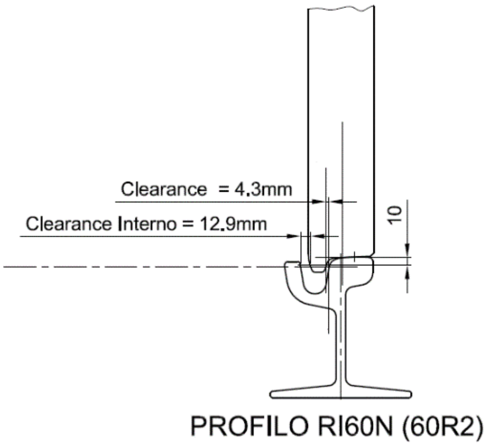

Fig. 50 Wheel-rail coupling

Fig. 51 Tram Sirio vehicle

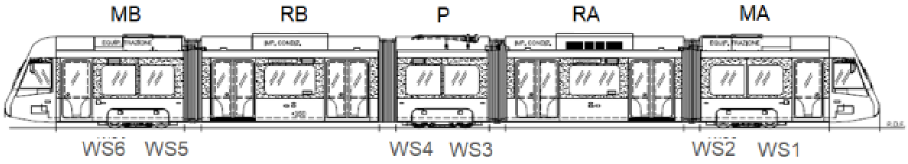

Fig. 52 Vehicle nomenclature

To allow the continuous 100% low floor, the bogies are designed with all the equipment (traction motor and the friction brake units) located on the sides. The two traction motors (one for each bogie axle) distribute the motor torque between the two wheels of the same axle through a differential device that allows different rotation speeds of the independent wheels when the vehicle is running a curve. When, instead, the vehicle runs on straight sections, the two wheels are stiffly re-connected by means of a clutch locking device. The mechanical connection between the two wheels of the same pseudo-axle is guaranteed by means of a shaft under the floor. The wheelbase is 1700 mm and the bogies are equipped with elastic 660 mm diameter tired wheels.

Table 4 Main vehicle and line characteristics

Vehicle overall length	32 030 mm
Width	2 400 mm
Height	3 414 mm
Floor height from t.o.r.	350 mm
Wheel arrangement	Bo-2-Bo
Bogie wheelbase	1 700 mm
Wheel diameter	660 mm
Track gauge	1 435 mm
Wheel profile	UNI 3332
Rail profile	60R2

Concerning the suspension system, a two-stage architecture was adopted: the primary suspension is fitted with rubber elements and the secondary one consists of a double coaxial helical spring.

The multibody model is built in Simpack Rail environment and consists of (see Fig. 53 and Fig. 54):

- five coaches;
- three bogies: the central bogie is trailer while the other ones are motorized;
- six drop axles for low floor;
- four motors: one for each side of motorized bogie;
- twelve gearboxes: four for each bogie;
- twelve brake disks: one for each wheel.

The rigid bodies are connected by means of appropriate elastic and damping elements; particularly, the vehicle is equipped with two suspension stages. The primary suspensions are two appropriate spring-damper elements and connect the drop axle to the bogie frame, while the secondary suspensions connect the bogies to the coaches and comprise the following elements:

- four coaxial helical springs;
- four non-linear dampers (lateral, vertical dampers);
- two non-linear lateral bumpstops;
- four non-linear vertical bumpstops.

Both the stages of suspensions are modelled by means of three-dimensional viscoelastic force elements taking into account all the mechanical non linearities of the system (bumpstop clearance, dampers. etc.). Even the clutch locking device, which allows to disconnect the wheels of the same pseudo-axle while the vehicle is running a curve, is modelled by means of a force element with an appropriate torque input function.

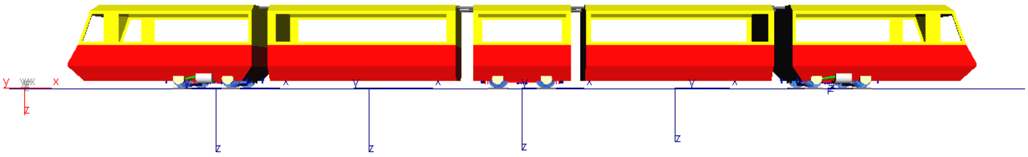

Fig. 53 Multibody model of Tram Sirio

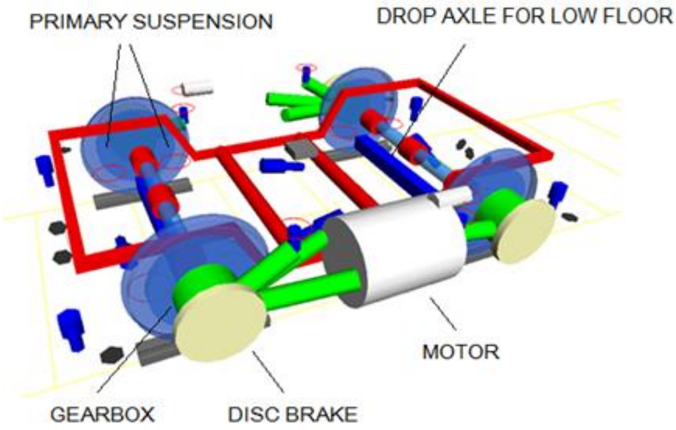

Fig. 54 Multibody model of the bogie

In the multibody simulations a real mission profile of the vehicle has been considered. The real speed profile used in dynamic simulations is shown in Fig. 55.

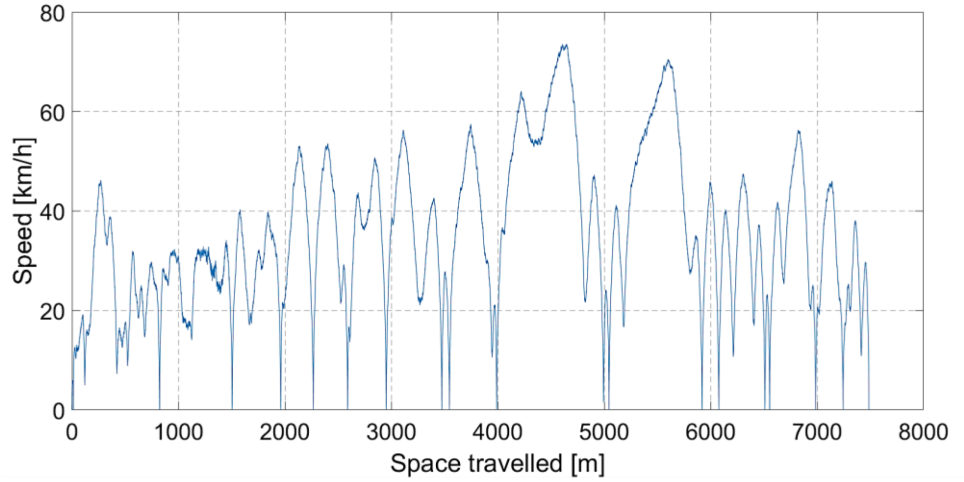

Fig. 55 Vehicle mission profile

Furthermore, the multibody model trustworthiness has been verified following some of the principles of EN14363:2016 [28]. In particular, load distribution (see Fig. 56) and lateral wheelset acceleration has been considered. The model validation, in terms of lateral acceleration, has been carried out comparing simulated data related to multibody simulations performed in a small radius curve (R=140 m) and in a large radius curve (R=600 m) and those experimentally evaluated on all vehicle wheelsets. The comparison between experimental data (red line) and simulated ones (blue line) for wheelset 1 (motor bogie) and wheelset 3 (trailer bogie) as visible in Fig. 59 and Fig. 58, has shown a good agreement proving the accuracy of the vehicle multibody model.

Fig. 56 Vehicle model validation - load distribution

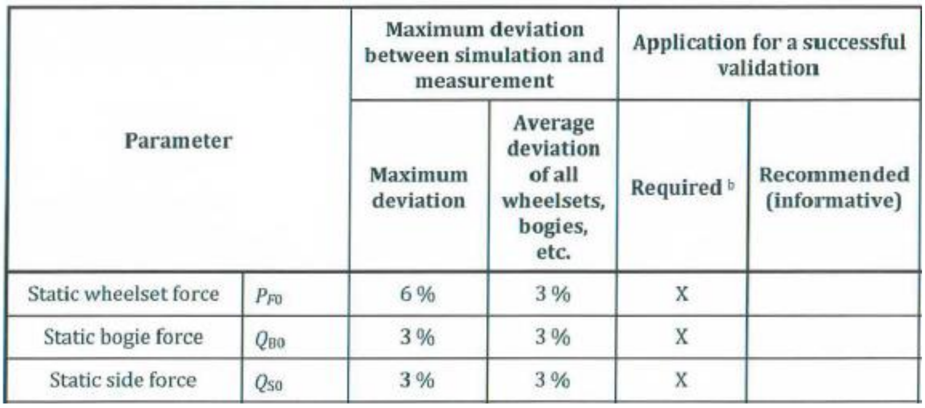

Parameter		Maximum deviation between simulation and measurement		Application for a successful validation	
		Maximum deviation	Average deviation of all wheelsets, bogies, etc.	Required [b]	Recommended (informative)
Static wheelset force	P_{F0}	6 %	3 %	X	
Static bogie force	Q_{B0}	3 %	3 %	X	
Static side force	Q_{S0}	3 %	3 %	X	

Fig. 57 Extract from EN14363: parameters for model validation

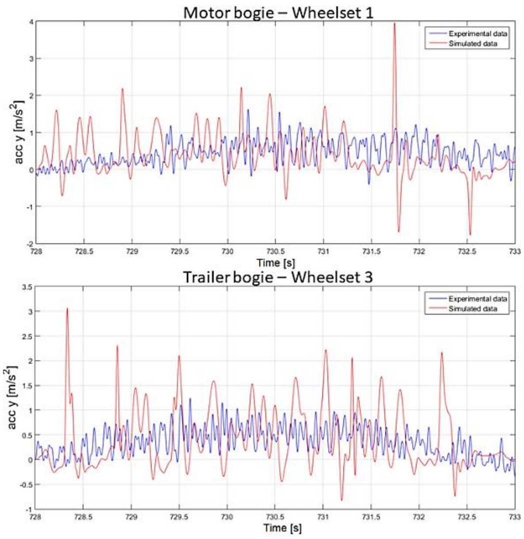

Fig. 58 Vehicle model validation - lateral acceleration comparison (R=600 m)

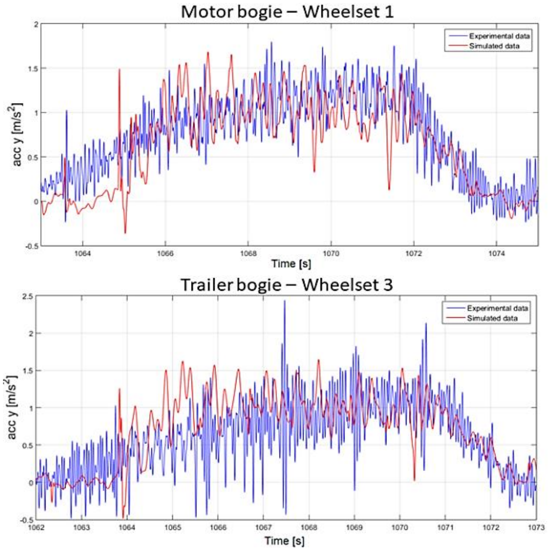

Fig. 59 Vehicle model validation- lateral acceleration comparison (R=140 m)

5.2. Wear

To assess the model reliability a validation against measurements acquired on field has been carried out. Both for the wheel and for the rail, the wear evolution in terms of reference quotas, has been taken into account. Furthermore, thanks to a special measurements campaign with an innovative 3D laser scanner, a comparison also in terms of rail profile shape evolution has been possible. In the following paragraphs the validation of the wear part of the tool will be discussed, analysing separately the evolution of the wheel and the rail.

5.2.1. Wheel

The wear model validation is carried out comparing the measured wheel reference parameters to the numerically evaluated ones (flange height Hb, flange thickness Lbe and flange steepness Qr – see Fig. 60). The reference quotas allow the estimation of the wheel profile evolution without necessarily knowing the whole profile shape and then to establish when the worn wheel profile must be re-profiled because it does not guarantee the dynamical stability of the vehicle anymore. The reference quotas for the Florence Tram Line are defined as follows:

- the reference point C, which defines the nominal rolling circumference, is evaluated on the profile at 44 mm from the internal vertical face of the wheel;
- the flange height Hb is the vertical distance between C and the flange vertex;
- the flange thickness Lbe is the horizontal distance between the internal vertical face and the point on the flange identified by the line 10 mm above the point C;
- the flange steepness Qr is the horizontal distance between the point defined in the previous bullet point and the point 2 mm under the flange vertex.

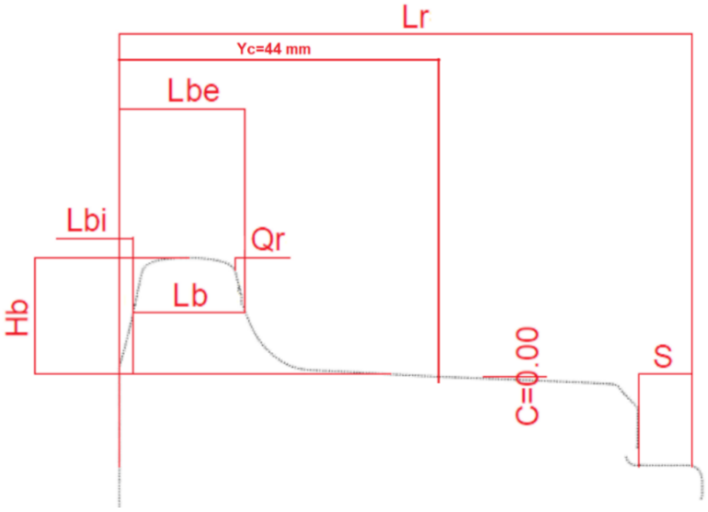

Fig. 60 Tram wheel reference parameters

Table 5 Tram Sirio reference quotas limits

	Quota	Warning [mm]	Accepted [mm]
Measurement	**Hb**	15.00 - 16.40	16.50 – 18.90
	Lb	13.00 – 16.50	16.50 – 20.60
	Lbe	17.90 – 20.40	20.40 – 22.80
	Lbi	3.50 – 4.90	2.30 – 3.50
	Qr	1.00 – 1.70	1.70 – 2.45
	Gauge		1380.50 – 1383.50

The values of these parameters are measured periodically to determine if the profile has to be re-turned or not, according to the maximum or minimum values specified in the maintenance plan (see Table 5). As regards their physical meaning, both the flange thickness Lbe and the flange height Hb describe the size of the flange: variations of the first quota are due to the action of the wear which progressively reduces the thickness of the flange and its structural resistance, while the rise of the flange height is a measure of the wear on the tread. The QR quota is a shape parameter which quantifies the local conicity on the flange. Although the performance in terms of dynamic behaviour depend on the coupling between the wheel and rail profiles rather than just the wheel profile, the check of the reference quotas aims to guarantee an acceptable running behaviour.

The experimental data, provided by Hitachi Rail Italy and Gest SpA, come from tests performed from March 2012 to November 2016 on the Sirio Firenze vehicles and consist of the wheel wear control parameters measured as a function of the mileage travelled by the vehicle. The vehicle is equipped with 84 mm wide wheel with UNI3332 profile running on 60R2 rail profile. The data are related to all the wheels of the entire fleet (17 vehicles) and it was necessary to make a selection to consider only the measurements of the reference parameters evaluated in a period between two turnings, during which the profiles are not re-established. According to this strategy, it has been looked for a bogie which had a sufficient number of measurements of the reference parameters. Then, it has been selected the leading motor bogie (CM1 in Fig. 56) of the vehicle n°1014 and the trailer bogie CP3 of the vehicle n°1004 whose related measured data goes from April 2015 to May 2016. For the model validation, the experimental reference parameters related to the leading axles of the chosen bogies have been considered. The corresponding values for the left and right wheel are given in Table 6. Looking at Fig. 61 and Fig. 62, where the reference parameters are plotted against the mileage travelled by the vehicle, it can be noticed the almost symmetrical wear evolution between left and right wheel due to the operating conditions of the vehicle. In fact, the tram is periodically turned during the service. Since that, it is reasonable consider the wheel evolution between left and right side symmetrical during the numerical simulation. As starting wheel profiles for the wear and RCF simulations, real measured profiles (acquired at the same time of the reference parameters first measurement) have been implemented within the multibody model of the vehicle (see Fig. 63 for the wheel of the wheelset 1).

Table 6 Experimental wheel wear parameters

CM1 Wheelset 1

Mileage [km]	Left [mm]			Right [mm]		
	Hb	**Lbe**	**QR**	**Hb**	**Lbe**	**QR**
0	18.83	20.43	1.76	18.84	20.68	1.78
15684	18.71	20.08	1.78	18.63	20.41	1.61
35387	18.57	19.92	1.64	18.47	20.31	1.55
52386	18.52	19.88	1.74	18.4	20.45	1.59
70156	18.39	19.87	1.82	18.26	20.17	1.68

CP3 Wheelset 3

Mileage [km]	Left [mm]			Right [mm]		
	Hb	**Lbe**	**QR**	**Hb**	**Lbe**	**QR**
0	19.11	20.40	2.27	18.95	20.45	2.14
17599	19.16	20.57	2.1	19.02	20.53	2.00
35327	19.24	20.01	2.11	19.05	20.25	1.96
52680	19.17	19.57	2.15	18.99	20.19	1.98
70216	19.01	19.44	2.1	18.8	19.96	1.85

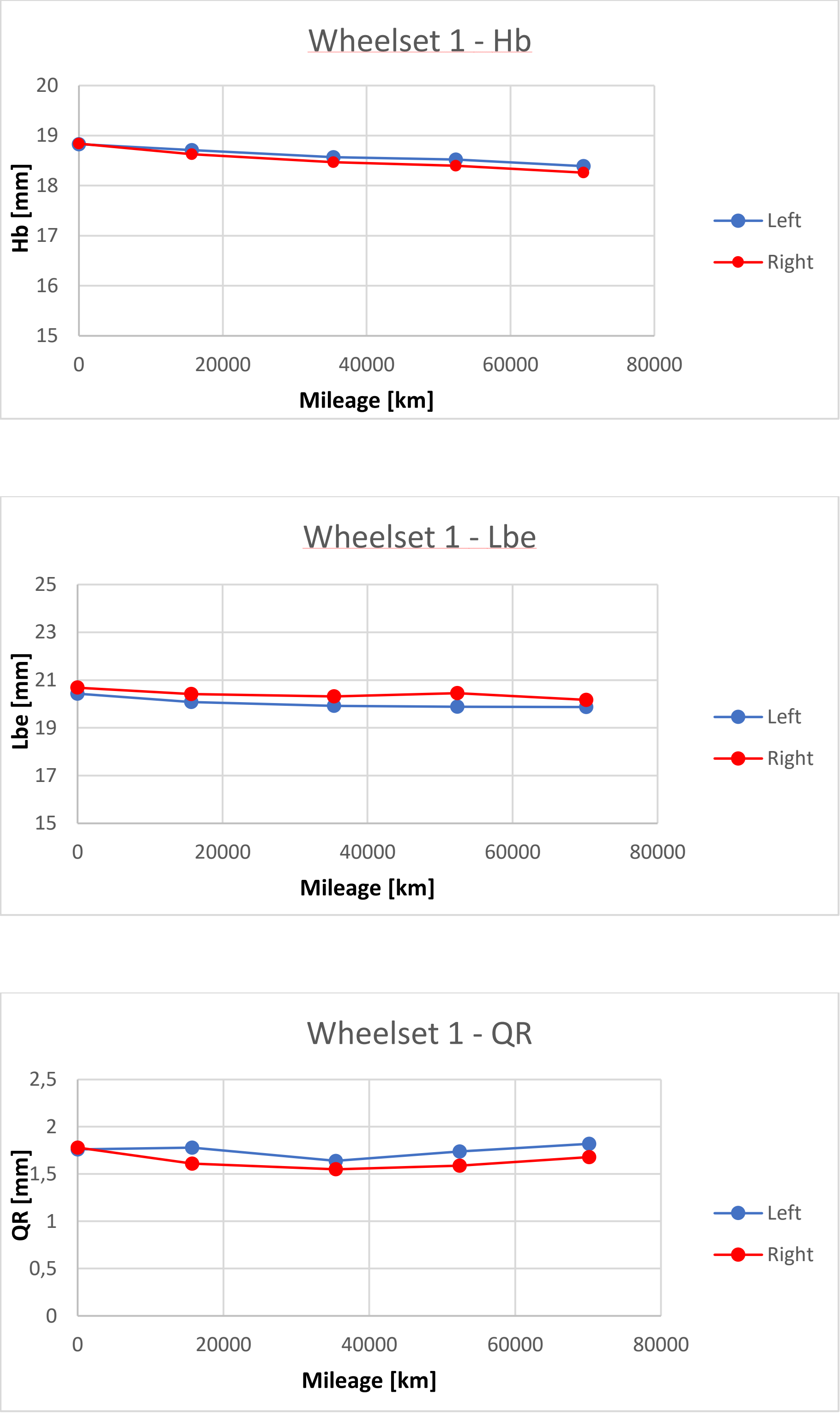

Fig. 61 Plot of experimental wheel reference parameters of the first wheelset as a function of the mileage

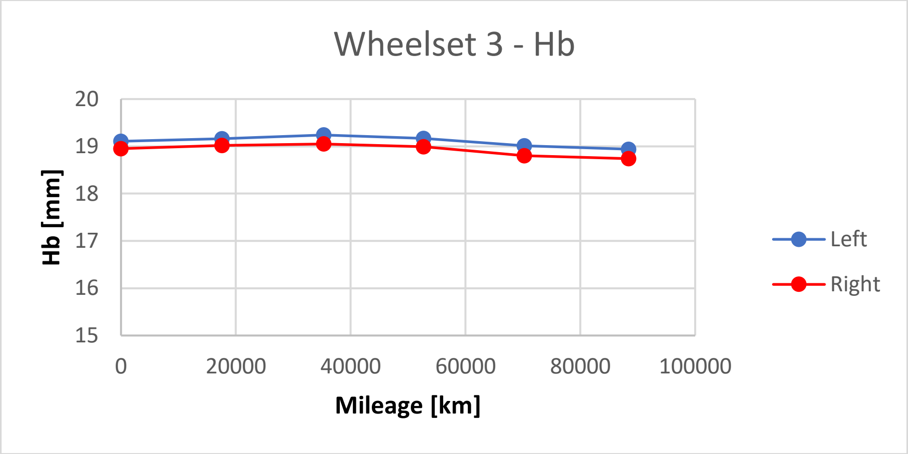

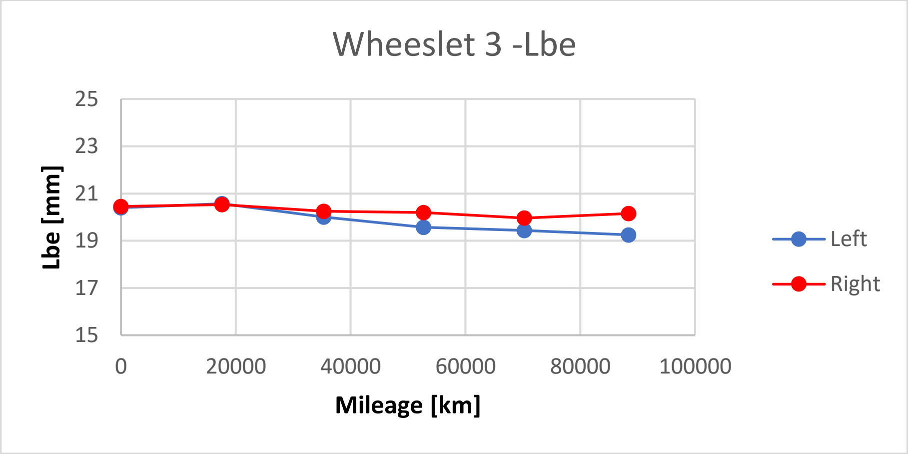

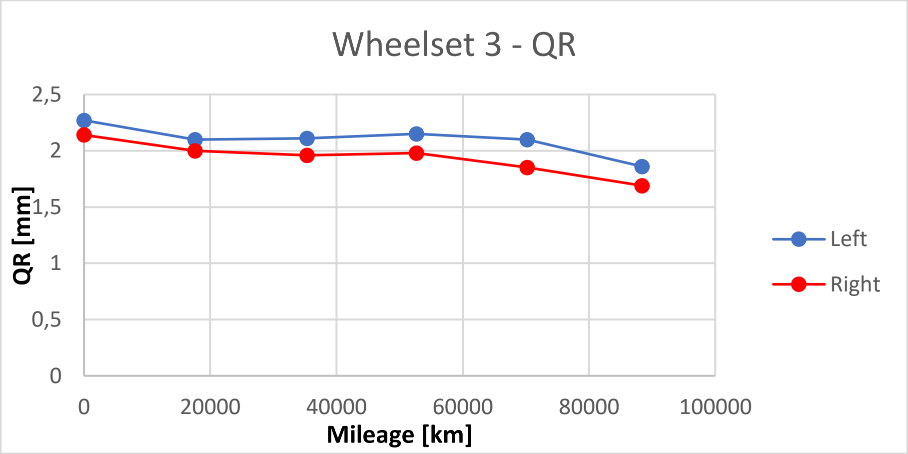

Fig. 62 Plot of experimental wheel reference parameters of the third wheelset as a function of the mileage

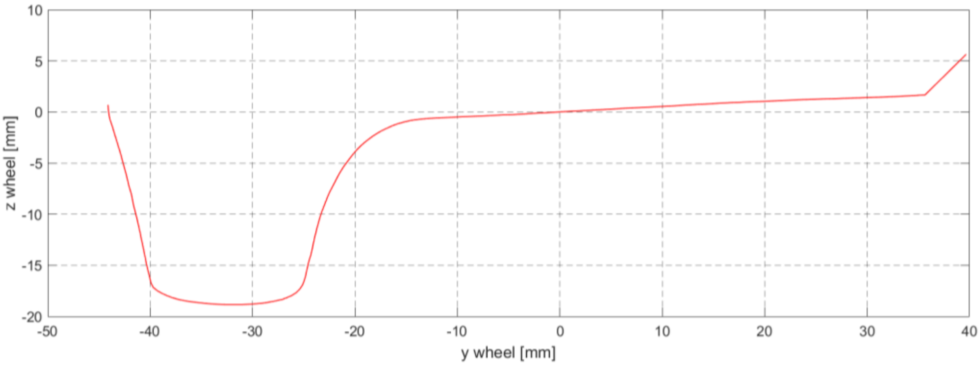

Fig. 63 Starting profile of the wheel – CM1 wheelset 1

According to the update strategy described in 2.3.3, the threshold value (see Table 7) on the maximum thickness of material removed by wear on the wheels at each wheel discrete step has been chosen equal to 0.4 mm. Instead, for the rail a threshold value of 0.8 mm has been set. Therefore, when the removed material reaches this quantity, a discrete step finishes and the whole procedure passes to the following discrete step. In Table 7 the number of discrete steps and the adopted threshold values for the wheel and the rail profiles are summarized.

Table 7 Wear loop parameters

	N° of discrete step	**Threshold value**
Wheel	5	0.4 mm
Rail	1	0.8 mm

The evolution of the wheel wear control parameters obtained after the 5 wheel steps (from new unworn wheel up to totally worn wheel reached in 81 088 km) of the first general rail step (new unworn rail) of the iterative procedure is here compared to the experimental data.

The reference quotas evolution both for the wheelset 1 and wheelset 3 is represented in Fig. 64 and Fig. 65 as a function of the mileage.

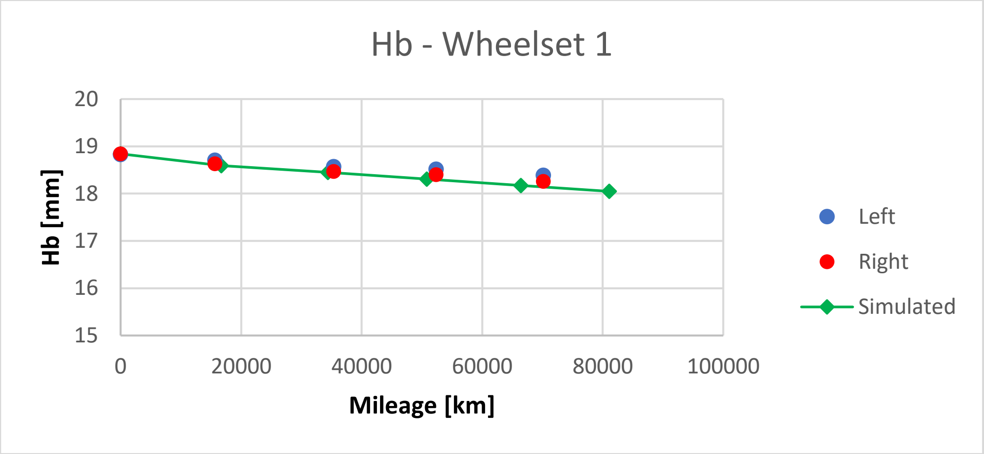

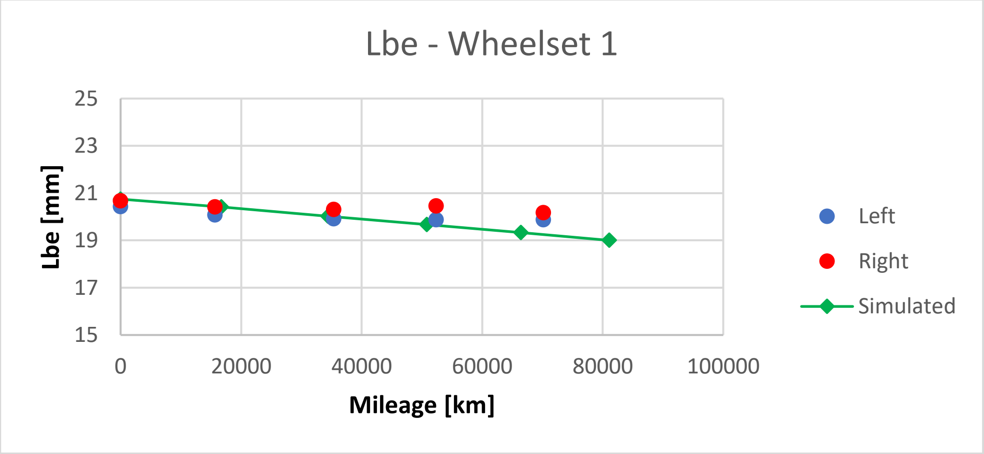

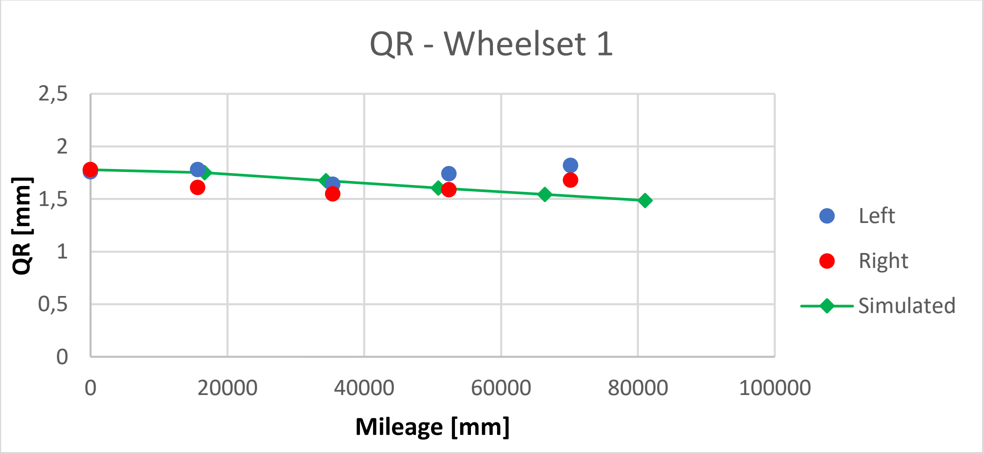

Fig. 64 Reference parameters comparison at first rail step – wheelset 1

Fig. 65 Reference parameters comparison at first rail step – wheelset 3

Considering the flange height trend, it can be noticed how it decreases due to the flange tip running motion and the low wear rate on wheel tread. Contrary to railway applications, a tram vehicle has a particular behaviour when it runs on switches and crossings, called flange tip running (Fig. 66). The groove of the rail is filled up to a certain level and the wheel runs on the flange tip over the crossing gap without any contact between wheel tread and the rail. Once the crossing gap is passed, the groove is gradually deepened back to its normal depth. The main consequence is a flange tip wear that is not present on a conventional train wheel.

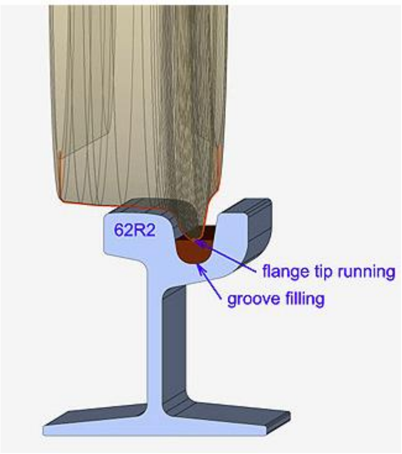

Fig. 66 Flange tip contact

The progress of Lbe dimension and the Qr factor trend are also shown in Fig. 64 and Fig. 65. The comparison had shown a good agreement between the outputs of the wear model (continuous green lines) and the experimental data (red and blue dots), both for the flange dimension (Hb, Lbe) and for the conicity (Qr). Fig. 67 shows the evolution of the whole wheel profile due to wear (leading wheelset): the removed material is mainly localized on the flange zone due to the presence of several narrow curves typical of a tramway scenario. The flange tip wear, as already said, is caused by the flange tip running motion that occurs when the tram vehicle runs over switches and crossings.

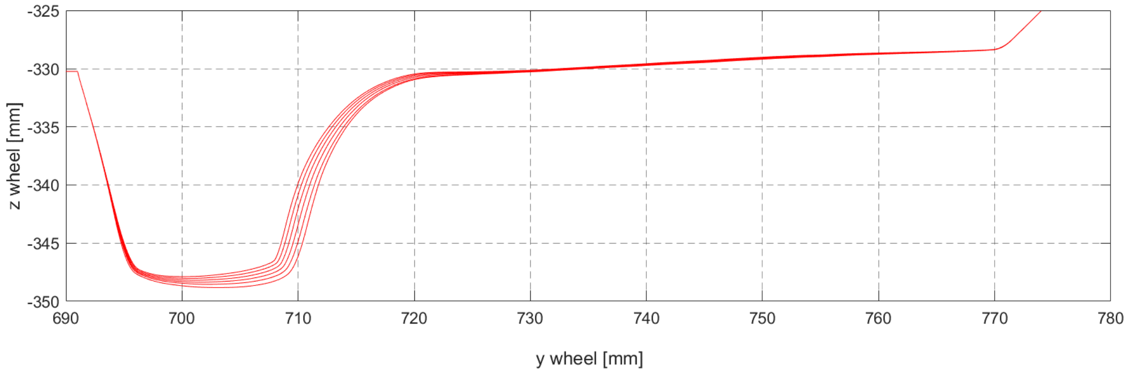

Fig. 67 Simulated wheel profile evolution at first rail step – Motor bogie CM1 - leading wheelset

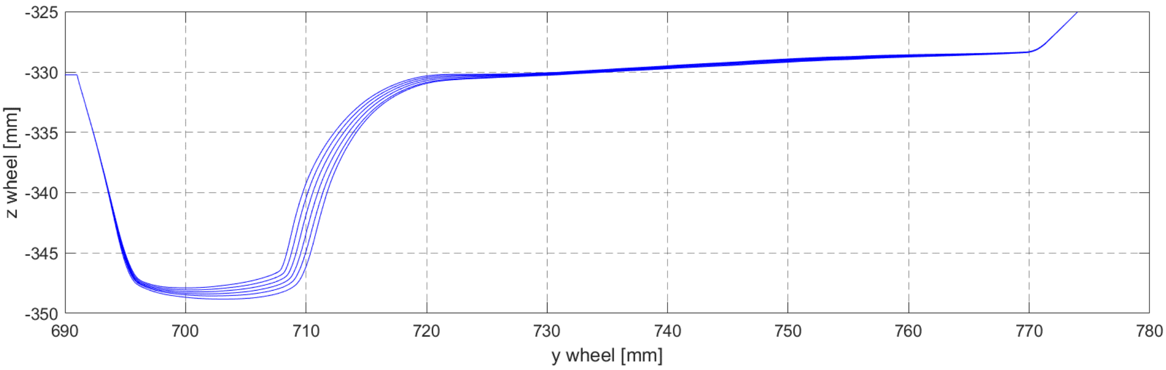

Fig. 68 Simulated wheel profile evolution at first rail step – Trailer bogie CP3 - leading wheelset

5.2.2. Rail

The wheel wear and RCF evaluation has been assessed considering the entire real track, implemented in the multibody software, of the tramway line. When the wear analysis has to be carried out on a set of tracks of considerable length by using, at the same time, accurate models for the vehicle and the wheel-rail contact, the utilization of "railway line statistical model" may be an indispensable way to overcome a series of problems due to the computational times and the organization of the simulations themselves. The basic idea is to substitute a complex railway network or the too long tracks to be simulated with a set of simpler tracks representative of the railway network which can produce an equivalent amount and distribution of wear both on the vehicle wheels and on the rail tracks. For these reasons, the simulation campaign for rail damage assessment has been carried out considering a set of curves (characterized by a minimum Rmin and a maximum Rmax radius) and a straight track obtained from a statistical analysis of the real track layout of the Florence Tram line 1. With reference to Table 8, the set consists in Nc = 7 distinct elements (6 real curves and a straight line) characterized by the radius Rc, the traveling speed V and the statistical weight Pk (with 1 ≤ k ≤ Nc). The latter is calculated as the ratio between the track length of curved sections related to the k-th class and the total railway track length and represents the frequency with which each curve appears on the considered tramway track. The radius Rc are calculated by means of the weighted mean on all the curve radii included in the corresponding class (the weighted factor is the length of the curves in the real track). All the curved tracks considered to study rail evolution are shown in Table 8. Then, as output of the damage tool, the rail profile evolution and RCF growth for each curves of the set have been obtained.

Table 8 Data of the curvilinear and straight tracks of the statistical analysis

Class	Rmin [m]	Rmax [m]	Rc [m]	V [km/h]	Pk [%]
1	600	1600	1084	50	5
2	250	600	342	50	5.1
3	77	250	149	34	10.17
4	45	77	50	20	1.71
5	45	32	38	17	1.56
6	25	32	26	14	1.75
7	1600	∞	∞	50	75.38

Before to proceed with the simulations, a quantitatively comparison between the results obtained with the complete railway line (as done for the wheel) and the statistical approach with a set of 7 different classes of curves has been performed to verify the trustworthiness of the adopted approach. In Fig. 69 the reference dimensions trend of the first axle both for the statistical and the whole track analysis are shown. The reference dimension comparison shows a good consistency between the two approaches.

The same update strategy and threshold value reported in Table 7 on the maximum thickness of material removed by wear on the wheel at each wheel discrete step has been used, while for the rail, to better appreciate the profile shape variation a smaller step was set equal to 0.4 mm.

Table 9 Wear loop parameters

	N° of discrete step	Threshold value
Wheel	5	0.4 mm
Rail	5	0.4 mm

In Fig. 70, Fig. 71 and Fig. 72 the rail profile shape evolution respectively for a large, medium and narrow radius curve is shown. It can be observed how narrower is the radius and more important is the damage due to wear due to the increase of the contact forces at wheel-rail interface.

In Fig. 70, Fig. 71 and Fig. 72, the rail profile evolution related to a large, medium and narrow radius curves of the Florence tramway line after 5 rail discrete steps of the wear loop corresponding at a total tonnage of 5.12 Mt (see Table 10) calculated as Mtot = Ntot *Mv is shown. The removed material is mainly localized on the rail flank zone and rises up with the decrease of the radius.

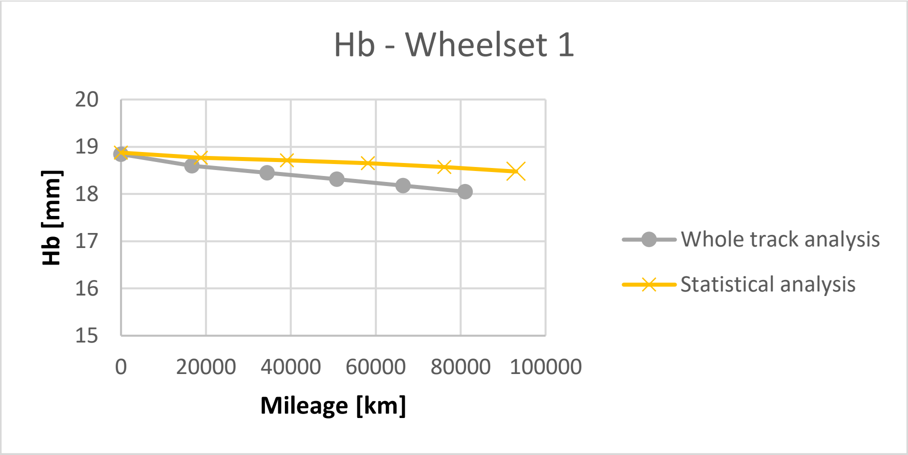

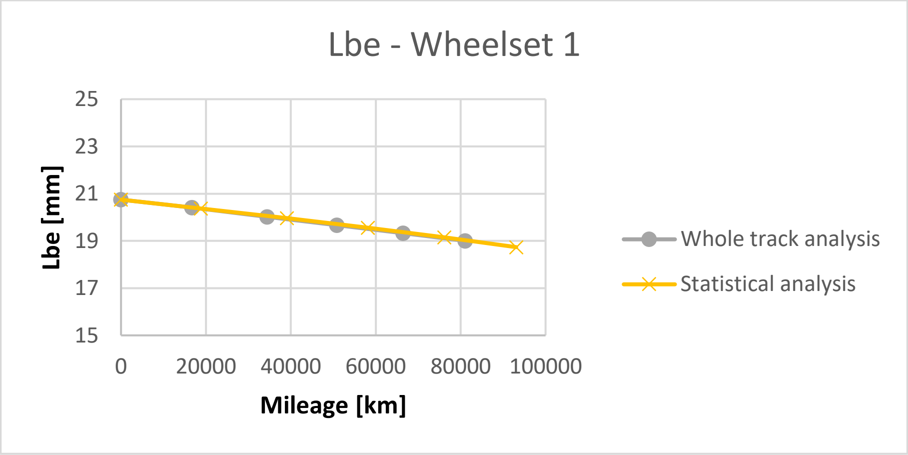

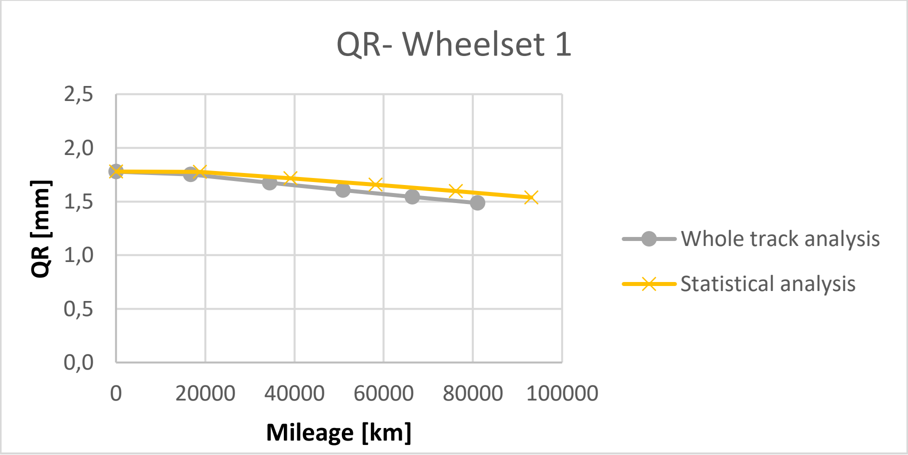

Fig. 69 Wheel reference parameters - Whole track vs statistical analysis

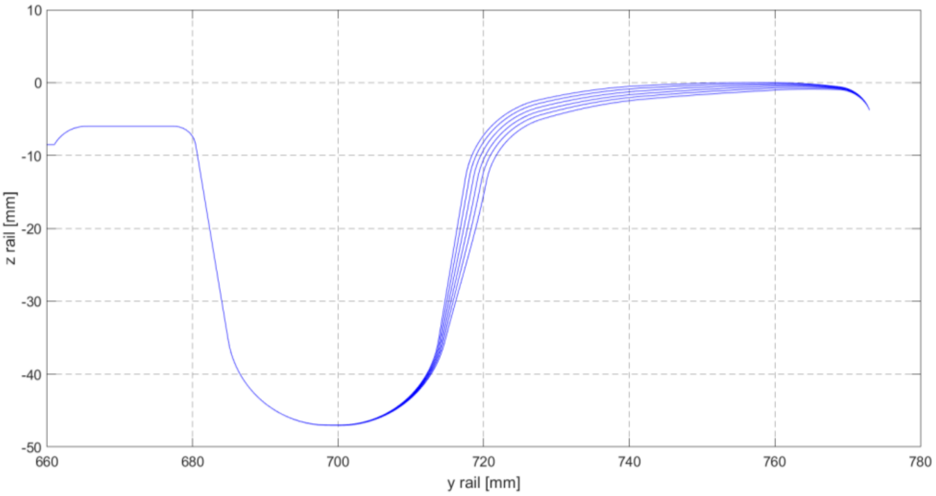

Fig. 70 Rail profile evolution – Curve R=38 m

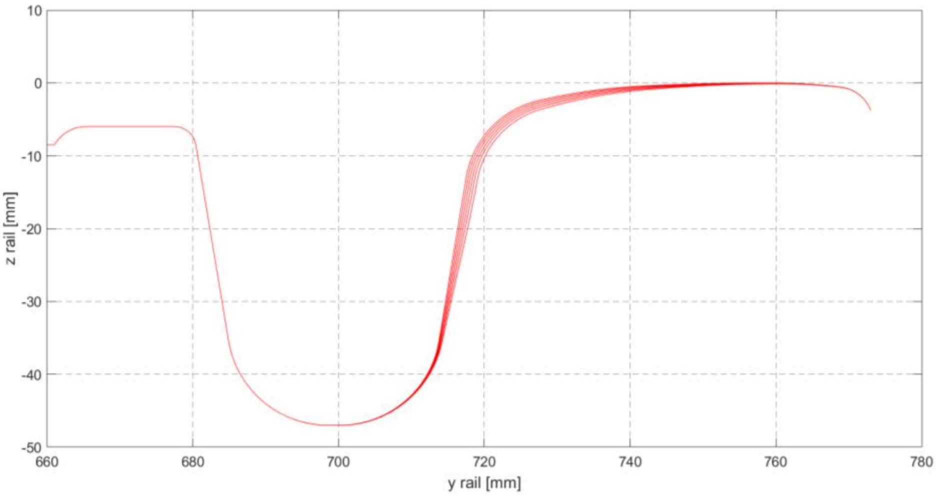

Fig. 71 Rail profile evolution – Curve R=149 m

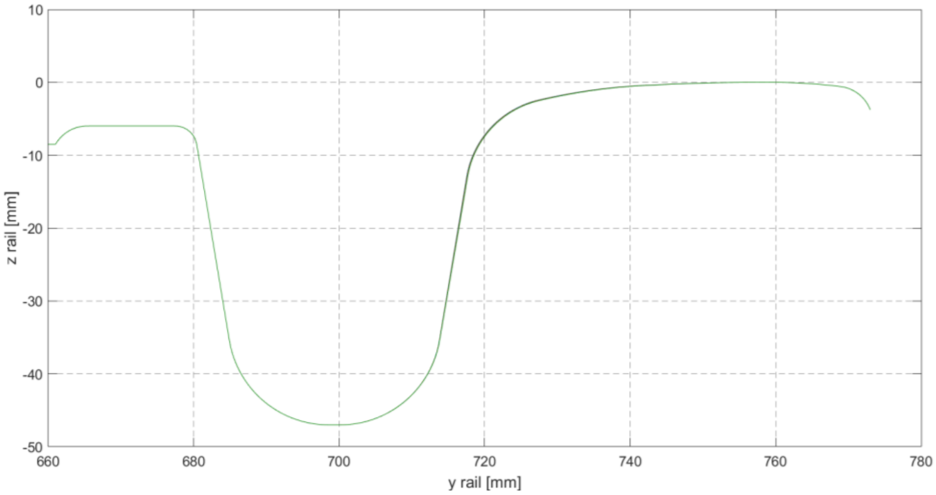

Fig. 72 Rail profile evolution – Curve R=1084 m

Table 10 Total tonnage burden on track

Total vehicle number (Nv)	Vehicle mass (Mv) [t]	Total tonnage [Mt]
93 702	54.7	5.12

To evaluate the evolution of rail wear, two additional control parameters have been introduced: the QM quota and LW quota (see Fig. 73). The QM is defined as the rail head height in the point y_r = 759 mm with respect to the centre line of the track. The value of y_r depends on the railway gauge (equal to 1435 mm in the Florence Tram line 1) and on the laying angle of the track. Physically the QM quota gives information about the rail head wear. The LW quota is defined as the lateral wear depth evaluated along a line with 45° slope as shown in Fig. 73.

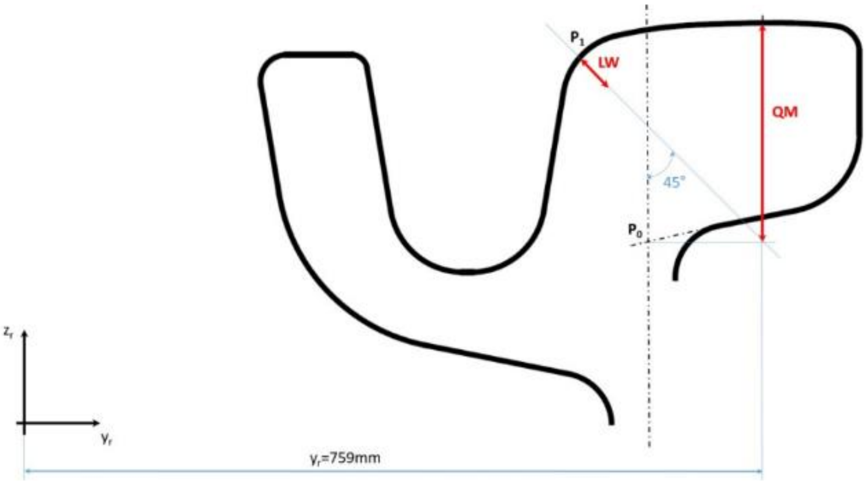

Fig. 73 Definition of rail wear control parameter

In Fig. 74 the QM progress of the three reference curves seen previously, is plotted as a function of the number of vehicle running on the line. The QM trend shows that the head rail wear increases if the curve radius decreases according with the real wear phenomena.

In Fig. 75 the lateral wear LW trend is shown. In this case too, the lateral wear increase with the curve radius reduction.

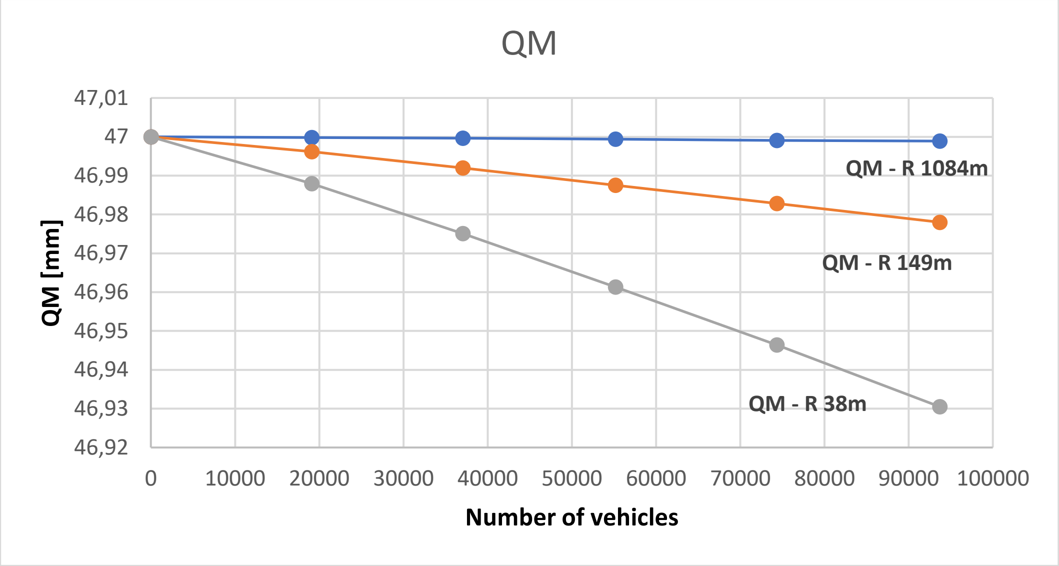

Fig. 74 QM dimension progress

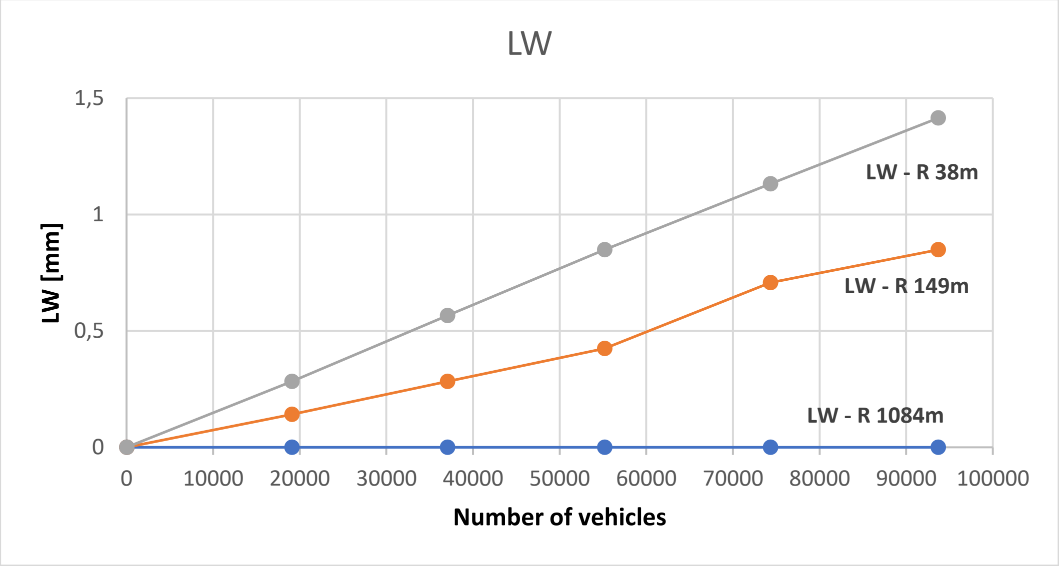

Fig. 75 LW dimension progress

5.2.2.1. New innovative measuring instruments

To validate the model, the work was focused on the wear assessment of the most critical curve in the line, investigated using measured data obtained from an innovative measuring procedure which use a 3D optical scanner. This part of Ph.D. work has been carried out in collaboration with the University of Perugia. Because of the importance of rail and wheel conditions, their health status is constantly monitored by means of different measuring instruments. Currently, many digital wear measurement methods exist and, in general, they can be classified as direct and indirect [82][83]. Direct methods are used when the direct access to the worn surface is possible optically or by contact while, when the access is impossible, indirect methods are used. The latter methods do not measure directly wear but they measure specific quantities which are caused by wear (for example heat, noise, vibration, etc...) and which can be put in relationship with wear, by means of analytic formulas [82][83].

Direct methods range from visual inspection and 2D contact profilometer to the most recent and innovative 2D/3D optical scanners. Currently, 2D wear measurements are the most used to check wheel and rail wear condition. They use a mechanical sensing probe (2D contact profilometer, [82][84][85][86]) or a laser beam (2D optical profilometer, [82]) to detect a set of reference parameters which are representative of the wear status of the entire wheel and rail profiles geometry. However, most of them do not allow an accurate assessment of specific 3D wear phenomena such as corrugation, plastic deformations, etc. The most recent devices exploit 3D laser systems to detect wheel and rail surfaces in terms of Cartesian coordinates and polygonal meshes and, thanks to the continuous improvement of laser scanning technology, a higher degree of accuracy and efficiency can be reached, allowing a more complete analysis of the wear conditions over the whole component surfaces [82][87]. Thanks to their great versatility, reliability and accuracy, the use of these measuring instruments is highly suggested especially with a complex shape sample. Furthermore, some 3D optical scanners have the advantage of being portable, allowing to scan undercuts and complex geometries in a simple way [84][88] and without dismounting the components from their exercise environment. This way, it is possible to generate a full 3D digital model of the specimen and to accurately compare it to the unworn geometry, getting the final 3D distribution of material removed by wear. The resulting 3D wear maps allow also the measurement of several wear parameters, which would be unappreciable by 2D measurements. Thus, a complete scenario of the wear phenomenon can be achieved.

Then, an accurate validation of the proposed model has been carried out against experimental rail wear data acquired using a new non-contact portable metrological 3D laser scanner on a curved section of the Florence tramway line. The reference section is part of the narrowest curve of the whole network (named A-V08), the most critical in terms of wear, due to its small radius (equal to 25 m). The curve layout is shown in Fig. 76. The vehicle runs through the curve at a speed of 14 km/h. The wear trend numerically evaluated in terms of 2D rail profiles will be compared to the experimental one, and consequently to the 3D wear maps of the worn rails. For the sake of completeness, the wear reference parameters acquired by the classical

2D contact profilometer (currently used in the Florence tramway line) will be also considered to get a more robust validation of the proposed model.

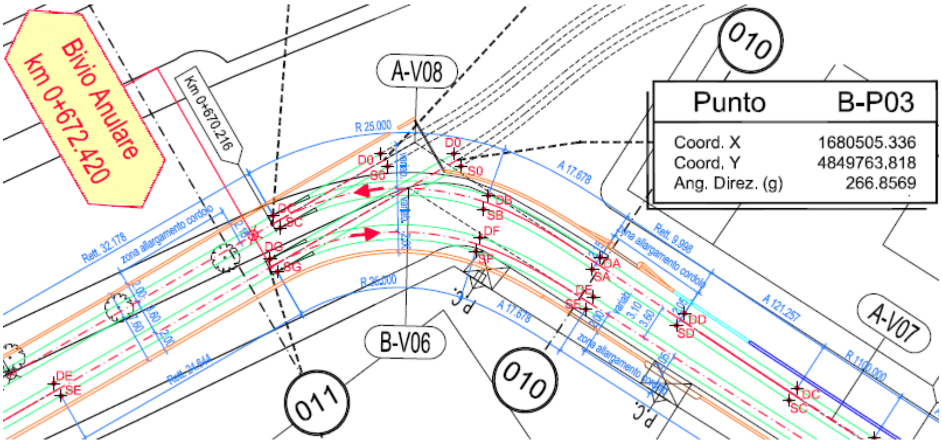

Fig. 76 Curve A-V08 layout

The new measuring instrument used was the optical noncontact 3D laser scanner HandySCAN 700 produced by Creaform Inc (Levis, Quebec) (see Fig. 77), suitable for a wide range of industrial applications and engineering services [89][90][91][92]. It is completely portable, easy to handle and to use but characterized by a very high accuracy and reduced data processing time. Moreover, it allows also the scan of reflecting objects. The main technical specifications are shown in Table 11. The 3D acquisition software VXelements is directly embedded on board and allows the real time 3D reconstructions of any shapes without further additional data editing procedure. The scan is performed by positioning physical targets on the object and/or on the scene, to build a reference positioning model. The following wear mapping and inspection procedure were performed by means of VXmodel and VXinspect, integrated in VXelements software suite. The first one enables 3D scanned data to be used directly in any CAD software, optimizing and cleaning the acquired mesh and applying reverse engineering procedures. The latter allows complete inspection procedures by direct comparison between the scanned part with the nominal CAD project or with the imported mesh of the unworn part to obtain the wear distribution.

Before carrying out the experimental campaign on the real track, to preliminarily test the acquisition procedure, a detailed laboratory analysis has been performed on a straight 500 mm length rail section manually worn out (see Fig. 78). First of all, the scanned unworn rail was compared with the reference CAD model to prove the quality of the considered rail section. Then, the scanned worn rail portion was compared with the reference CAD model to evaluate the wear of the surface. Finally, the two unworn and worn scanned rail sections were compared to reproduce the real on track acquisition procedure.

Fig. 77 HandySCAN 700

Table 11 HandySCAN 700 technical specifications

Measurement range	480000 measures/s
Light source	7 laser cross (+ 1 extra line)
Resolution	0.050 mm
Accuracy	0.030 mm
Volumetric accuracy	0.020 mm + 0.0060 mm/m
Stand-off distance	300 mm
Depth-of-filed	250 mm

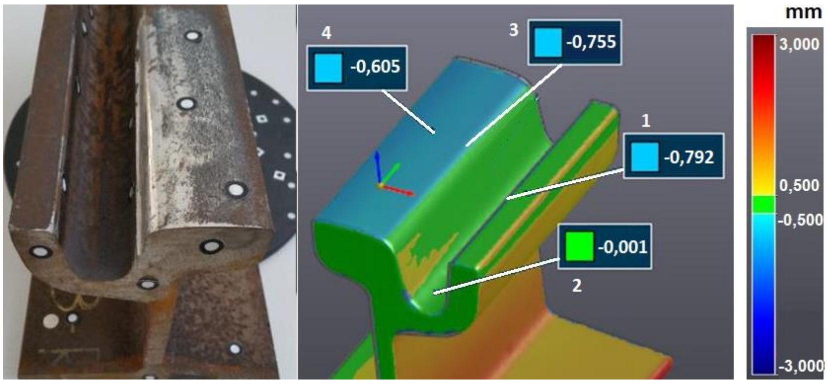

Fig. 78 Rail section used in laboratory analysis to preliminarily test the acquisition procedure

The measuring campaign with the 3D optical scanner started by placing a set of physical targets close to the rail in order to create a positioning model, made of reference points. After the generation and also optimization of the reference model by software tools to enhance the accuracy, the scanning procedure was performed by HandySCAN 700 generating the 3D model of the rail in real time (Fig. 79).

Fig. 79 3D optical scanning campaign

Two measurement campaigns using the optical scanner have been performed on March 10th and on September 26th 2016 and the scanned rail surfaces have been used to validate the model in terms of rail shape evolution. During the considered time period, no grinding operations have been done on the track. The results of the acquisitions are saved as mesh files in a .stl format and then converted to a step file by means of an ultra-accurate reverse engineering procedure, based on a perfect fitting of parametric surfaces onto the measured mesh. The resulting 3D models of the rails related to the two acquisition campaigns have been cut by using orthogonal planes in the investigated zone of the curve. Subsequently, the unworn and worn 2D rail profiles are obtained from the intersection between the 3D scanned meshes of the rail and such reference planes. For the complete workflow see Fig. 80.

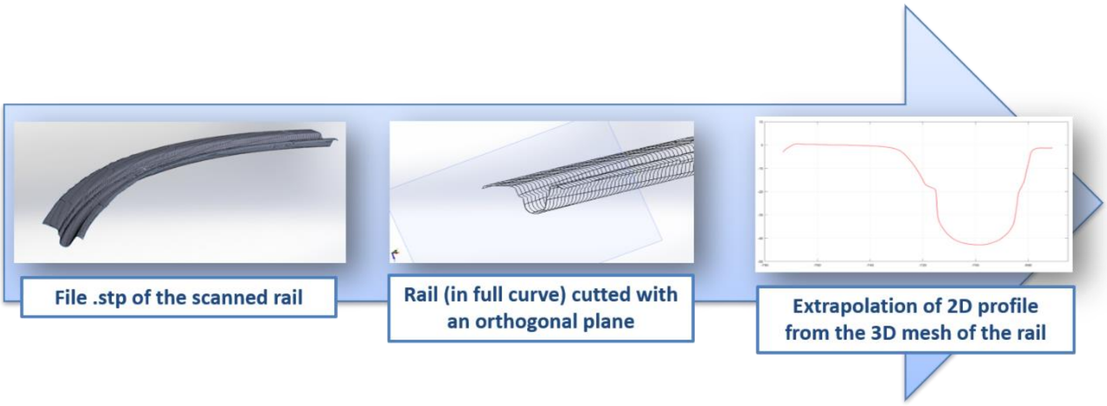

Fig. 80 Workflow to obtain 2D rail profiles starting from 3D surfaces

By way of example, the difference between the worn (acquired during the second measuring campaign carried out in September) and the unworn reference profile (reference CAD model) of the considered curve is shown in Fig. 81. The colour map highlights the different wear depths along the rail.

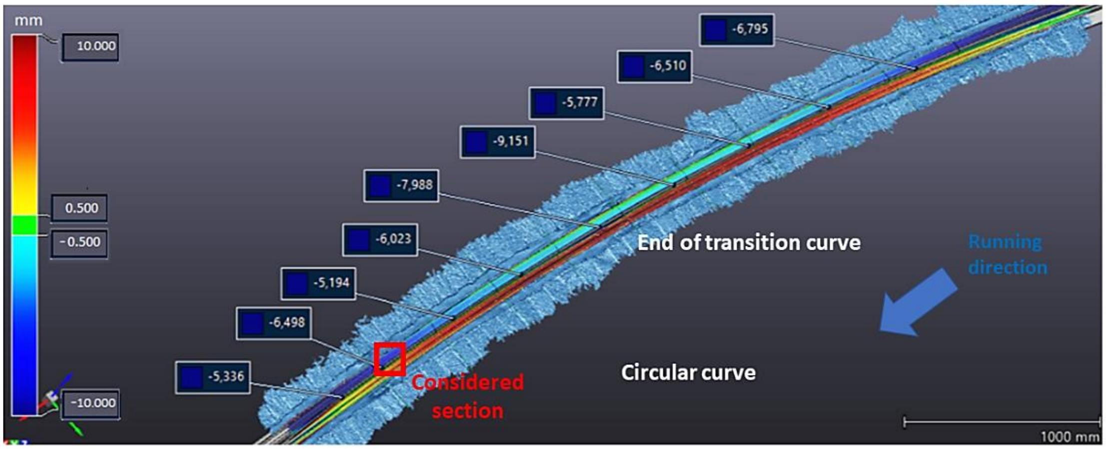

Fig. 81 Rail 3D wear map

Furthermore, the large amount and quality of the measured data could be better appreciated considering that the cross sections are taken every 100 mm. In Fig. 82, as an example, four cross sections of the considered curve are shown. From these sections, after a comparison between the nominal rail profile (reference CAD model) with the scanned one, it is possible to evaluate the tread, flange and check the rail conditions to get a clear and complete wear assessment. The red zone in the groove and on the checkrail top (red colour indicates positive wear values) are due respectively to the presence of sediments and oxides. The flange wear is higher especially in the central area of the rail where about 9 mm of removed material has been measured with reference to the nominal rail profile (reference CAD model). In the curves characterized by very narrow radius wear on the checkrail is present as well.

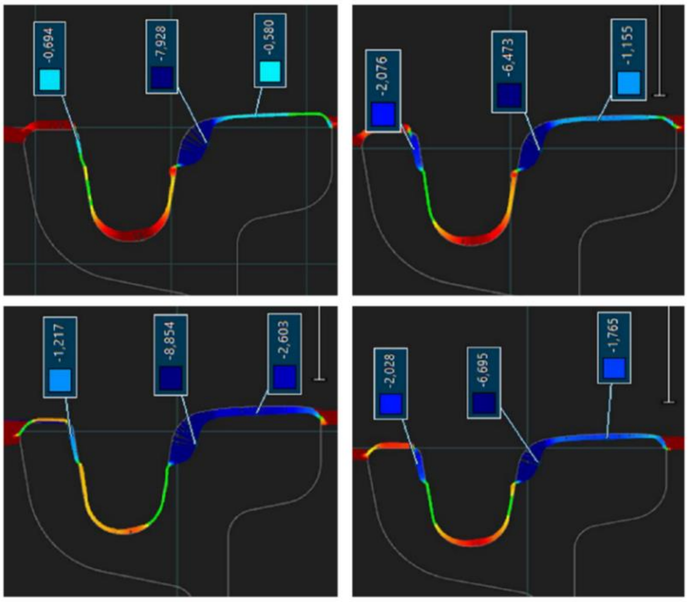

Fig. 82 Cross sections

Since the grinding operations in the considered scenario are "targeted" (i.e. the operator locates the spot along the rail where an addition of material is needed, according to the line maintenance plan previsions, he welds on it the new material and then he grinds to re-establish the rail profile), a specific 100 mm long section obtained by means of the procedure previously described and corresponding to the zone highlighted with a red square in Fig. 81, has been considered for the wear model validation. The considered rail section is shown in Fig. 83 for the first 3D scanner acquisition performed in March 2016 and in Fig. 84 for the second one, performed in September 2016. In Fig. 83 it is also possible to notice the 2D starting rail profile used in the simulations highlighted in (red).

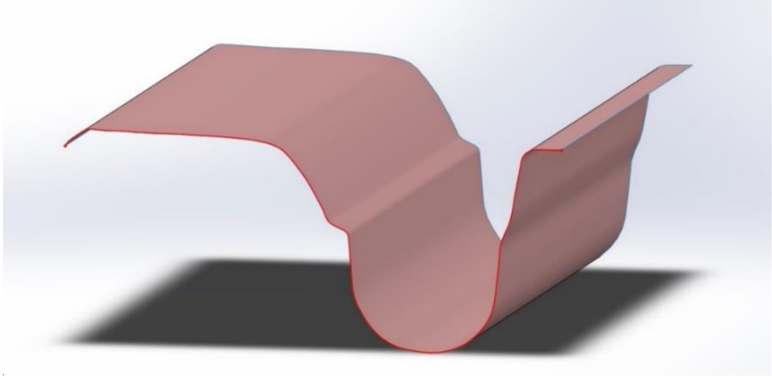

Fig. 83 Considered rail section related to the first measurement campaign

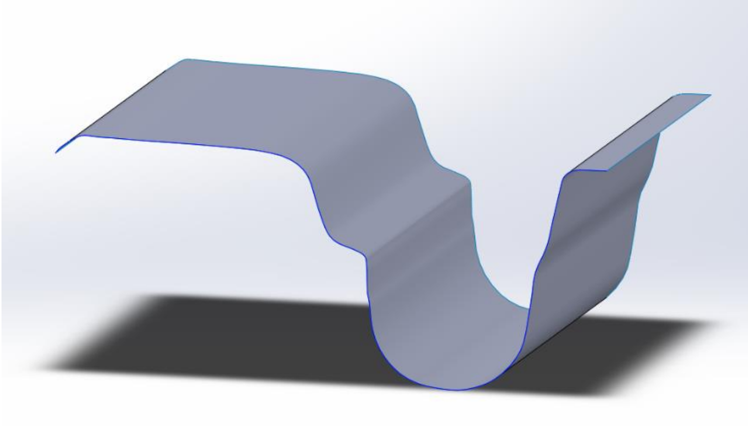

Fig. 84 Considered rail section related to the second measurement campaign

To have a clearer wear assessment, in Fig. 85 the distribution of wear on the surface of the considered section of rail is shown: in particular the difference measured in the normal direction between the two on-line scanner acquisitions is reported.

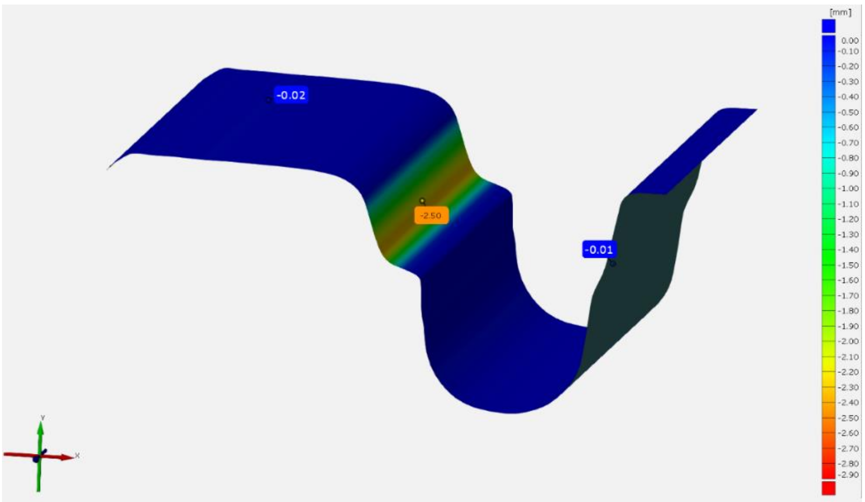

Fig. 85 Surfaces comparison between first and second measurement campaign

As said previously, the wear model validation has been carried out considering rail experimental data acquired by means of the new accurate 3D optical laser scanner and by a commonly used 2D measurement instrument to have a more complete model validation. As diagnostic systems, on the tramway line a contact profilometer is used to assess rail wear status (see Fig. 86). It is an electronic hand-pushed trolley able to measure the main wear reference parameters as a function of the travelled distance. In particular, lateral wear, calculated from the gauge measurement, has been considered because it directly provides the wear status of the track and by which the maintenance operations are scheduled. Three measurement campaigns have been performed, from March to September. According to the maintenance plan, during this period no maintenance operations have been done on the considered track section. Processing the measured data, during the considered time period, a lateral wear equal to 2.6 mm on the outer rail has been observed; the related trend is shown in Table 12. The model validation will be carried out taking into account both the lateral wear measured through the contact profilometer and the wear measurement acquired by means of the laser scanner to prove the model trustworthiness in terms of rail shape evolution.

Fig. 86 Contact profilometer

Table 12 Experimental lateral wear values

	March 2016	May 2016	September 2016
Lateral wear [mm]	0	1.3	2.6

In Fig. 87 the comparison between experimental and simulated 2D rail profiles obtained after 5 rail discrete steps of the wear loop is shown: the continuous red line corresponds to the first scan carried out in March 2016 (see Fig. 83) while the black one to the last scan performed in September 2016 (see Fig. 84). The blue dashed lines are the simulated rail profiles. The wear is mainly concentrated on the flank zone (see also the zoomed flank area in Fig. 88) and the simulated results show a good correspondence with the real wear evolution.

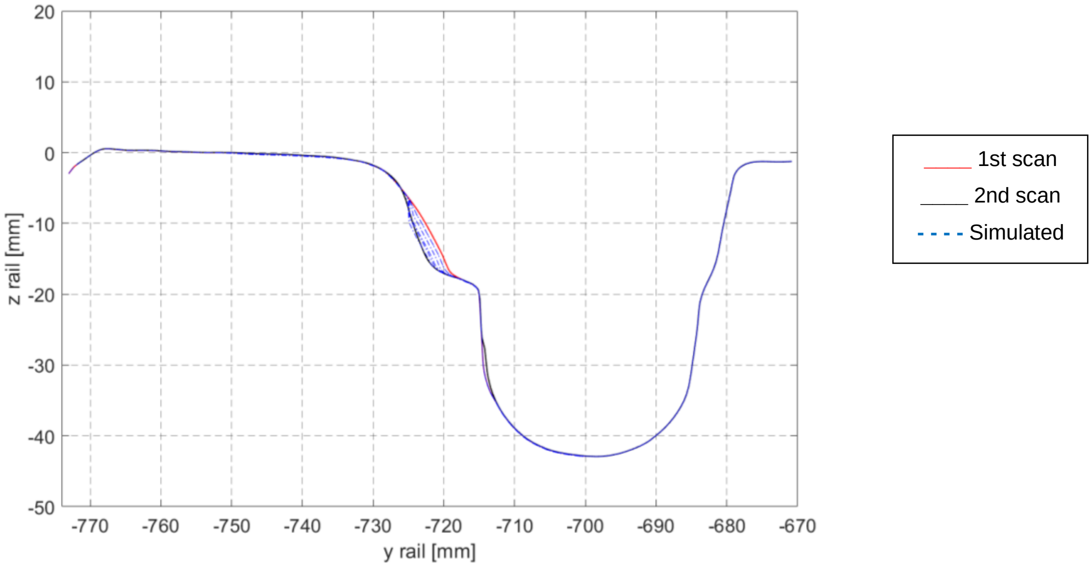

Fig. 87 Experimental and simulated rail profiles comparison

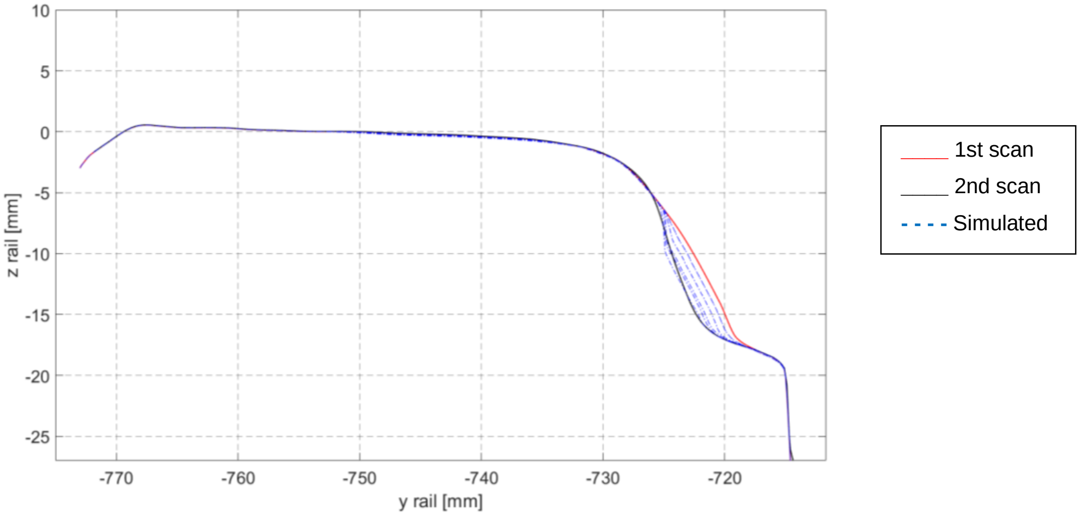

Fig. 88 Experimental and simulated rail profiles comparison – zoom on rail flank zone

In Fig. 89 the comparison between the lateral wear values obtained as output of the wear model and those measured through the contact profilometer and the optical 3D scanner is shown. The lateral wear amounts are plotted as a function of the number of vehicles running on the line, calculated considering the real timetable provided by the research partner GEST S.p.A (see Table 13 and Table 14). Also, in this case, the results obtained from the wear model can be considered satisfactory.

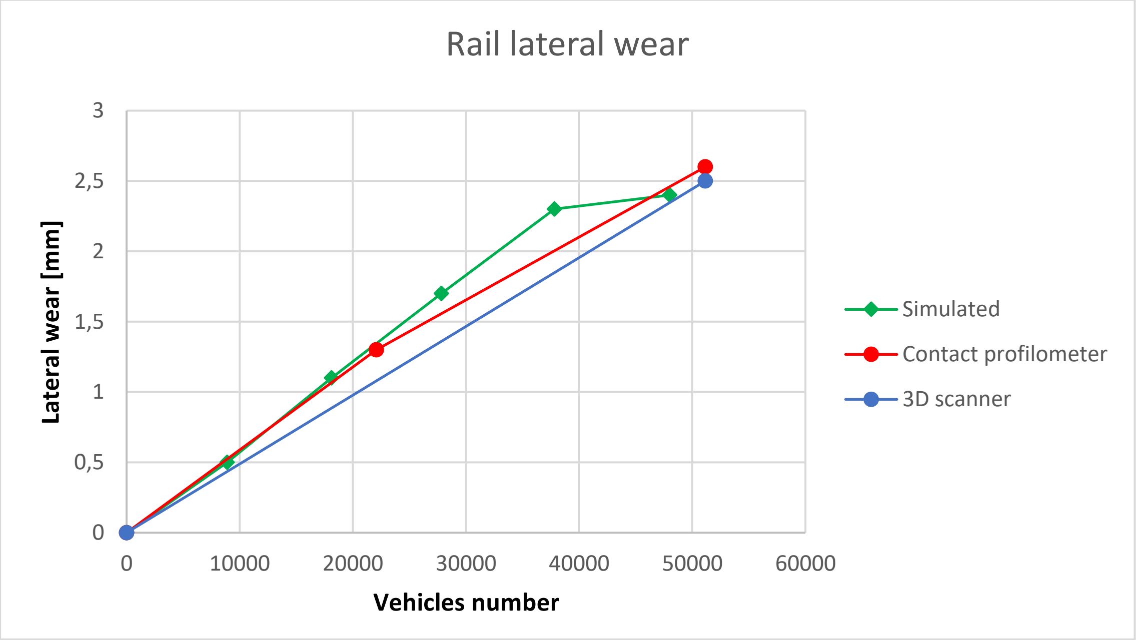

Fig. 89 Comparison between experimental and simulated lateral wear

Table 13 Experimental lateral wear as function of the vehicles number

Vehicles n°		**0**	**22 088**	**51 145**
Lateral wear [mm]	Contact profilometer	0	1.3	2.6
	3D scanner	0	-	2.5

Table 14 Simulated lateral wear as function of the vehicles number

Vehicles n°	**0**	**8 880**	**18 132**	**27 834**	**37 829**	**47 995**
Lateral wear [mm]	0	0.5	1.1	1.7	2.3	2.4

In both cases (profile shape and lateral wear), the results obtained from the comparison are satisfactory, highlighting the good accuracy of the model.

It has to be pointed out how the 3D laser scanner allowed a more accurate study of the rail profile evolution than the contact profilometer, providing a clearer and more complete picture of the wear distribution over the whole rail surface.

5.3. RCF

The RCF model provides as outputs of each discrete step of the iterative process the crack depth distribution along the wheel and rail profile. More in details, for each point of the profile in lateral direction, the model is able to predict if the crack initiates and its evolution in terms of length and depth. In the following, the main outputs of the tool in terms of RCF damage evolution will be presented. Despite the lack of measured data about RCF of the reference scenario, since the RCF law has been calibrated against experimental laboratory tests performed under strictly controlled conditions it is reasonable to be confident about the model trustworthiness.

5.3.1. Wheel

The crack depth of the leading axle of CM1 bogie shown in Fig. 90, is obtained after the 5 wheel steps of the first general rail step of the iterative process. The cumulative RCF crack depth on the wheel refers to a running distance equal to 81 088 km (the distance reached after 5 wheel steps of the process). The maximum crack depth of about 0.73 mm is localized both on the tread and the flange zone of the wheel. In fact, these zones, considering the same number of cycles, are the most severely stressed during the vehicle motion. Moreover, the tread area is less subjected to wear which may remove cracks, increasing the probability of their growth. With reference to Fig. 90, the last blue profile is the total amount of crack depth calculated adding up the crack depths obtained at each discrete step of the procedure. The crack length and depth for each discrete step are evaluated considering the effect of wear on cracks: if the wear rate is high, the crack may be also worn off. To include the effect of wear, the difference between crack and wear depth is calculated. The cracks are considered worn off where this difference assumes negative values (see equation (3-20).

In Fig. 90 the maximum crack depth on the wheel at the first rail step is plotted as a function of the distance travelled by the vehicle. Despite the lack of experimental data about the RCF damage on the considered line, the results numerically obtained are comparable with those found in literature [14].

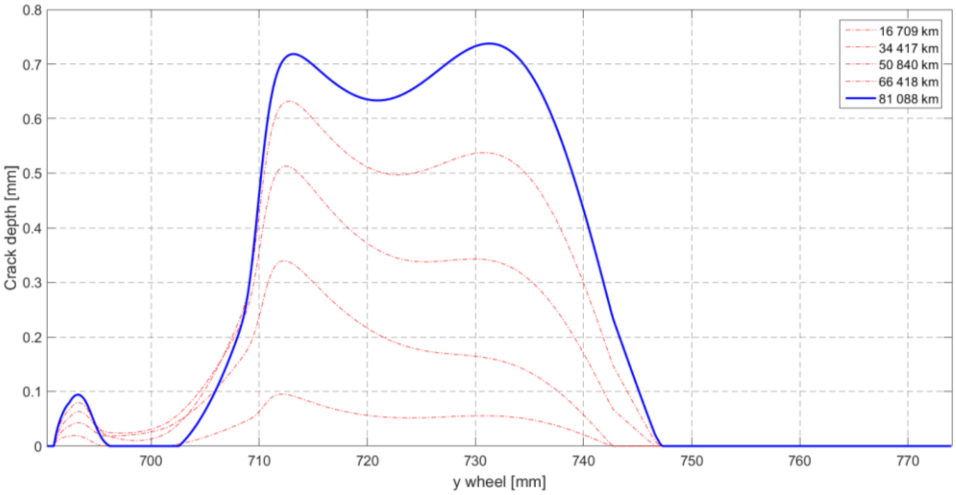

Fig. 90 Simulated RCF crack depth evolution on wheel of the leading wheelset, left wheel

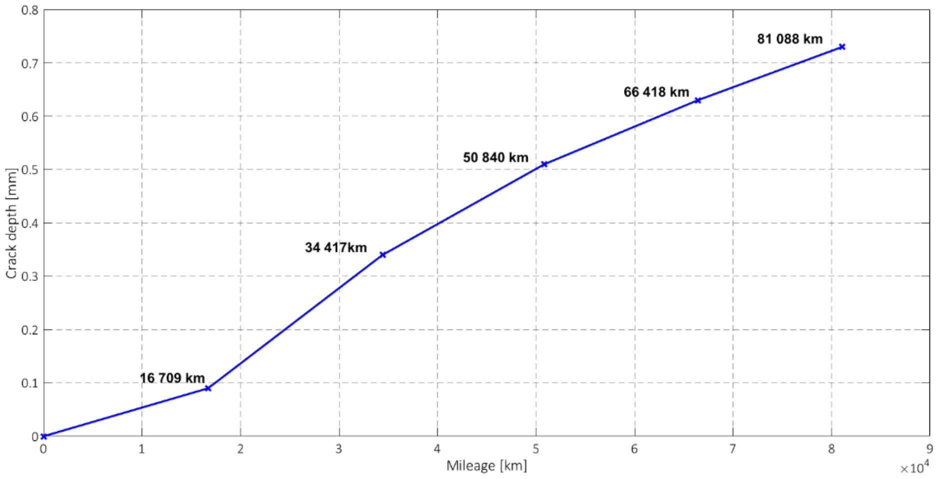

Fig. 91 Simulated crack depth against the mileage

5.3.2. Rail

As in the wear evolution assessment, the crack growth has been evaluated using the statistical approach described in 5.2.2. In Fig. 92, Fig. 93, Fig. 94 the crack depth evolution related to a large, medium and narrow radius curves of the Florence tramway line after 5 rail discrete steps of the wear loop corresponding at a total tonnage of 5.12 Mt, is shown. The maximum RCF damage is located on the rail flank zone due to a greater concentration of the stress in that area, especially in curve, in consequence of wheel-rail contact. In fact, the outer wheel strikes the side of the rail generating forces with an intensity even greater as the curve radius decreases.

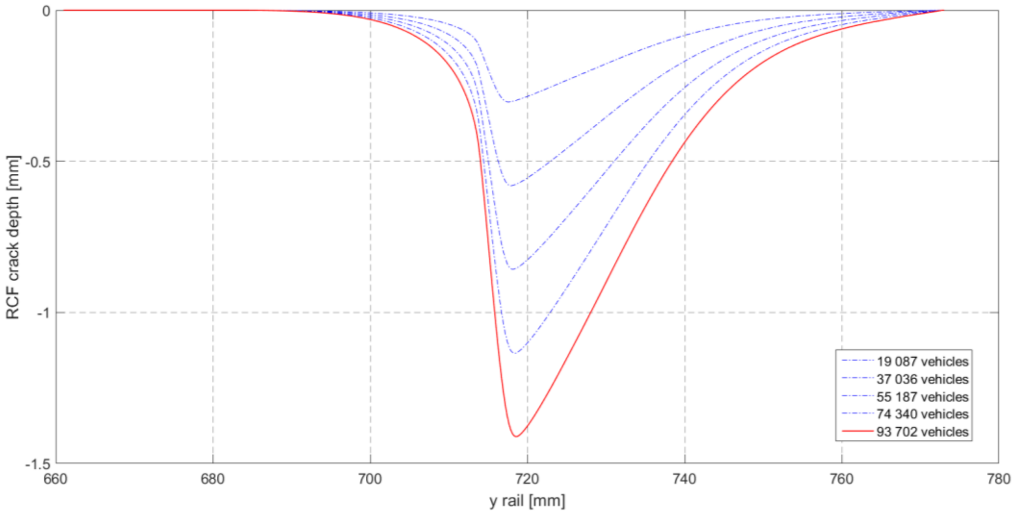

Fig. 92 Crack depth growth - Curve R=38 m

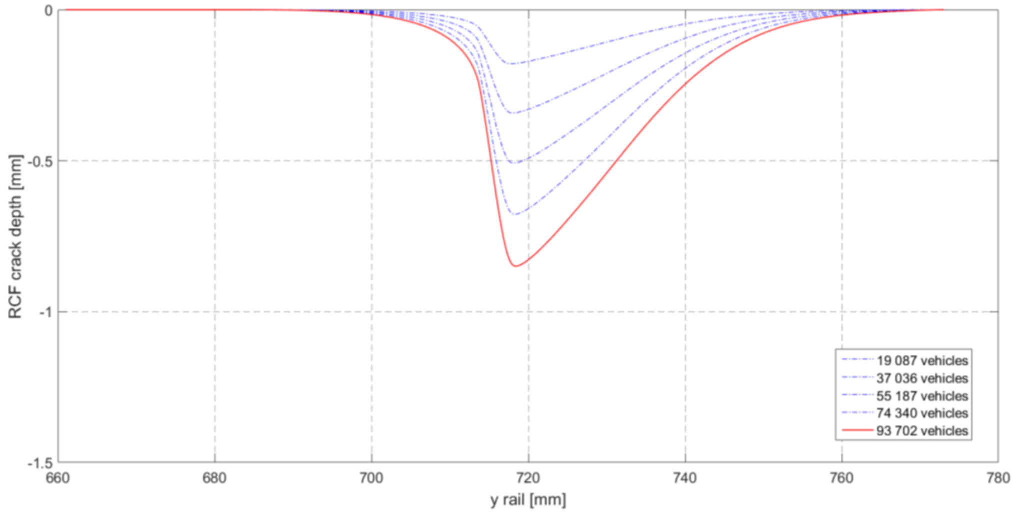

Fig. 93 Crack depth growth - Curve R=149 m

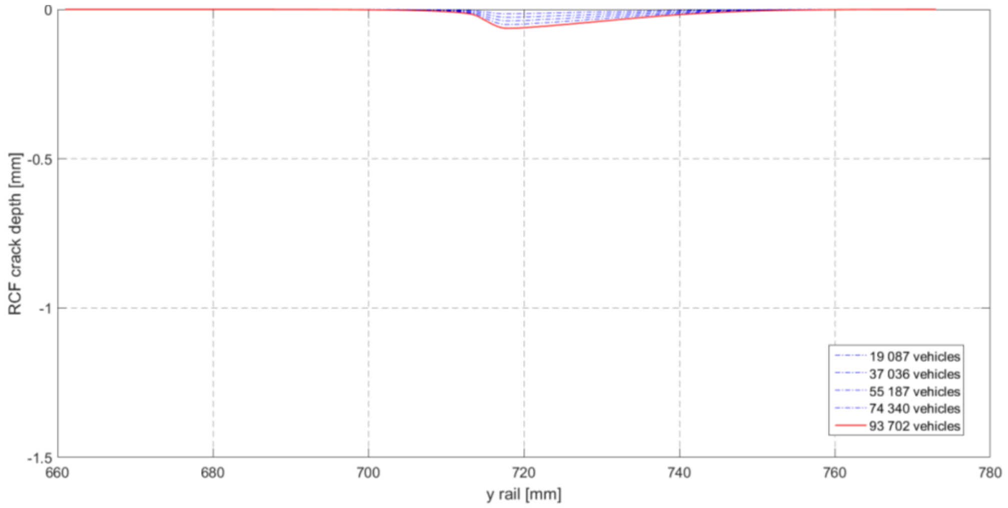

Fig. 94 Crack depth growth - Curve R=1084 m

In Fig. 95 the crack dimension progress of the three curves taken as an example, is plotted as a function of the number of vehicle running on the line to better appreciate the increase of RCF damage with the curve radius.

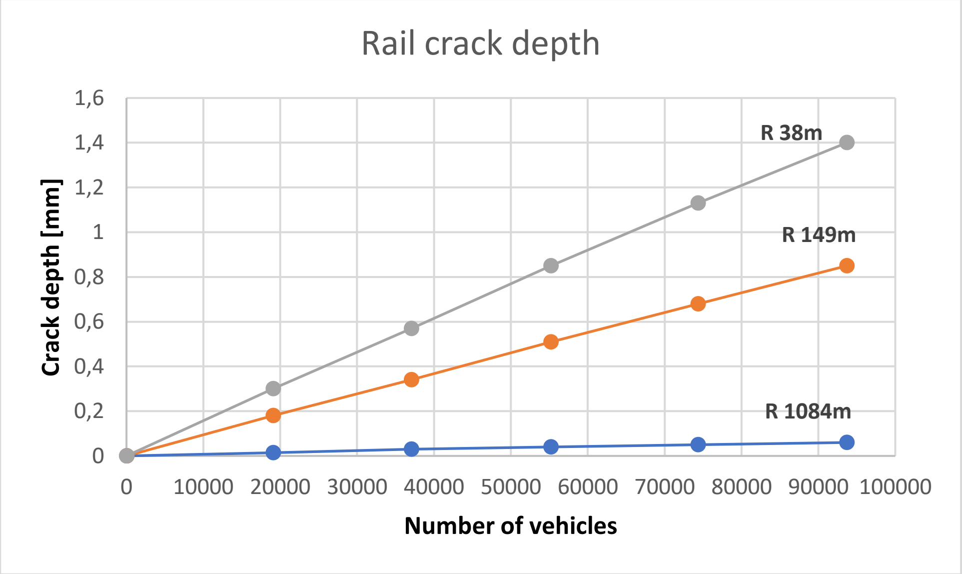

Fig. 95 Crack depth growth as a function of the number of vehicles

5.4. Sensitivity analysis

A sensitivity analysis has been performed to investigate the influence that a change in the vehicle characteristics have on wheel damage. Different cases have been analysed and their results (relative to the leading wheelset) have been compared with a reference calculation to evaluate the effect on wear and RCF damage of different solutions. The reference calculation has been performed on the same set of curves obtained from a statistical analysis of the Florence tramway network but starting from new wheel and rail profiles. In this way, having the system in its nominal condition, a more general impact assessment of the changes introduced can be obtained. It has been analysed the effect of different vehicle architecture and maintenance strategy by introducing a different wheel profile and simulating the presence of a flange lubrication system. In Table 15 are summarized the tests carried out varying wheel profile (Test 1) and the friction coefficient (Test 2). All the following comparisons have been performed considering the results of the leading axle.

Table 15 Sensitivity analysis

	Reference case	**Test 1**	**Test 2**
Wheel profile	New UNI3332	105 mm wide wheel	UNI3332
Rail profile	New 60R2	New 60R2	New 60R2
Friction coefficient	0.36	0.36	0.36 on tread, 0.15 on flange

In Test 1 the vehicle has been equipped with a different wheel profile of 105 mm wide especially developed for the Tramway of Florence and mounted on the new vehicles operating on the line. A comparison in terms of profile evolution between the classical UNI3332 and the new 105 mm wide wheel profiles obtained after five discrete steps of the iterative process is presented in Fig. 96. It is clear the positive effects of the new wheel profile on wear. This effect can be quantified comparing the distances travelled to reach a certain rate of wear between the reference calculation and the Test 1. Since the two profiles have different values of the reference parameters in unworn condition, the comparison in terms of travelled mileage by the vehicle, has been performed considering the distance travelled to reach the same quote variation ΔLbe. Flange thickness has been considered as reference parameters because the small radius curves that characterized the tramway line lead to a more pronounced wear rate on wheel flange. The comparison is reported in Table 16 and highlights the significant improvement in the distance travelled by the vehicle thanks to the introduction of the new wheel profile.

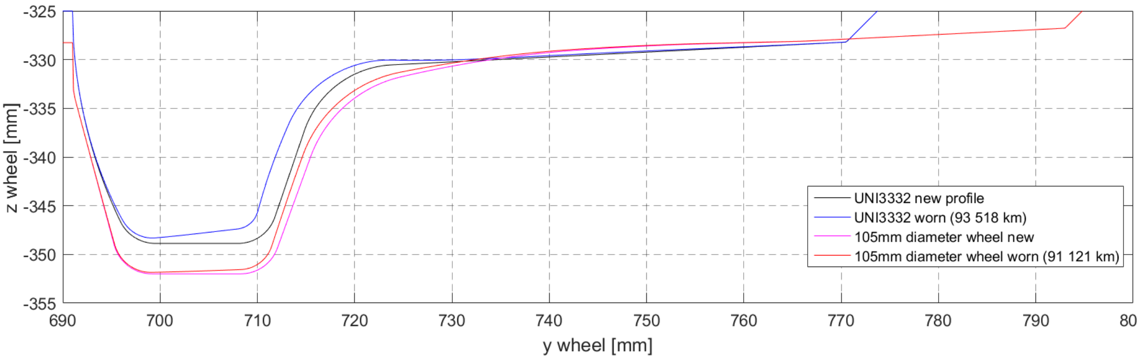

Fig. 96 Test 1 - Effect on wear of a 105 mm wide wheel profile

Table 16 Test 1 - Difference in the mileage travelled

Value of reference ΔLbe [mm]	1.95
Test case	**Space travelled**
Reference case	91 248
105 mm wheel profile	194 264
Space travelled variation [%]	**+ 113**

In Fig. 97 the RCF crack depth evolution in presented and in Table 17 the difference in terms of crack depth is shown. To compare the RCF crack depth the same mileage equal to the reference case total space travelled (93 518 km) has been considered. Also in this case, it can be noticed how the introduction of the new wheel profile leads to a significant decrease in the crack depth.

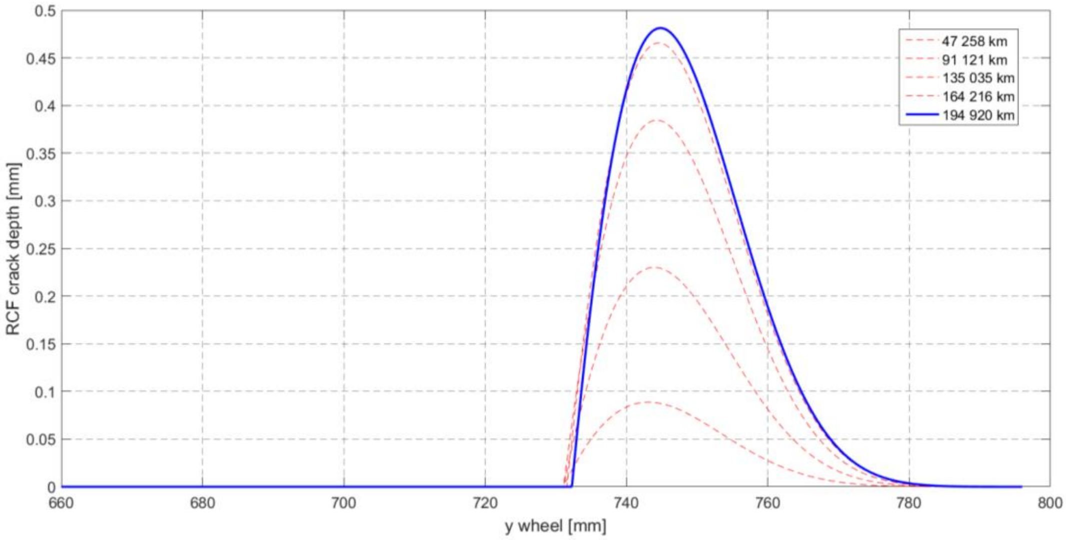

Fig. 97 Test 1 – RCF damage on 105 mm wide wheel profile

Table 17 Test 1 - Difference in crack depth

Crack depth	Value [mm]	Crack depth variation [%]
Reference case	0.75	- 68
105 mm wide wheel profile	0.24	

In Test 2 to analyse the effect of a lubrication system, a variable friction coefficient along wheel profile has been adopted: lower in the flange area (μ=0.15) and higher on the wheel tread (μ=0.36). The vehicle model is the same used in baseline calculation except for the friction coefficient that is now variable along wheel profile.

In Fig. 98 the wheel profile shape evolution due to wear obtained after five discrete steps of the iterative process is shown. Here, the wheel profile of the reference case and the lubricated one obtained after about the same mileage travelled have been compared. The good effect on the wheel flange wear evolution of the lubrication system is evident. In fact, the lower friction coefficient lead to a decrease in the wear rate on the flange respect to the reference case. While, on the wheel tread, it can be noticed a similar wear distribution between the two considered cases since the same value of friction coefficient on the tread (no friction modifier has been applied). In Table 18 an estimation of the mileage covered by the vehicle to reach the same values of the wear reference parameters (Lbe) are shown: it can be seen a benefit in terms of distance travelled with the introduction of the friction modifier (for the same flange thickness reached, the distance increase of 75% respect to the reference case).

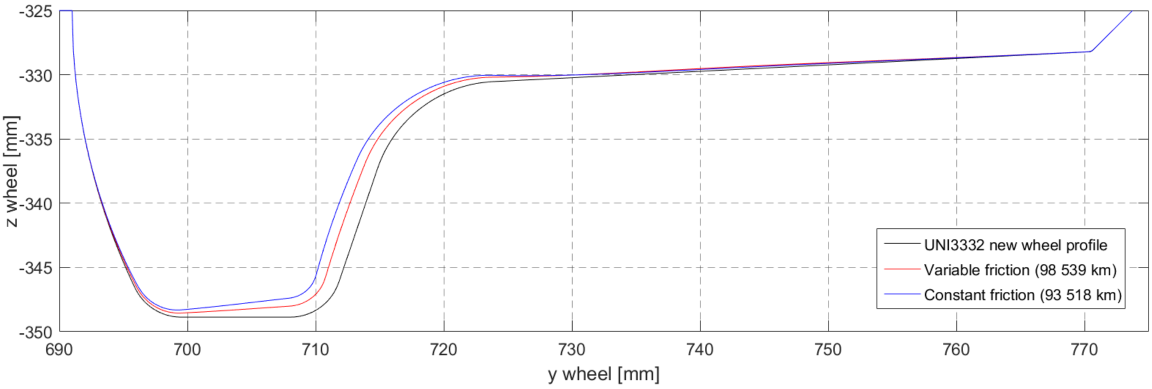

Fig. 98 Test 2 - Effect on wear of a variable friction coefficient

In Fig. 99 the RCF crack depth evolution in presented while in Table 19 the percentage difference in terms of crack depth compared to the reference case is shown. The same travelled mileage (93 518 km reached in the reference calculation) is considered to compare the RCF crack depth. In the case with the wheel flange lubricated the crack depth increase of 2.6% due to the less wear rate that directly impact on crack growth.

Table 18 Test 2 - Difference in the mileage travelled

Value of reference Lbe [mm]	20.95
Test case	**Space travelled**
Reference case	91 248
105 mm wheel profile	159 647
Space travelled variation [%]	**+ 75**

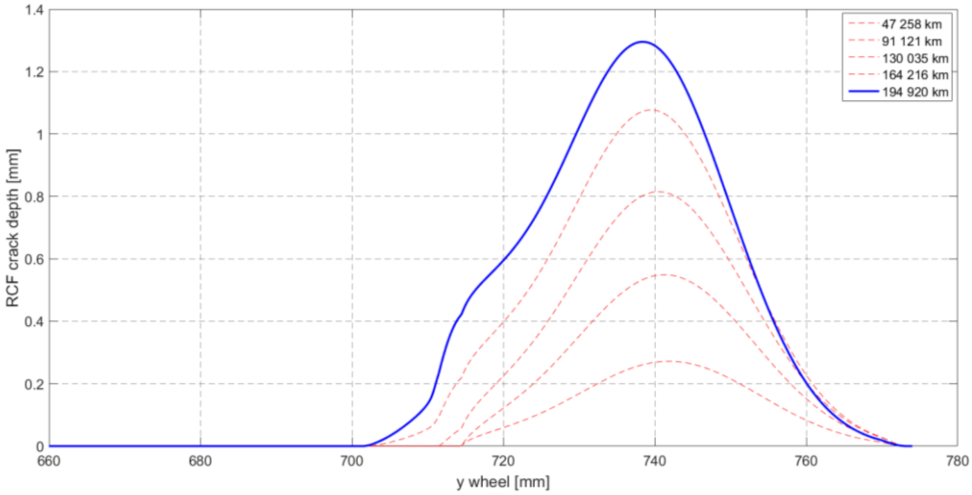

Fig. 99 Test 2 – RCF damage with variable friction coefficient

Table 19 Test 2 - Difference in crack depth

Crack depth	Value [mm]	Crack depth variation [%]
Reference case	0.75	+ 3
Variable friction	0.77	

In this paragraph the proposed tool has been applied to a tramway scenario and the results in terms of wear and RCF assessment has been discussed and analysed. The results of the wear - RCF model are encouraging both in terms of wear - RCF evaluation and in terms of numerical efficiency. The model reproduces quite good the evolution of all the profile characteristic dimensions, describing in satisfying way the wear progress both on the wheel and on the rail.

6. Test case: subway application

The proposed damage tool has been also tested considering a subway application. In the following paragraphs a detailed description of simulated scenario illustrating the track layout, the vehicle main characteristics and its mission profile, essential inputs for the damage tool, will be given. Also in this test case, the aim was to evaluate the wear evolution and RCF crack growth to compare the obtained results against experimental data. More in details, for the wheel, the model validation will be carried out comparing both the measured reference parameters and the measured wheel profiles with the simulated ones. While, for the rail, the attention was focused on two reference curves affected by a serious damage comparing the experimental profile shape evolution with the simulated one. Moreover, the corrugation growth has been assessed on one of these curves.

6.1. Simulated Scenario

The benchmark vehicle chosen for this work is a driverless subway vehicle, designed by Hitachi Rail on MLA platform (light automatic metro). The vehicle is a fixed-length trains composed of four carbodies and five bogies (four motorized and one - the third - trailer – see Fig. 100). The intermediate ones are Jacobs type bogies. The bogie frames are made up of two articulated semi-frames connected each other by a spherical joint to ease the vehicle entry in sharp curves and on track twists (see Fig. 101). The multibody model consists of several rigid bodies connected each other by means of appropriate elastic and damping elements. Particularly the vehicle is equipped with two suspension stages. Both the suspensions stages have been modelled using viscoelastic force elements taking into account all the mechanical non linearities of the system (bumpstops clearance, dampers and rod behaviour). More in details, the primary suspension is a bush comprised of two concentric metal sleeves with rubber vulcanised between them (commercial name Sutuco) while the second suspension stage includes air springs and a vertical dumper.
To sum up, according to the real vehicle characteristics (see Fig. 100), the multibody model built in Simpack environment, consists of:

- Five coaches

- Five bogies, four motorized and one trailer (the central one)
- Eight motors
- Eight gearboxes
- Ten wheelsets.

Table 20 Principal vehicle and line characteristics

Total vehicle length	49 000 mm
Max width	2 650 mm
Bogie centre distance	10 850 – 11 000 – 11 000 – 10 850 mm
Motor and trailer bogie wheelbase	2000 mm
Wheel diameter	711 mm
Wheel profile	ORE S1002
Track gauge	1 435 mm
Rail profile	UIC 50
Rail cant	1/20

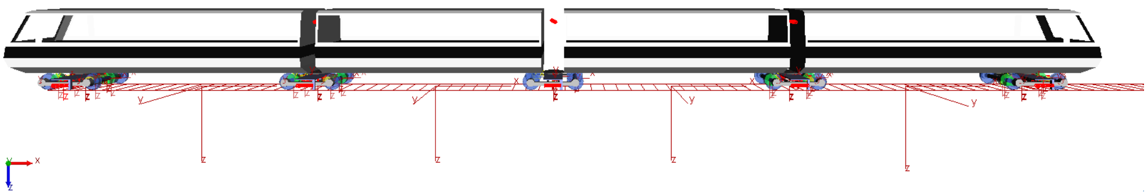

Fig. 100 Multibody model of the benchmark vehicle

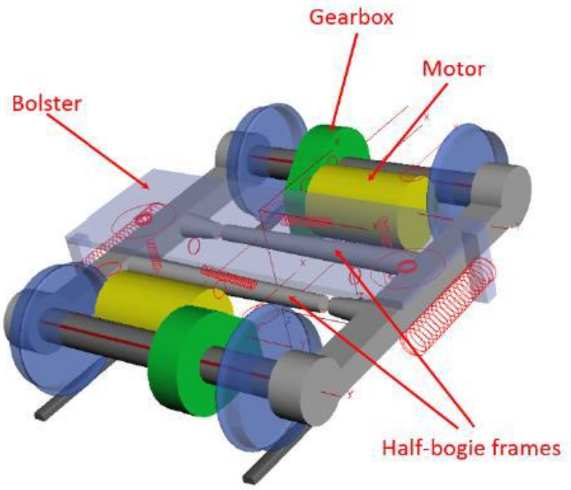

Fig. 101 Multibody model of the bogie

The vehicle is equipped with an ORE S1002 wheel profile: the wheel profiles implemented within the model, are measured and represent the real evolution due to wear of the wheel mounted on the vehicle. The vehicle operates along a line of approximately 12.8 km length with 19 stations distributed along its route. The line presents some curves of small radius (R<150 m), which impacts on the magnitude of the forces acting on the wheelset and on wheel and rail damage.

To study the wheel damage evolution, during the simulations the multibody model runs on the entire track. In order to reduce the computational time, the whole track has been splitted into four sections of about 6 km to be used for four different dynamic simulations (to simulate a roundtrip) carried out in parallel. Considering the real operating conditions, two vehicle configurations have been developed depending on whether the vehicle runs on the even or odd track. In fact, during the service the vehicles are not rotated in the passage between the two tracks. Then, the leading coach in one case will be the A and in the other the coach B (see Fig. 102): in particular when the vehicle travels the odd track the coach A is at the head of the train, while, in the other case, the coach B is in the leading position. The maximum speed is 80 km/h while the average service speed is set at 29 km/h. The speed profiles relating to the four sections in which the entire route has been divided are shown in Fig. 103. Since the maintenance plan includes the acquisition of rail profile, to improve the modelling approach accuracy, the real measured rail profiles have been implemented within the multibody model of the track. Analysing the information about maintenance actions on the track, it has been possible identify those section of the track subjected to grinding or rail substitution near the time period considered for the simulation. The rail profile in these sections has been considered unworn (new profile) while, in the other sections, the profile obtained from the measurements (and then worn) has been added to the track model. Therefore, the rail profiles change as a function of longitudinal coordinate of the track, both for the right and for the left rail (see Fig. 104 as example).

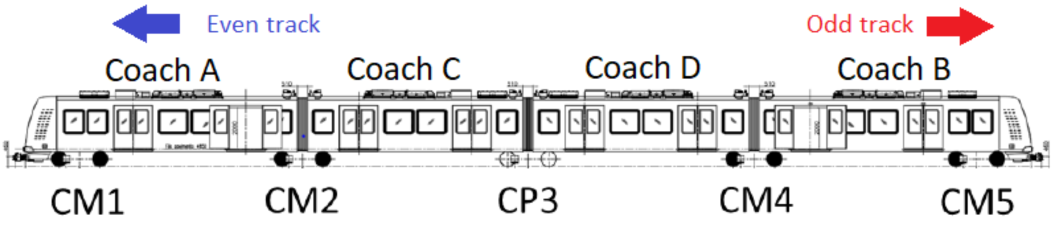

Fig. 102 Even and odd track directions

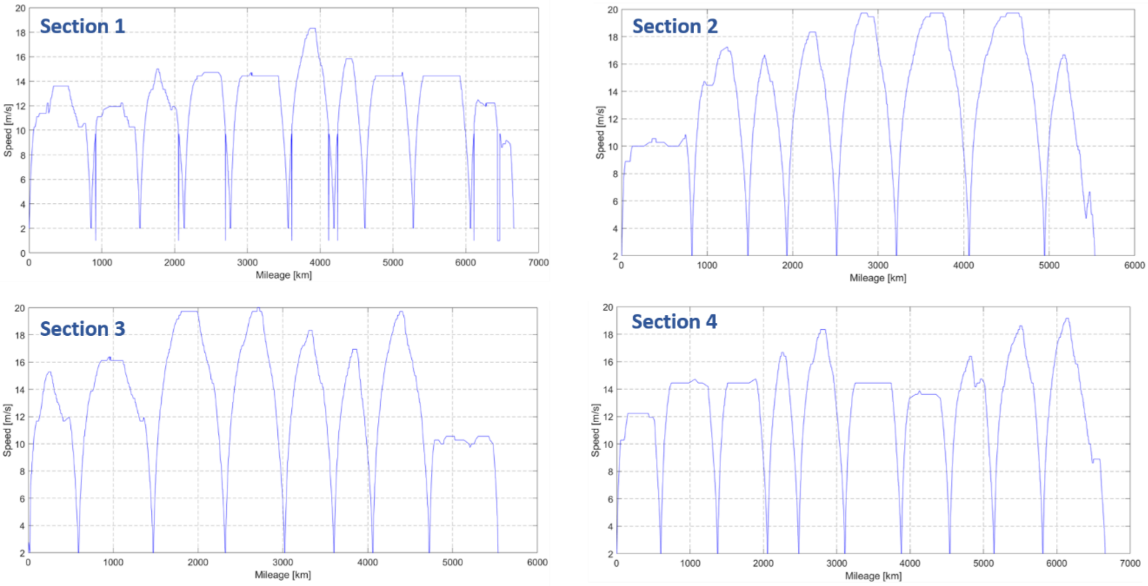

Fig. 103 Speed profile of the four sections

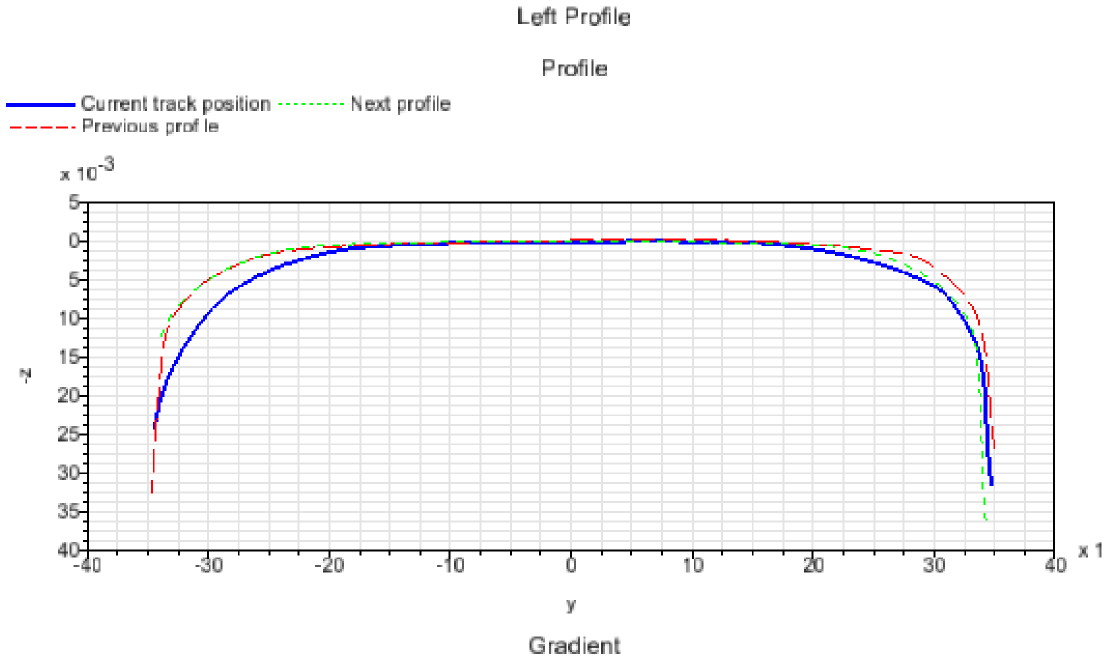

Fig. 104 Variable rail profiles

For the rail, the damage in terms of profile shape evolution has been assessed on two reference curve which have presented severe problems because of wear. Their main characteristics and their position along the line are reported in Table 21 and Fig. 105.

Table 21 Reference curve characteristics

Curve	Radius	Lenght	Speed
C17	200 m	320.48 m	60 km/h
C23	150 m	233.29 m	44 km/h

Fig. 105 Position along the line of the reference curves

6.2. Wear

As in the tramway case, to assess the model reliability a validation against measurements acquired on field has been carried out. For the wheel, the wear evolution in terms of reference quotas and change in profile shape, has been taken into account. For the rail, the study was mainly focused on the variation of profile shape of the two reference curves comparing the simulated and measured profiles. In the following paragraphs the validation of the wear part of the tool will be discussed, analysing separately the evolution of the wheel and the rail.

6.2.1. Wheel

The reference parameters FH (flange height), FT (flange thickness) and QR quota as in the tramway application, are capable of estimating the wheel profile evolution due to wear without necessarily knowing the whole profile shape (see Fig. 106).

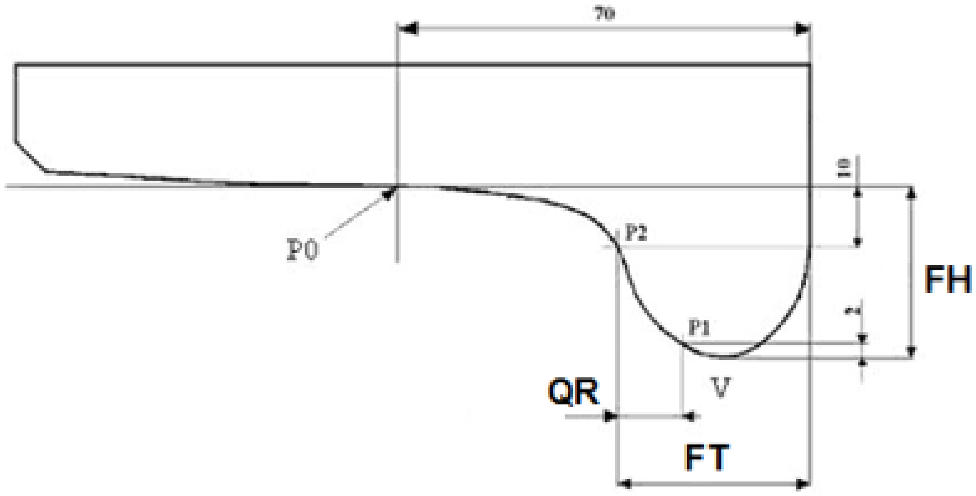

Fig. 106 Definition of the wheel wear control parameters

The wheel reference quotas are defined starting from the point that identifies the nominal rolling diameter (P0), placed at 70 mm from the inner face of the wheel:

- Flange height (FH): vertical distance between the point that defines the nominal diameter and the vertex V of the flange;
- Flange thickness (FT): distance between the point P2 (the point of the profile at a vertical distance of 10 mm from P0) and the inner face of the wheel;
- QR quote: it is the slope of the active part of the flange and is determined starting from the vertex of the flange, going up 2 mm and measuring the horizontal distance between the intersection point of this line with the wheel profile (P1) and the P2.

Table 22 Wheel reference quotas limits

	Quota	New [mm]	Limit [mm]
Measurement	**FH**	28	< 36
	FT	31	> 20
	QR		> 6.5

The wear model validation has been performed comparing both the measured reference parameters and the measured wheel profiles with those numerically evaluated. The experimental data come from five tests conducted from August 2015 to January 2016 and they consist of reference parameters progression and wheel profiles 2D shape. Measurements of these profile are carried out using the commercial instrument CALIPRI C4X based on laser light section technology (see Fig. 108 and Fig. 109). As in the previous test case, the data are related to all the wheels of the entire fleet and it was strictly necessary a data processing to extrapolate the measurements of the reference parameters evaluated in a period between two turnings, during which the profiles are not re-established. Following this strategy, it has been selected the leading motor bogie (CM1 in Fig. 102) whose related measured data goes from August 2015 to January 2016. For the model validation, the experimental reference parameters related to the leading axles of the chosen bogies have been considered. The corresponding values for the left and right wheel are given in Table 23. On the contrary of the previous test case, looking at Fig. 107, where the reference parameters are plotted against the mileage travelled by the vehicle, it can be noticed the non-symmetrical wear evolution between left and right wheel due to the operating conditions of the vehicle. In fact, during the service the vehicle is not turned and consequently a wheel runs always on the same side of the curves. For this reason, the wear evolution of the wheel of the same axle is not symmetrical and then, the wear evolution has been investigated considering the left and right side as separate. As starting wheel profiles for the simulations, real profiles measured in August 2015 have been implemented within the multibody model of the vehicle (see Fig. 110 and Fig. 111 for the right and left wheel of the wheelset 1).

Table 23 Experimental wheel wear parameters

CM1 Wheelset 1						
Mileage [km]	Left [mm]			Right [mm]		
	HB	**FT**	**QR**	**HB**	**FT**	**QR**
0	30.37	30.78	10.18	30.16	30.08	10.56
19 911	31.32	30.71	10.28	30.95	30.14	10.31
28 084	31.79	30.75	10.33	31.30	30.11	10.32
43 487	32.49	30.89	10.41	31.57	30.17	10.22
51 917	32.88	30.79	10.50	31.99	30.21	10.26

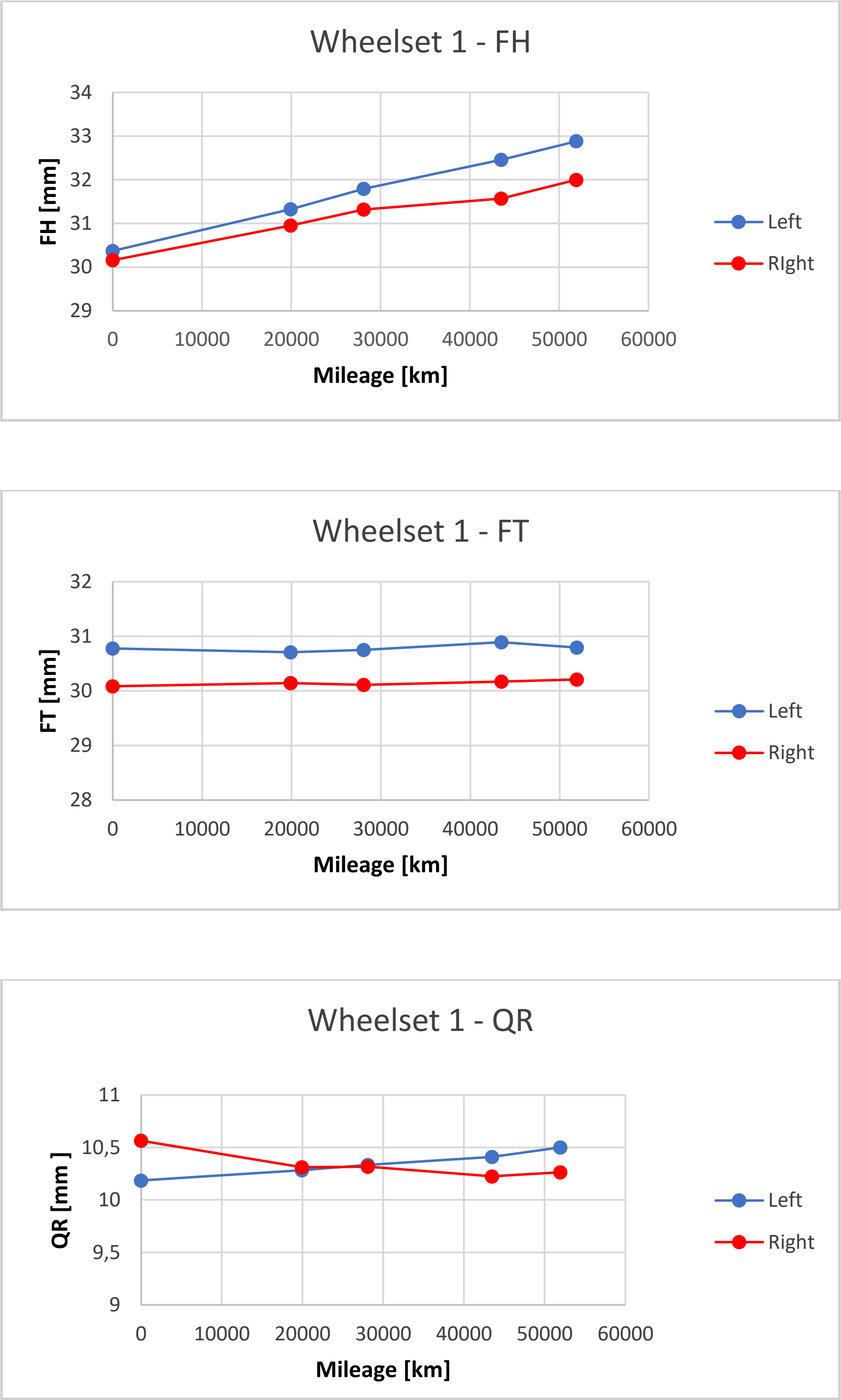

Fig. 107 Plot of experimental wheel reference parameters of the leading wheelset as a function of the mileage

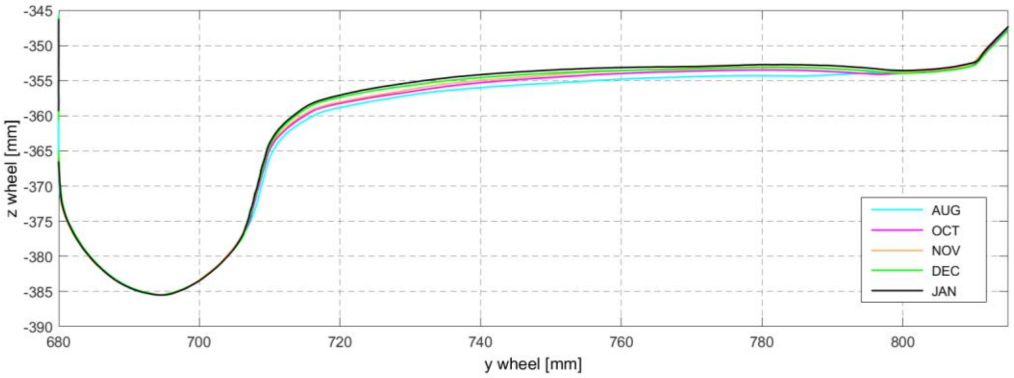

Fig. 108 Measured right wheel profile from August 2015 to January 2016 – CM1 wheelset 1

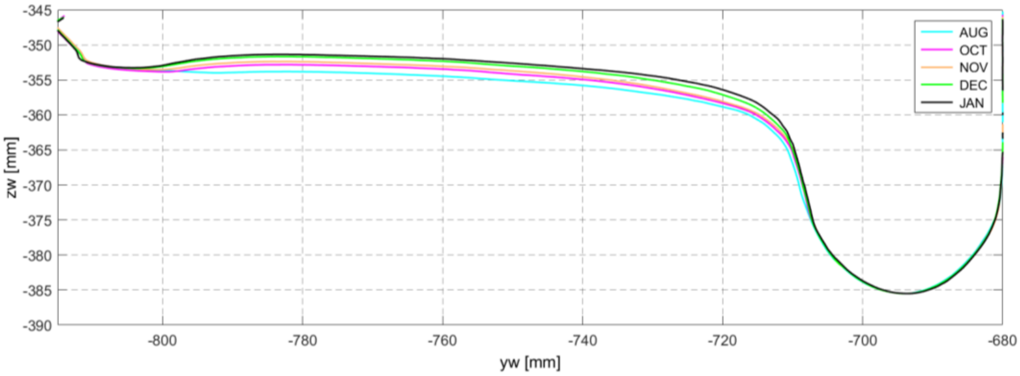

Fig. 109 Measured left wheel profile from August 2015 to January 2016 – CM1 wheelset 1

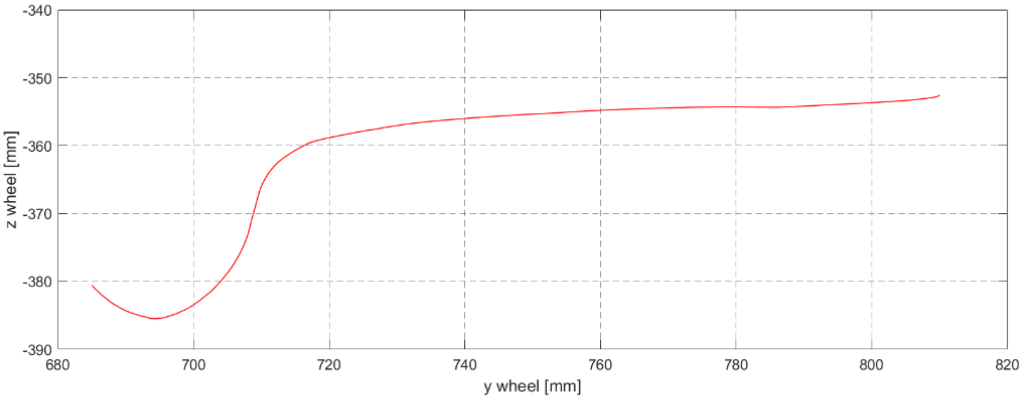

Fig. 110 Starting profile of the right wheel – CM1 wheelset 1

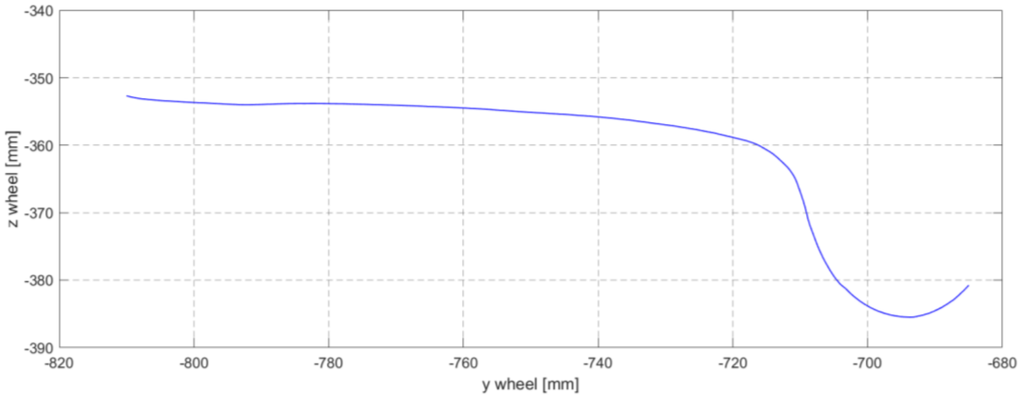

Fig. 111 Starting profile of the left wheel – CM1 wheelset 1

According to the update strategy described in 2.3.3, the threshold value (see Table 24) on the maximum thickness of material removed by wear on the wheels at each wheel discrete step has been chosen equal to 0.4 mm. Instead, for the rail a threshold value of 0.8 mm has been set. Therefore, when the removed material reaches this quantity, a discrete step finishes and the whole procedure passes to the following discrete step. In Table 24 the number of discrete steps and the adopted threshold values for the wheel and the rail profiles are summarized.

Table 24 Wear loop parameters

	N° of discrete step	**Threshold value**
Wheel	6	0.4 mm
Rail	1	0.8 mm

The evolution of the wheel wear control parameters obtained after the 6 wheel steps (from new unworn wheel up to totally worn wheel reached in 53 815 km) of the first general rail step (new unworn rail) of the iterative procedure is here compared to the experimental data.

The reference quotas evolution compared with those measured for the left wheel and for the right are represented in Fig. 112 and Fig. 113 as a function of the mileage. The FH quota progress shows how the flange height increases because the wear on the wheel tread. The comparisons had shown that the outputs of the wear model are consistent with the experimental data, both for the flange dimension (FH, FT) and for the conicity (QR); the slightly steeper development of the experimental data than the simulation can be explained with the dispersion of the experimental data and with wear mechanisms, like plastic and pitting wear, not considered in the model.

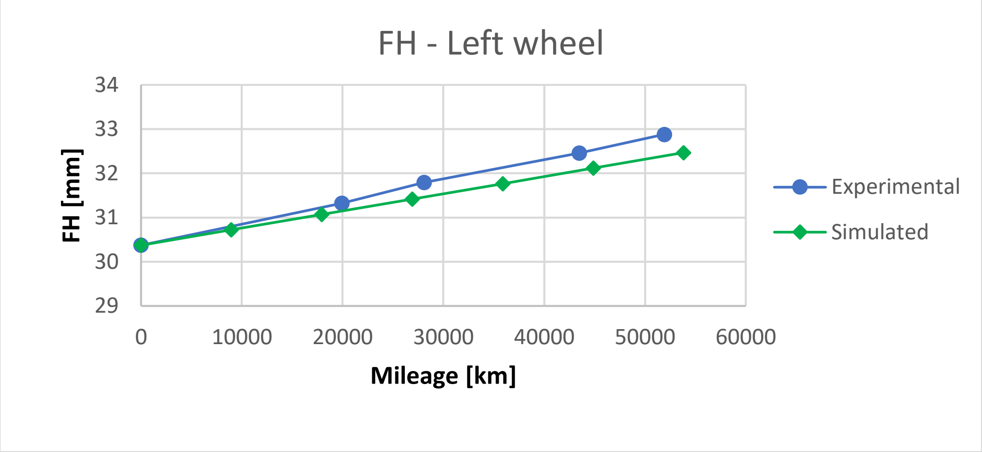

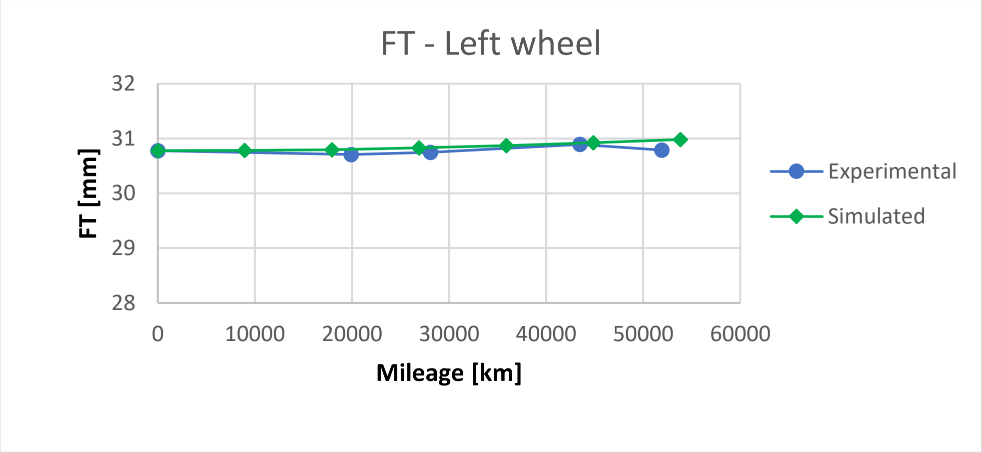

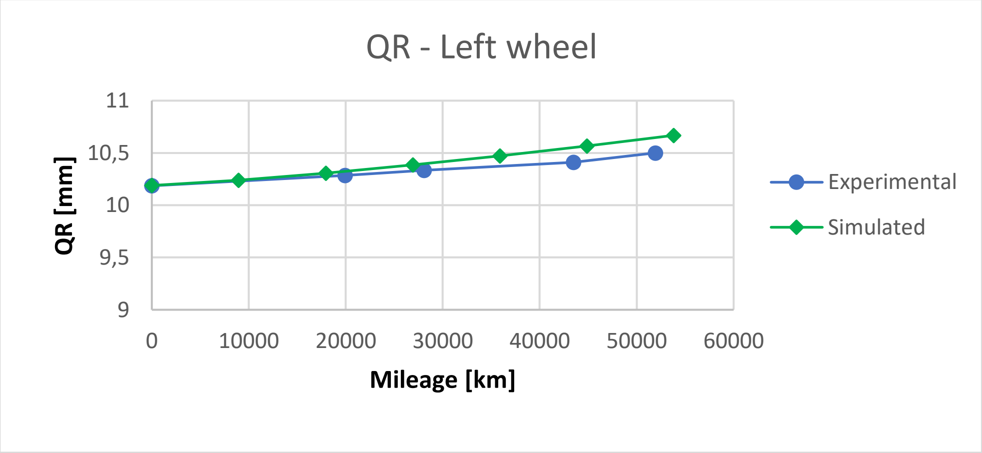

Fig. 112 Reference parameters comparison at first rail step – left wheel

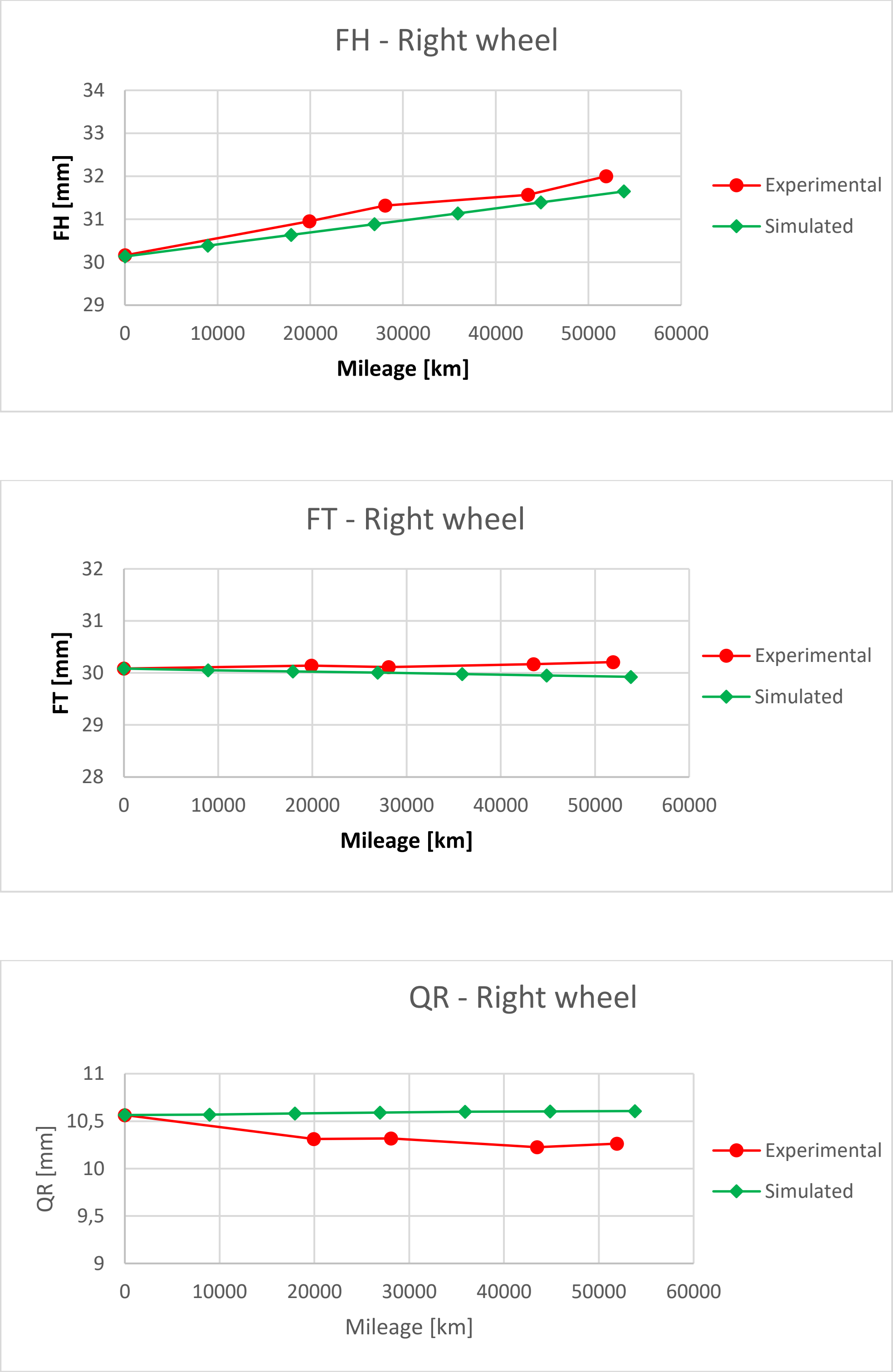

Fig. 113 Reference parameters comparison at first rail step – right wheel

The model trustworthiness has been verified also comparing the simulated wheel profile evolution against the real wear evolution. This comparison is reported in Fig. 114 and Fig. 115 both for the right and the left wheel of the wheelset 1 where the blue and red dashed lines are the profiles numerically obtained while the other coloured lines represent the experimental data, one for every measurement campaign. As supposed from the reference parameters trend, the wear is mainly localized on the wheel tread due to the several braking and traction manoeuvres typical of a subway scenario.

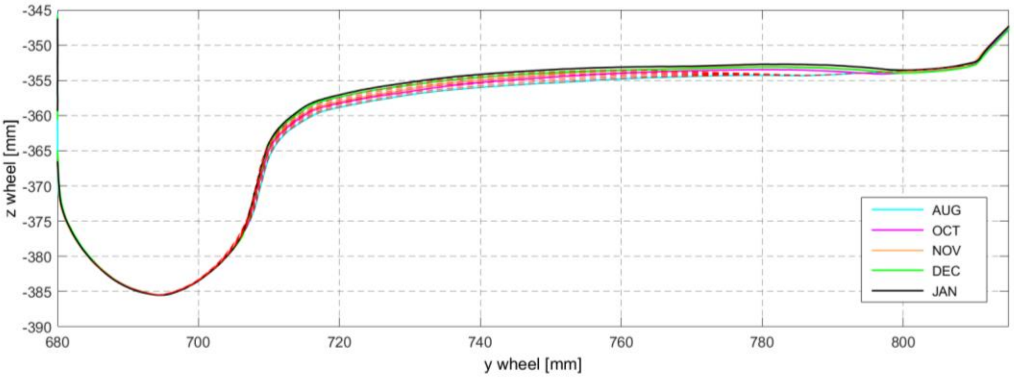

Fig. 114 Comparison between experimental and simulated wear evolution – right wheel

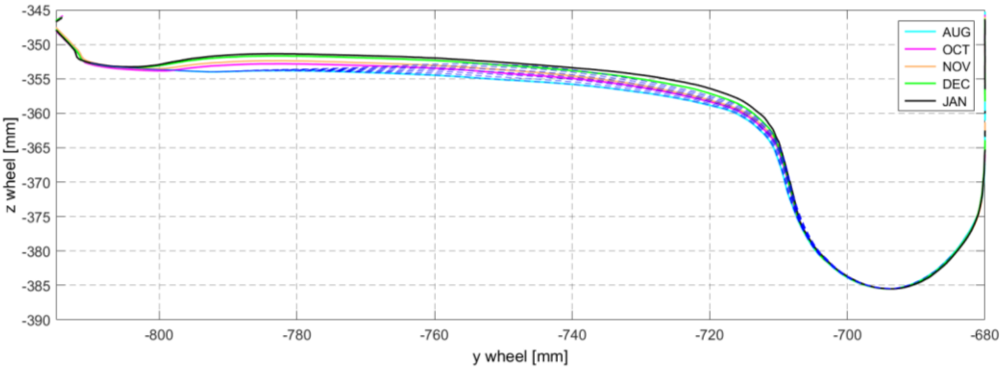

Fig. 115 Comparison between experimental and simulated wear evolution – left wheel

6.2.2. Rail

Concerning the model validation in terms of rail wear, the analysis was focused on the two reference curves (see Table 21 and Fig. 105) of the odd track which have experienced a severe damage because wear. The comparison between simulated and experimental data have been performed considering the evolution of rail shape. The acquisition of rail profiles has been carried out using the multifunctional "Plasser & Theurer EM-TRIPLEX", shown in Fig. 116. With this multifunctional vehicle it is possible to acquire several parameters, as track gauge, superelevation, level, alignment and the rail profile as a function of the travelled distance. Moreover, the main rail wear parameters have been measured by means of CALIPRI C4X. These parameters define vertical (Qt) and lateral wear (U45°) and they are determined through comparison with the standard profile (see Fig. 117). The latter parameters have been used to correct the offset error in measuring rail profile of the EM-TRIPLEX machine. Moreover, the worn rail data are affected by a certain amount of numerical noise and they had to be treated in order to smooth the profiles and their derivatives. To this end, the data were post processed and the rails profile rebuilt through several sections of cubic splines. The experimental data employed for the model validation refers to a period of about three months from August 2015 to November 2015. The profile related to the first acquisition campaign was used as starting profile implemented in the track to carry out the dynamic simulations. The wear evolution on the inner and outer rail has been evaluated separately. In Fig. 118 and Fig. 119 the three measured profiles (coloured solid lines) are plotted together with the simulated (blue dashed lines) for the benchmark curve C17 while in Fig. 120 and Fig. 121 for the C23 curve. The simulated rail profile evolution is in quite good agreement with the real development of the rail shape due to wear. The comparison between real and simulated number of vehicles running on the line are visible in Table 25. Looking at Fig. 120, it is possible to notice a disagreement near the flange zone between the simulated and measured profile. This discrepancy is mainly due to a sort of material flow on the rail head caused by the phenomenon of corrugation. In fact, this curve is affected by severe damages because of corrugation and for this reason it will be the reference curve in the following paragraphs where the corrugation phenomenon is studied.

Fig. 116 Plasser & Theurer EM-TRIPLEX

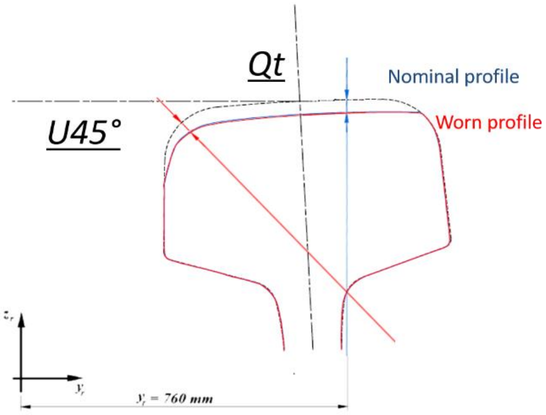

Fig. 117 Rail wear parameters

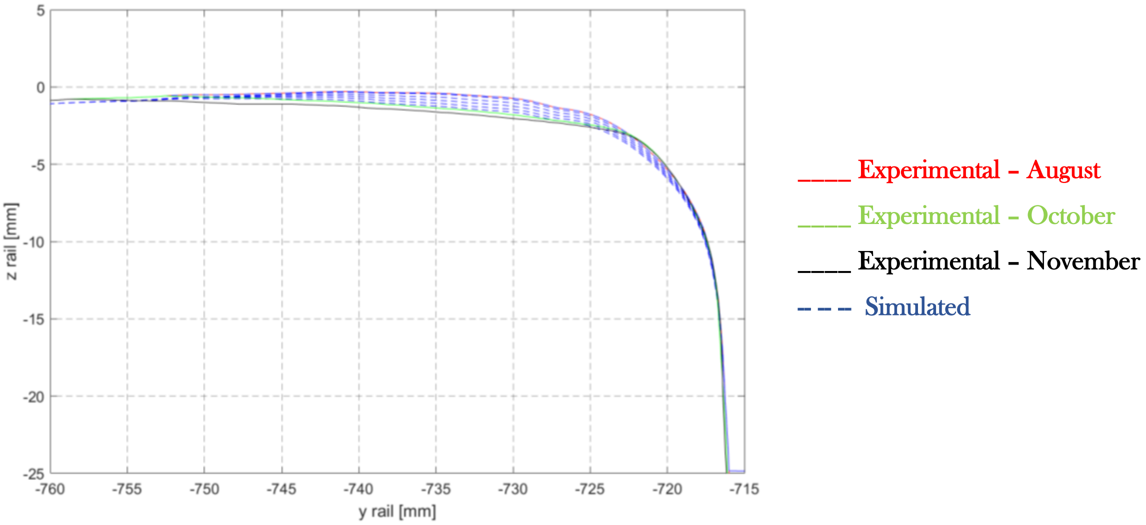

Fig. 118 Curve C17 - inner rail

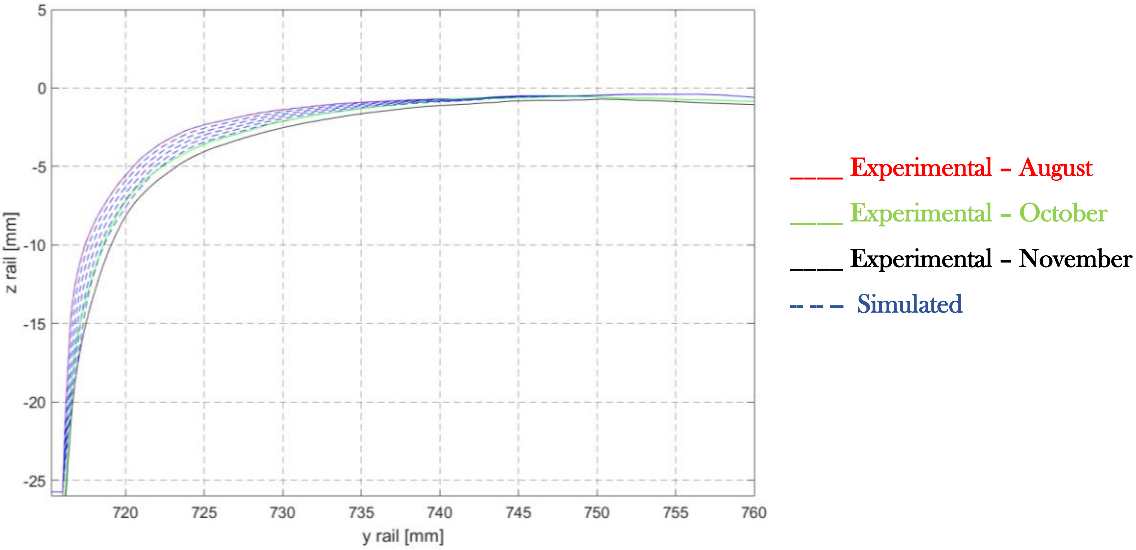

Fig. 119 Curve C17 - outer rail

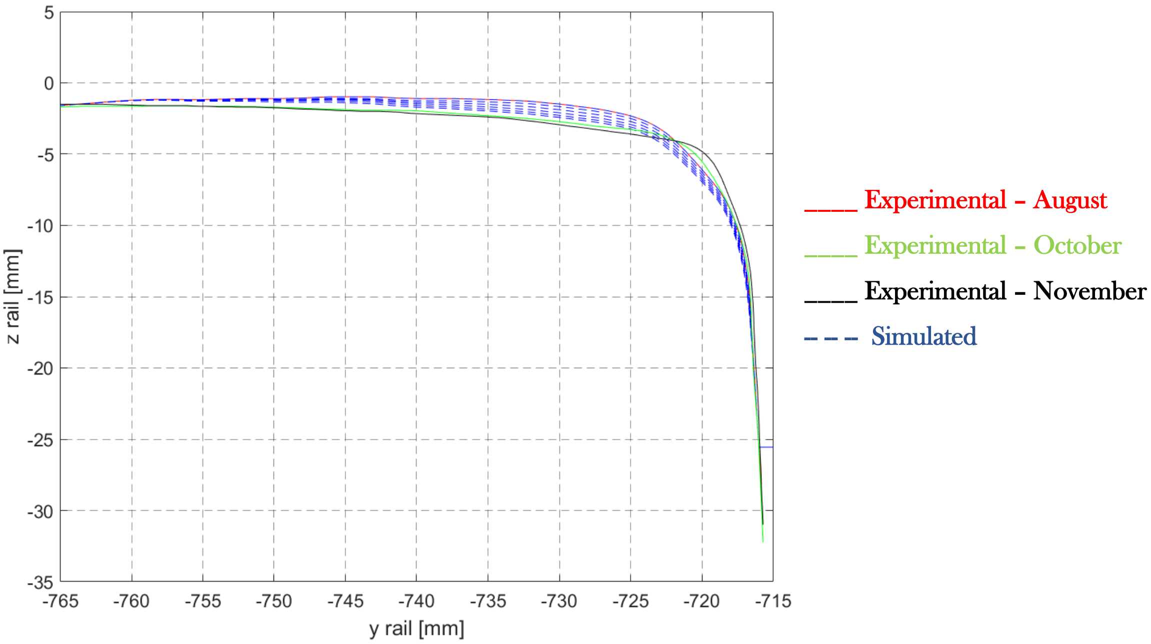

Fig. 120 Curve C23 - inner rail

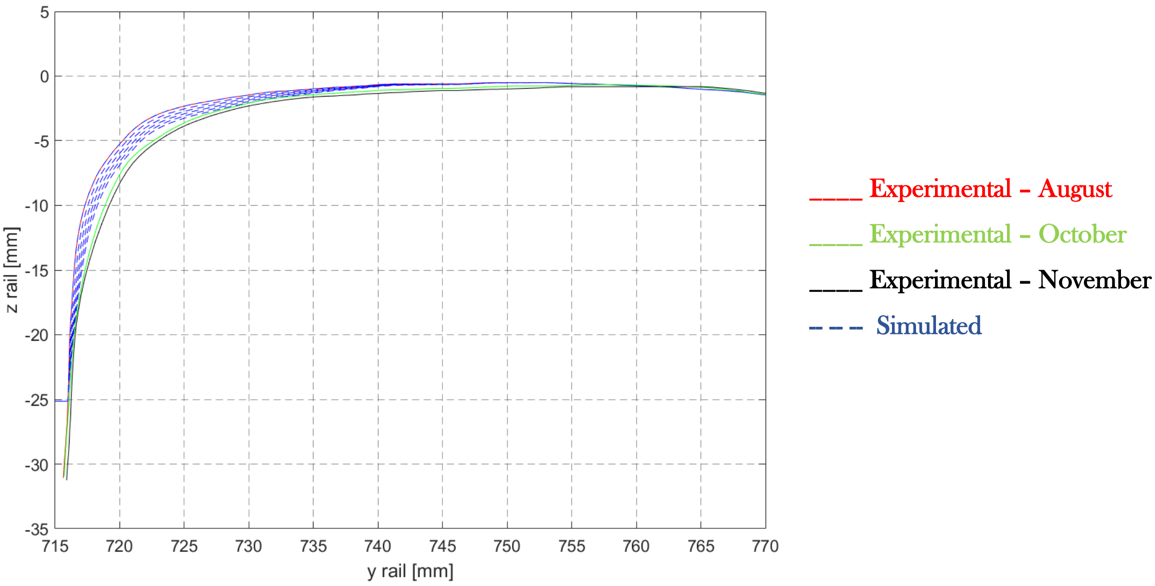

Fig. 121 Curve C23 - outer rail

Table 25 Real and simulated number of vvehicles

Real number of vehicles	Simulated number of vehicles
24 742	26 017

6.3. RCF

In the considered test case, the crack growth has been assessed on the wheel obtaining as of each discrete step of the iterative process the crack depth distribution along the wheel profile. More in details, for each point of the profile in lateral direction, the model can predict if the crack initiates and its evolution in terms of length and depth. In the following, the main outputs of the tool in terms of RCF damage evolution will be presented.

6.3.1. Wheel

The crack depth of the leading axle of CM1 bogie shown in Fig. 122, is obtained after the 6 wheel steps of the first general rail step of the iterative process according to the simulation strategy of Table 24. The cumulative RCF crack depth on the right and left wheel are visible in Fig. 123 and Fig. 124 and refers to a running distance equal to 53 815 km. Considering the right wheel, the maximum crack depth of about 0.95 mm is localized on the tread zone and around the flange, the most severely stressed during the vehicle motion because the contact forces in curves and the several traction and braking maneuvers. The same holds for the left wheel which, however, experiences less RCF damage due to the higher wear rate that reduce and sometimes remove the crack. With reference to Fig. 122, Fig. 123 and Fig. 124 the last blue profile is the total amount of crack depth calculated adding up the crack depths obtained at each discrete step of the procedure. The crack length and depth for each discrete step are evaluated considering the effect of wear on cracks: if the wear rate is high, the crack may be also worn off.

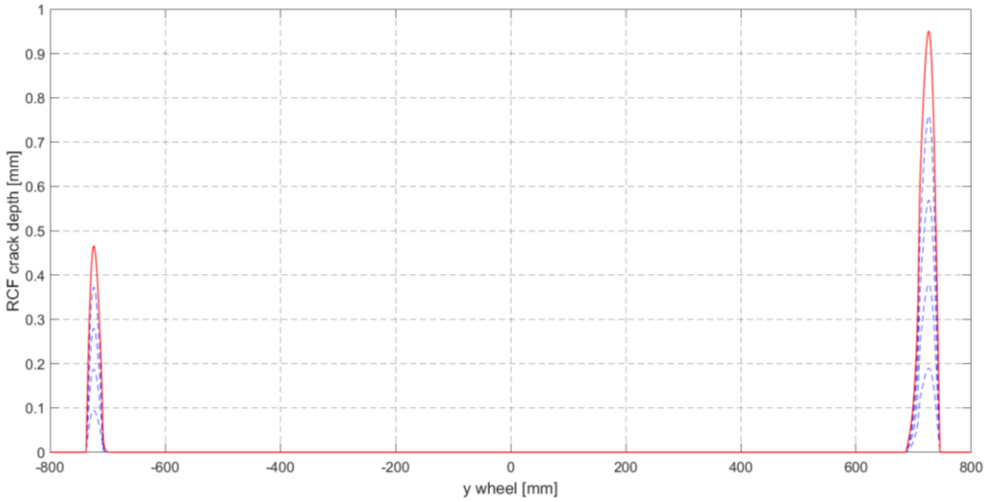

Fig. 122 RCF crack depth distribution

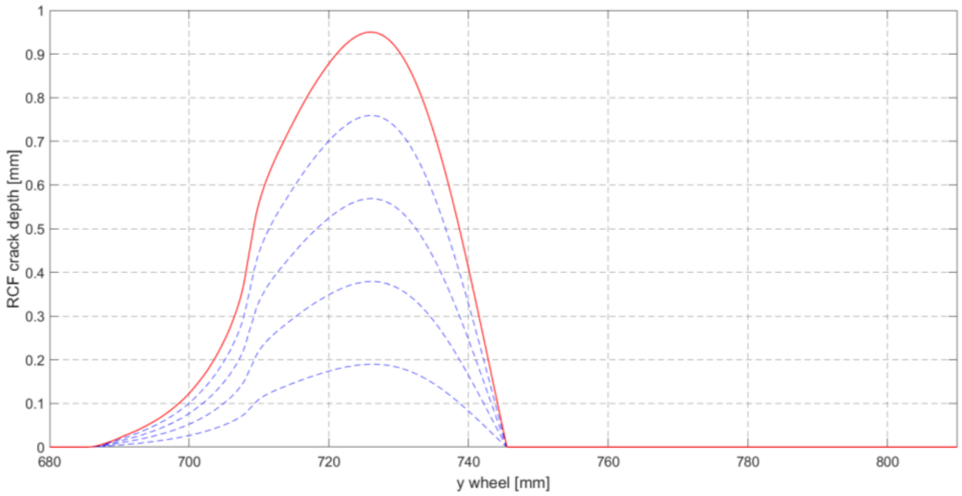

Fig. 123 RCF crack depth distribution on the right wheel

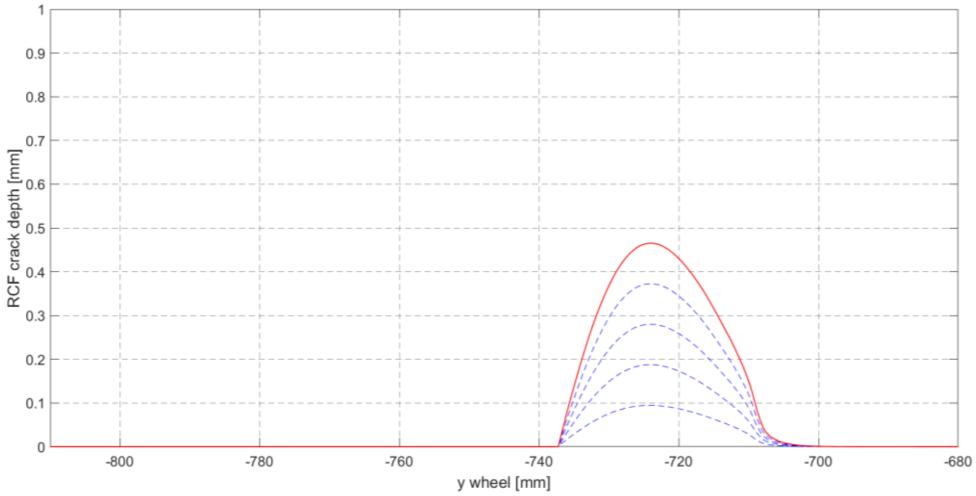

Fig. 124 RCF crack depth distribution on the left wheel

6.4. Corrugation

The last part of the tool developed during this Ph.D. project, has been preliminary validated by comparison with measurement data from a curve which has presented severe damages because of corrugation. The benchmark curve is the previous mentioned C23 whose characteristics are reported in Table 21. Corrugation is very common in the metro tracks, where small-radius curve, frequent accelerations and brakings give rise to high tangential stresses. Experimental data has been compared with the simulated ones in terms of defect wavelength and amplitude. During service, vehicle wheels change their profile, because of wear. The main novelty of this work is to consider this effect, therefore including the variability of wheel profiles in the simulation of corrugation growth. Measured wheel profiles are included in the simulation procedure which follows a discrete process allowing to reduce the number of simulation steps and thus computational times.

It is to be taken into account that as a first step the track and wheelsets are considered as rigid.

Finally, to evaluate the response of the model to some of the solutions adopted to mitigate the problem, a sensitivity analysis was carried out.

6.4.1. Measured data

As previously introduced, the validation of the model is carried out by comparison between numerical results and measurements. To reduce the number of simulation steps and thus computational times, the real variability of wheel profiles due to wear has been included in the simulation of corrugation growth. More in details, the measured wheel profiles seen in 6.2.1 has been implemented in the simulation procedure allowing a more accurate corrugation estimation and to save time since the wheel step are not performed.

The corrugation measurements are carried out using the multifunctional Plasser & Theurer EM-TRIPLEX using the laser technology. The contactless sensors mounted on the vehicle are shown in Fig. 125. This system consists of three asymmetrically displaced sensors that capture the rail height every 5 mm in the running direction. The sampling procedure and the arrangement of these sensors guarantees a correct evaluation of all wavelength in the characteristic waveband (20 mm – 1 m). Every 50 measurement steps, an FFT of the signal is carried out. The uncertainty of the instrument as regard the wavelength is ±1 mm and for the amplitude is ±0,01 mm.

Fig. 125 Sensors for corrugation measurement

Measurements in the reference curve, has been carried out between two maintenance actions, and precisely on July some days after a rail grinding, on September and on November 2015. In the Table 26, the amplitudes of the prevailing wavelength on the low rail are summarized, taken from the measurement campaign, function of the estimated number of train passages. According to the timetable of the line where the vehicles operate, the average number of trains passing on the benchmark curve is 278 per day.

Table 26 Corrugation measurements of the low rail of the reference curve

Month	Number of trains	Amplitude of corrugation (mm)
July	4726	0.03
September	16 124	0.06
November	34 124	0.25

The prevailing wavelength is 40 mm and it is constant over time, since vehicles speed (12 m/s) is constant on the reference curve confirming the fact that corrugation is a frequency-fixed phenomenon. On the high rail no prevailing wavelength has been pointed out from measurements. According to the classification of Table 3 the corrugation type in this reference curve could be classified as “rutting”, since it appears only on the low rail, the damage mechanism is wear and its characteristic frequency is 300 Hz.

In reality, corrugation starts developing because of initial irregularities present on the rail surface. In fact, if the vehicle-track system had ideal geometries, no corrugation would develop. The initial irregularity, which represents the rail roughness measured after a grinding process, was measured with the instrument Railstraight Compact and it has been added to the track model. In Fig. 126 the measured initial irregularities are shown. Since wear is evaluated in the circular section of the track, where steady-state running behaviour is reached, only a 3 m long section of it is considered for the evaluation of the removed material and corrugation growth. In fact, considering a longer section of the track, results would be similar, since the vehicle behaviour is steady along this portion of the curve. The initial rail irregularity has been implemented by translating a new EN50 E5 profile along the z-coordinate, according to initial irregularity of Fig. 126. Vectors describing the rail profile are updated every 2 mm inside the 3 m long section of the curve, where the development of corrugation was studied. Outside this section, the rail profile was described by using a new rail profile. A smooth transition between the new rail and the worn (corrugated) rail is guaranteed since the multibody software approximates the rail surfaces using Bezier curves.

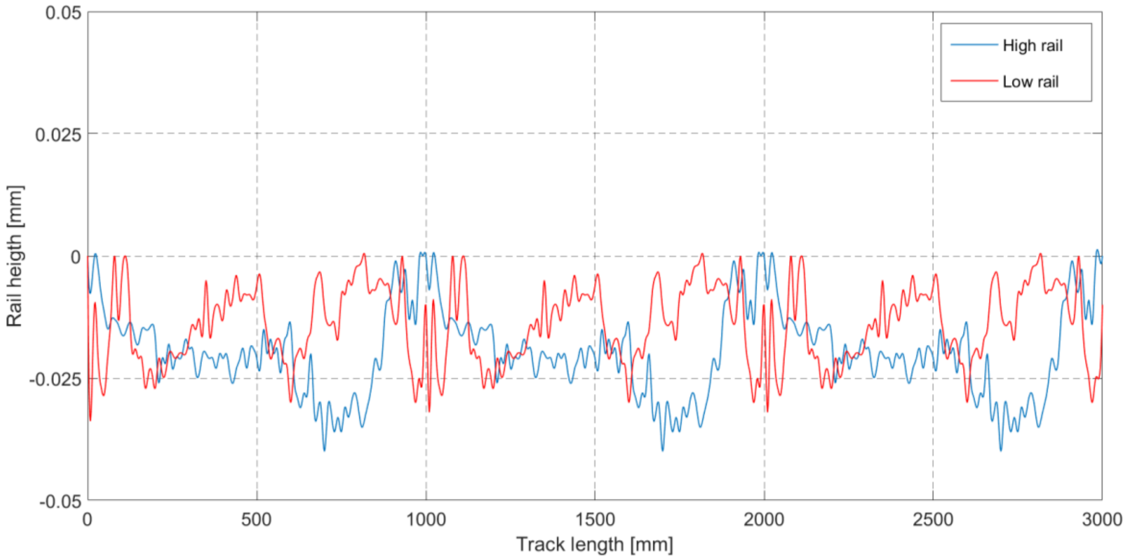

Fig. 126 Initial irregularities

6.4.2. Results

The corrugation part of the damage tool allows to have as output the 3D corrugated rail profile of the rail, the amplitude and the wavelength of the defect. In Fig. 127 the corrugated surfaces of low and high rail obtained from simulations are shown. These 100 mm long sections of the rails are obtained using a typical friction coefficient of 0.3 and a wheel and rail hardness of a typical value 270 HBW was considered. For this small section of the rail, it can be observed that low rail presents a quasi-sinusoidal corrugated surface while for the high rail, wear is uniform on the rail head and this is in accordance with measurements, where no corrugation has been pointed out. The corrugation on the low rail of a track is very common and if it arises from periodic slip of the wheel on the rail it occurs when the tangential force is close to the limit that can be sustained by friction. This may occur when the vehicle runs into a curve: tangential forces increase at the contact interface and the vertical load decrease on the inner wheel due to roll motion of the coach.

Since these surfaces represent only a small section of the track, a Fourier analysis of the 3 m long section of the track is necessary, to investigate all the waveband of interest. Fig. 128 shows the DFT of the wear depth, evaluated using the FFT algorithm, considering a longitudinal section of the low rail, half the track gauge far from the track centre. It can be observed that there is a marked waveband where corrugation develops. Results for wavelengths greater than 180 cm are omitted: both for high and low rail no prevailing wavelength can be pointed out in the part not shown of the graph. Since all vehicle and track components has initially been modelled as rigid, it is impossible to highlight a specific wavelength in these spectra. Peaks in the DFT are due to the excitation of the contact stiffness but the waveband in which the corrugation has a marked growth on the low rail (about 3-40 cm) includes the wavelength in which the corrugation grows, according to measurements.

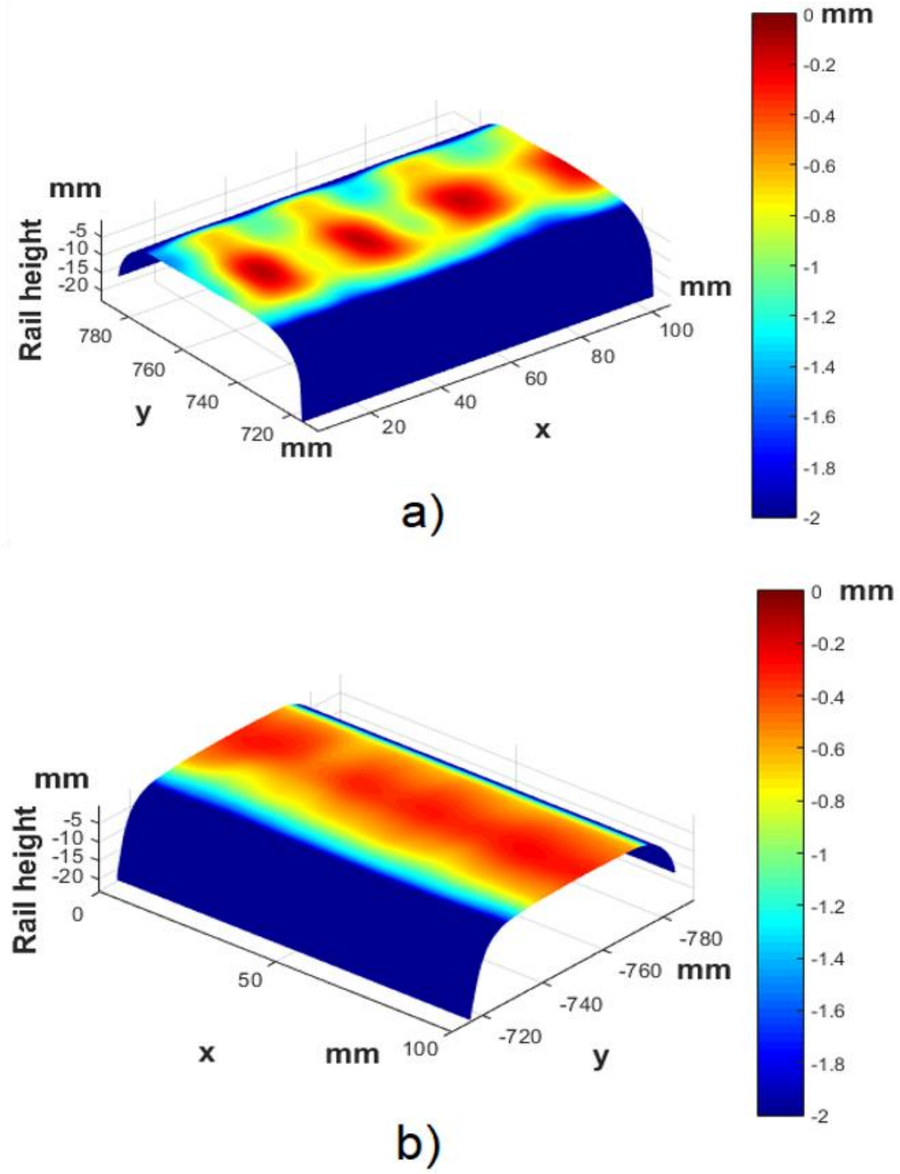

Fig. 127 Rail surfaces corrugation a) low rail b) high rail

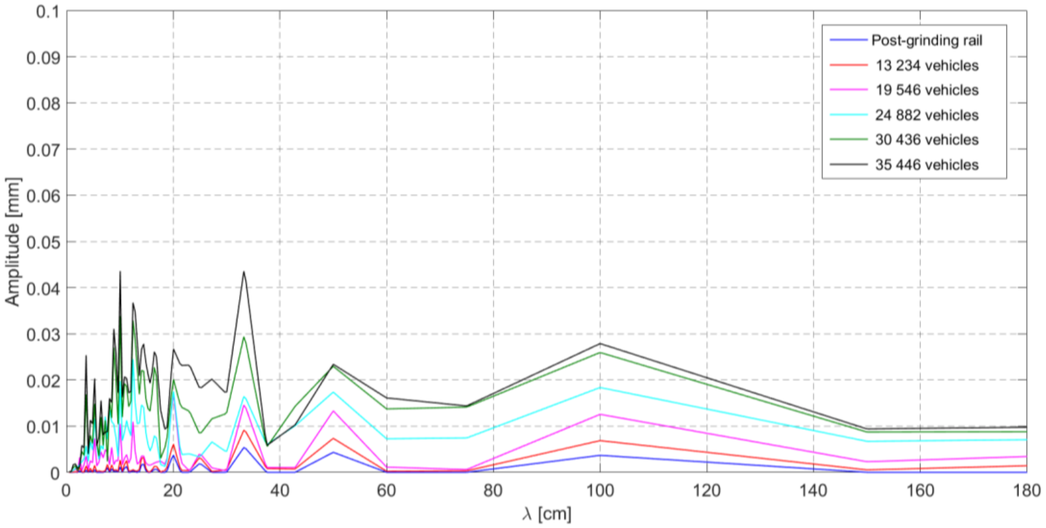

Fig. 128 DFT of the wear depth for the low rail

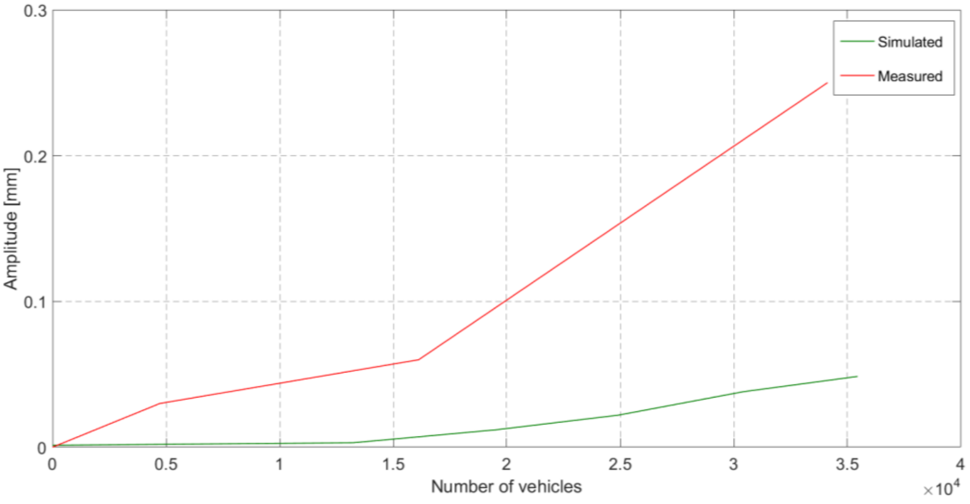

Fig. 129 Defect amplitude - numerical and experimental data

In Fig. 128 it can be observed the amplitude growth for each of the 5 rail step as a function of the number of train passages corresponding to 35 446 total vehicles running on the curve.

Fig. 129 shows the evolution of corrugation growth on low rail as function of train passages both for calculated and measured data. From Fig. 128 can be noticed that the maximum amplitude in the spectrum, considering the last rail step, is reached for a wavelength of about 10 cm: this is the reference wavelength of the calculated amplitude shown in Fig. 129. The discrepancy in the measured amplitudes is due to the absence of components flexibility, consequently since no wavelength-fixing mechanism could emerge, wear is not concentrated on a single wavelength but it is distributed over a broad waveband as shown in Fig. 128. Being corrugation a phenomenon which involves frequencies between 50 Hz and 1200 Hz, it is necessary to include bodies flexibility inside the corrugation model. In this frequency interval, the primary suspension of the vehicle often represents a filter for vibrations, thus accounting for the flexibility of sprung masses, e.g. bogie frame and car body, does not affect the predicted dynamic behaviour of the model. For sure, the model shall be improved including also the flexibility of the components, first of the wheelset since, considering the type of corrugation observed on the rail, the second torsional resonance of the driving axles is the wavelength-fixing mechanism of what is referred in literature as “rutting” corrugation. However, despite the simplification adopted, the model had shown a good behaviour considered its early stage of development.

6.4.3. Sensitivity analysis

A sensitivity analysis was carried out in order to evaluate the response of the developed model to some of the solutions presented in section 4.2, in particular the variation of friction coefficient and of the hardness of the rail material. Using harder rail and friction modifiers represents a very common way to mitigate this problem. In Table 27 are summarized tests carried out varying friction coefficient (Test 1) and rail hardness (Test 2).

Table 27 Sensitivity analysis tests

Test 1		**Test 2**	
Friction coefficient	**Rail hardness (HBW)**	**Friction coefficient**	**Rail hardness (HBW)**
0.2	270	0.3	270
0.3	270	0.3	350
0.4	270		
0.5	270		

In Fig. 130 is presented the evolution of the prevailing wavelength’s amplitude, as defined in the previous section for a variable friction coefficient. It can be observed that the higher the friction coefficient is, the faster is the corrugation growth. This is in accordance with the real behaviour, since a higher friction coefficient lead to higher maximum tangential pressure at the wheel-rail contact and thus to a greater wear rate.

In Fig. 131 is shown the influence of hardness of the rail surface: results are presented for hardness of 270 HBW and 350 HBW. As stated in [93], this type of hard rails provided a solution for corrugation on a main-line track in Germany which corrugation developed at about two-thirds of the rate on 350 HBW rail as on 260 HBW rail. Results are in accordance with reality, since corrugation is reduced using harder rails.

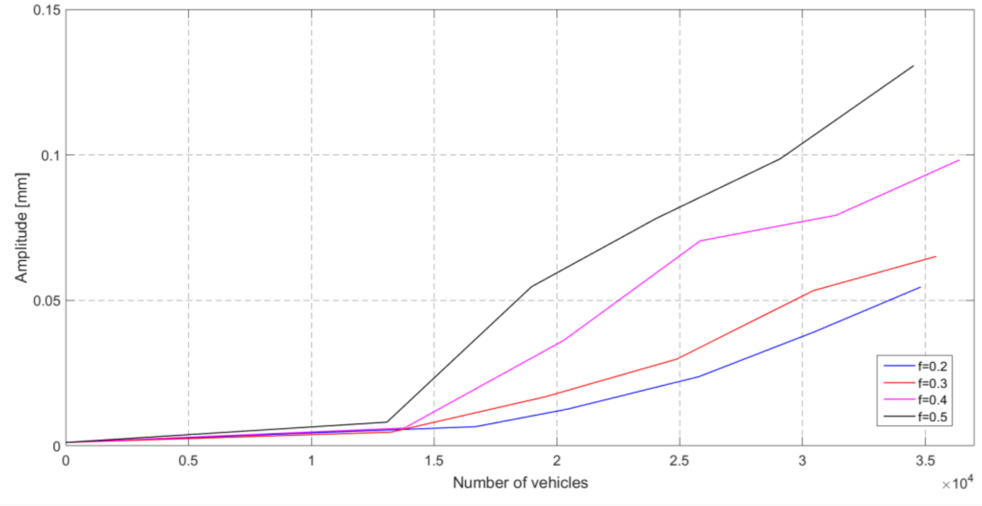

Fig. 130 Influence of friction coefficient on corrugation amplitude

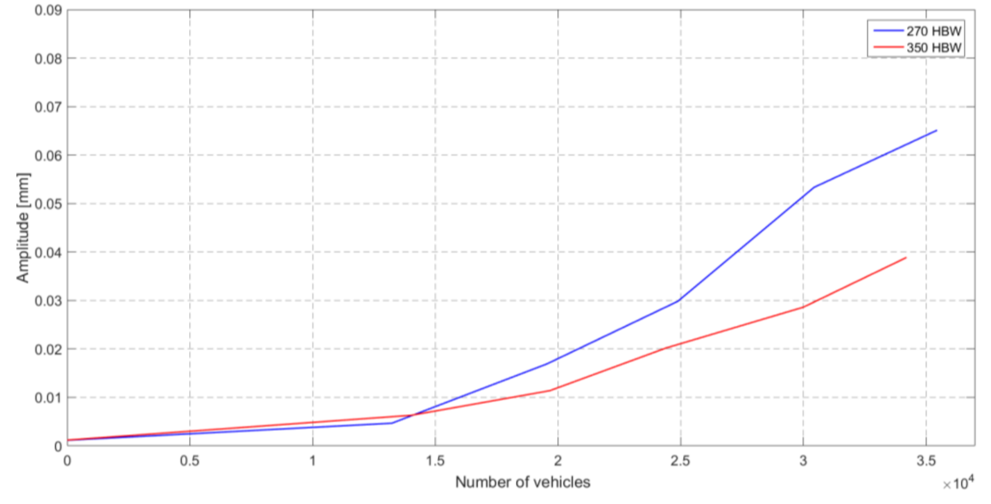

Fig. 131 Influence of rail hardness on corrugation amplitude

The sensitivity analysis had shown the good response of the model to variations of the most used solution to mitigate the problem. Numerical results had shown that the lower the friction coefficient is and higher rail hardness is, the lower is the corrugation growth in accordance with the real phenomena.

Conclusion

This Ph.D. work was carried out with the main purpose to fill a gap noticed in literature of efficient models able to predict the main damage mechanisms observed in railway field and suitable for complex networks. To face this issue, a complete tool for the wheel and rail wear, RCF and corrugation prediction has been developed characterized by a high numerical efficiency and suitable to be applied to complex railway lines.

The wear-RCF part is capable of simultaneously evaluating wear evolution and RCF crack growth (crack length and depth), both on the wheel and on the rail. The good compromise between numerical efficiency and accuracy, allows the wear-RCF model to be implemented into complex multibody models of railway and tramway vehicles to be used for large-scale simulations. Concerning RCF, the model is able to predict both the crack position on the wheel and rail profiles and its dimensions in terms of length and depth.

The whole wear-RCF model is made up of two main blocks: the first one evaluates the vehicle dynamics by means of the vehicle multibody model implemented in Simpack Rail and of a global wheel–rail contact model. The second block includes the wear model which, starting from the outputs of the multibody simulations, evaluates the amount of material to be removed through an experimental relationship found in the literature. The RCF model has been implemented in parallel to the wear model and calculates the crack characteristics starting from the same inputs. The influence of wear on crack growth (high wear rate may wear off short cracks) has been considered at the end of each calculation step.

To characterize the RCF damage law, specific experimental fatigue tests have been carried out in the laboratory of the Tribology Research Institute of the Southwest Jiaotong University, using two scaled rolling-sliding test machines.

Concerning the corrugation part of the tool, it consists of two parts, the dynamic model and the corrugation model. After implementing the initial irregularities and once the dynamic analyses have been carried out, in the corrugation model the quantity of material to be removed is assessed and the rail surfaces updated, to simulate the growth of corrugation. The model is also able to simulate the real evolution of wheel profiles running on the track, because of wear. In this way the dynamic vehicle-track interaction influenced by the real change in rail and wheels surface during the cyclic process has been considered. The outputs of the model are the 3D corrugated rail surfaces as a function of the number of train passages.

The tool has been applied to two different test case and the outputs have been compared against experimental data.

The first test case was the Florence tramway line characterized by very sharp curves and on which the Sirio vehicle, built by Hitachi Rail Italy, operates. The wear assessment has been evaluated both on the wheel and on the rail. The results highlight how the wear was mainly localized on the wheel flange and, in particular, on the flange top because of the flange top running motion typical of tramway vehicles. While, for the rail, it has been noticed how the wear was mainly concentrated on the flank and rise with the decrease of curve radius. As regards wheel RCF, the numerical results have shown a maximum crack depth of 0.73 mm after 81 088 km localized on the tread zone of the wheel while on the rail is located on the rail flank zone due to a greater concentration of the stress in that area especially for narrow curves. For the narrower curve of the line, the experimental validation of the wear model has been performed using a new ultra-accurate laser 3D measurement instrument. In particular, the data collected by means the 3D laser scanner have been used to study the shape evolution of the rail profile. Moreover, to complete the model validation, also the experimental data coming from a classical contact profilometer, the measurement instrument currently adopted for wear inspection on the Florence tramway line, have been considered to investigate the lateral wear. The results of the wear-RCF part have been encouraging both in terms of wear-RCF evaluation and in terms of numerical efficiency.

The proposed damage tool has been also tested considering a subway application. In this test case too, the aim was to evaluate the wear evolution and RCF crack growth and to compare the obtained results against experimental data. More in details, for the wheel, the model validation has been carried out comparing both the measured reference parameters and the measured wheel profiles with the simulated ones. While, for the rail, the attention was focused on two reference curves affected by severe damage comparing the experimental profile shape evolution with the simulated one. Since this scenario is affected by corrugation, the second part of the tool has been tested on a small-radius metro curve where defects because corrugation have been observed. In this currently version of the model, track and wheelsets have been considered as rigid. From numerical results, it has been observed that corrugation grows preferentially on the low rail of the track and this is in accordance with measurements. The DFT of the wear depth on the low rail showed a marked waveband in which the corrugation grows preferentially. This waveband includes the prevailing wavelength present on the real corrugated rail. A sensitivity analysis has also been carried out, regarding the response of the model to variations in friction coefficient and rail hardness: friction modifiers and hard rails are, in fact, commonly adopted solutions to mitigate this issue. Numerical results show that the lower the friction coefficient is and higher rail hardness, the lower is the corrugation growth. The results of the corrugation part have been encouraging considering the simplifications adopted in this first issue of the model.

Recommendations for future works

As regards future improvement of the tool, further model validations based on different vehicles and scenarios shall be considered. Moreover, new experimental campaigns on test rigs aimed at characterizing different wear/RCF mechanisms should be scheduled. The new campaigns should be carefully taken into account important aspects as contact geometries, external applied loads, sliding at the contact surface, adhesion conditions, rolling velocity, materials and temperature. Furthermore, it should be useful to include into the wear model the thermal effects and the hardening of the materials to have an even more accurate wear assessment.

Being corrugation a phenomenon which involves frequencies between 50 Hz and 1200 Hz, it is necessary to include bodies flexibility inside the corrugation model. Including wheelset flexibility inside the vehicle model should be another future step, since the second torsional resonance of the driving axles is the wavelength-fixing mechanism of what is referred in literature as “rutting” corrugation, the type observed on the benchmark curve. Also the flexibility of the track should be implemented together with the integration of a non-steady and non-linear theory of rolling contact as the Kalker’s complete theory. This theory would also allow to consider the real trend of the creeping force as a function of the creepage, thus letting to simulate the roll-slip motion, that usually exacerbates some type of corrugations.

References

[1] A. Innocenti, L. Marini, E. Meli, G. Pallini, A. Rindi "Development of a wear model for the analysis of complex railway networks" Wear 309 (2014), pp. 174-191

[2] M. Ignesti, L. Marini, M. Malvezzi, E. Meli, A. Rindi "Development of a wear model for the prediction of wheel and rail profile evolution in railway systems" Wear 284-285 (2012), pp. 1-17

[3] J. Pombo, J. Ambrosio, M. Pereira, R. Lewis, R.D. Joyce, C. Ariaudo, N. Kuka "A study on wear evaluation of railway wheels based on multibody dynamics and wear computation" Multibody Syst. Dyn. 24 (2010), pp. 347-366

[4] I. Zobory "Prediction of wheel/rail profile wear" Veh.Syst.Dyn. 28 (1997), pp. 221-259

[5] T. Jendel, M. Berg "Prediction of wheel profile wear" Suppl.Veh.Syst.Dyn. 37 (2002), pp 502-513

[6] J. Pombo, J. Ambrosio, M. Pereira, R. Lewis, R. Dwyer-Joyce, C. Ariaudo, N. Kuka "Development of a wear prediction tool for steel railway wheels using three alternative wear functions" Wear 271 (2011), pp. 238-245

[7] R.Enblom "On simulation of uniform wear and profile evolution in the wheel-rail contact" (Ph.D.thesis),2006

[8] R. Lewis, R.S. Dwyer-Joyce. "Wear mechanisms and transitions in railway wheel steels" IMechE Part J, J. Engineering Tribology, Vol. 218, pp. 467-478, 2004

[9] S. Bogdanski, M.W. Brown "Modelling the three-dimensional behavior of shallow rolling contact fatigue cracks in rails" Wear 253-285 (2002), pp. 17-25

[10] M. Kotoul "Crack path modelling in railway wheel under rolling contact fatigue" Applied and Computational Mechanics 9 (2015), pp. 103-126

[11] D.I. Fletcher, L. Smith, A. Kapoor "Rail rolling contact fatigue dependence on friction, predicted using fracture mechanics with a three-dimensional boundary element model" Engineering Fracture Mechanics 76 (2009), pp. 2612-2625

[12] Ringsberg, J. W. Shear mode growth of short surfacebreaking RCF cracks. *Wear*, 2005, 258, 955–963

[13] Beynon, J. H. and Kapoor, A. The interaction of wear and rolling contact fatigue. In Proceedings of theVARNA Conference, 1996

[14] B. Dirks, R. Enblom, and M. Berg “Prediction of wheel profile wear and crack growth – comparison with measurements” Wear 366-367 (2016), pp. 84-94

[15] B. Dirks, R. Enblom, A. Ekberg, M. Berg “The development of a crack propagation model for railway wheels and rails” Fatigue & Fracture of Engineering Materials & Structures 38 (2015), pp. 1478-1491

[16] F. Braghin, R. Lewis, R.S. Dwyer-Joyce, S. Bruni “A mathematical model to predict railway wheel profile evolution due to wear” Wear 261 (2006), pp. 1253-1264

[17] M.C. Burstow (2004) “Whole life rail model application and development for RSSB – continued development of an RCF damage parameter” Report AEA Technology Rail, AEATRES- 2004-880

[18] A. Ekberg, E. Kabo, H. Andersson “An engineering model for prediction of rolling contact fatigue of railway wheels” Fatigue Fract. Eng. Mater. Struct. 25 (2002), pp. 899-909

[19] A. Ekberg, B. Åkesson, E. Kabo “Wheel/rail rolling contact fatigue – probe, predict, prevent” Wear, 314 (2014), pp. 2-12

[20] A. Bevan, P. Molyneux-Berry, B. Eickhoff, M. Burtstow “Development and validation of a wheel wear and rolling contact fatigue damage model” Wear 307 (2013), pp. 100-111

[21] I. Goryacheva, S. Soshenkov, E. Torskaya “Modelling of wear and fatigue defect formation in wheel-rail contact” Veh.Syst.Dyn. 51 (2013), pp. 767–783

[22] I. Goryacheva, S. Zakharov “Rolling contact fatigue defects in freight car wheels” Wear 258 (2005), pp. 1142-1147

[23] Suresh S. “Fatigue of Materials” (1998) 2nd edition, Cambridge University Press, Cambridge

[24] K.L. Johnson “A graphical approach to shakedown in rolling contact” Proc.Conf. On Applied Stress Analysis (1990), Elsevier, pp. 263-274

[25] K.L. Johnson “A shakedown limit in rolling contact” Proc. 4th US Nat. Conference of Appl. Mech. (1962), ASME, pp. 971-975

[26] M. Malvezzi, E. Meli, S. Falomi, A. Rindi, Determination of wheel-rail contact points with semianalytic methods, Multibody Syst Dyn (2008) 20: 327-358, DOI 10.1007/s11044-008-9123-5

[27] J. Auciello, E. Meli, S. Falomi, M. Malvezzi “Dynamic simulation of railway vehicles: wheel/rail contact analysis” Vehicle System Dynamics, Vol. 47 (2009), No. 7, pp. 867-899,

[28] J.J. Kalker. “Three-Dimensional Elastic Bodies in Rolling Contact” Kluwer Academic Publishers, 1990

[29] EN 14363, March 2016, "Railway applications – Testing and Simulation for the acceptance of running characteristics of railway vehicles – Running behavior and stationary tests"

[30] J.J. Kalker "A fast algorithm for the simplified theory of rolling contact" Vehicle System Dynamics, Vol. 11, pp. 1-13, 1982

[31] H.Hertz "The contact of elastic solids" J.Reine Angew.Math.92 (1881)

[32] X.J. Zhao, J. Guo, Q.Y. Liu, E. Butini, L. Marini, E. Meli, A. Rindi, W.J. Wang "Effect of spherical dents on microstructure evolution and rolling contact fatigue of wheel/rail materials" Tribology International 127 (2018), pp. 520-532

[33] Li Z. and Kalker J. (1998). "Simulation of severe wheel-rail wear" Proceedings of the 6th International Conference on Computer Aided Design, Manufacture and Operation in the Railway and Other Advanced Mass Transit Systems, Sep. 2-4, Lisbon, Portugal, pp. 393-402

[34] O. Polach. "Fast wheel-rail forces calculation computer code" Vehicle System Dynamics Supplement, 33, pp. 728-739, 1999

[35] R. Enblom, M. Berg. "Simulation of railway wheel profile development due to wear influence of disc braking and contact environment" Wear 258 (2005), pp. 1055-1063

[36] T. Jendel and M. Berg. "Prediction of wheel profile wear". In: Suppl. Vehicle System Dynamics 37 (2002), pp. 502–513

[37] S. Iwnicki. "Hanbook of Railway Vehicle Dynamics" Taylor&Francis, 2006

[38] C. Esveld. "Modern Railway Track." Delft University of Technology, Delft, Netherland, 2001

[39] Rail Safety & Standard Board, Management and Understanding of Rolling Contact Fatigue – Literature Review, Report, 2006

[40] Lewis R. and Olofsson U. "Mapping rail wear regimes and transitions", *Wear*,257, pp. 721-729, 2004

[41] Bolton, P. J., and Clayton, P. "Rolling—sliding Wear Damage in Rail and Tyre Steels," Wear, **93**(2), pp. 145–165, 1984,

[42] Li Z. (2002) *Wheel-Rail Rolling contact and its application to wear simulation.* PhD Thesis. Delft University of Technology.

[43] Lewis, R., and Olofsson, U., 2009, *Wheel-Rail Interface Handbook*, Woodhead Publishing Limited, Cambridge, UK

[44] Olofsson U and Nilsson R, Surface cracks and wear of rail: a full scale test and laboratory study, Journal of Rail and Rapid Transit (2002), 216, 249-64.

[45] Archard J.F. (1953) 'Contact and Rubbing of Flat Surfaces', *Journal of Applied Physics*, 24, pp. 981-988.

[46] Dirks, B., 2015, Simulation and Measurement of Wheel on Rail Fatigue and Wear, Ph.D thesis

[47] J Tunna, J Sinclair, and J Perez "A review of wheel wear and rolling contact fatigue", Journal of Rail and Rapid Transit (2007), 221 Part F

[48] Cantini, S., and Cervello, S., 2016, _The Competitive Role of Wear and RCF: Full Scale Experimental Assessment of Artificial and Natural Defects in Railway Wheel Treads, Wear, 366-367, pp. 325-337

[49] Magel, E. E. "Rolling Contact Fatigue: A Comprehensive Review", U.S. Dep. Transp. Fed. Railr. Adm., (November 2011), p. 118

[50] Suresh S. (1998) Fatigue of Materials. 2nd edition, Cambridge University Press,Cambridge.

[51] Kalousek, J., and Magel, E. (1997 March). The magic wear rate. *Railway Track and Structures*

[52] Bold, P. E., Brown, M. W. and Allen, R. J. (1991), Shear mode crack growth and rolling contact fatigue, *Wear,* 144, 307-17

[53] Kapoor A., Fletcher D.I., Franklin F.J. and Alwahdi F. (2002) Whole life rail model interim report, T115 report 5, Rail Safety & Standards Board (RSSB)

[54] Brickle, B. J., Elkins, J. A., Grassie, S. L., and Handal, S. J. Rail corrugation mitigation in transit. Research Results

[55] Digest, Transit Cooperative Research Program, National Research Council, USA, number 26, June 1998

[56] S.L. Grassie, J.A. Elkins (2007), "Rail Corrugation on north american transit systems"

[57] Stuart L. Grassie "Rolling contact fatigue on the British railway system: treatment", Wear 258 (2005) 1310–1318

[58] S.L. Grassie, J. Kalousek (1993), "Rail Corrugation: characteristics, causes, and treatments", Proceedings of the Institution of Mechanical Engineers, Part F: Journal of Rail and Rapid Transit, 1993

[59] Grassie S.L, "Rail corrugation: characteristics, causes, and treatments", Proceedings of the Institution of Mechanical Engineers, Part F: Journal of Rail and Rapid Transit, v. 223(6), pp. 581-596, 2009

[60] Railway applications – track – acceptance ofwork – part 3: acceptance of rail grinding, milling and planing work in track, European Standard, EN 13231-3

[61] Y. Sato, A. Matsumoto, K. Knothe, Review on rail corrugation studies, Wear 253 (2002) 130–139

[62] E. Tassilly, N. Vincent, A linear model for the corrugation of rails. Journal of Sound and Vibration 150 (1991) pp. 25–45

[63] E. Tassilly, N. Vincent, Rail corrugations: analytical model and field tests. Wear 144 (1991) pp. 163–178

[64] A. Saulot, S. Descartes, Y. Berthier, Sharp curved track corrugation: From corrugation observed on-site, to corrugation reproduced on simulators. *Tribology International* **42** (2009) pp. 1691–1705

[65] S. Bruni, F. Cheli, F. Resta, “A model of an actively controlled roller rig for tests on fullsize railway wheelsets” Proceedings of the Institution of Mechanical Engineers, Part F, Journal of Rail and Rapid Transit 215 (2001) pp. 277–288

[66] L.E. Daniels, T.J. Devine, “FAST sheds light on corrugations” *Wear* (1983) pp. 174-176

[67] J. Kalousek, K.L. Johnson, “An investigation of short pitch wheel and rail corrugations on the Vancouver mass transit system” Proceedings of the Institution of Mechanical Engineers, Part F: Journal of Rail and Rapid Transit 206 (1992) pp. 127–135

[68] D.R. Ahlbeck, L.E. Daniels, “Investigation of rail corrugations on the Baltimore Metro” Wear 144 (1991) pp. 197–210

[69] Y. Suda, H. Komine, T. Iwasa, Y. Terumichi, “Experimental study on mechanism of rail corrugation using corrugation simulator” *Wear* **253** (2002) pp. 162–171

[70] Y. Suda, M. Hanawa, M. Okumura, T. Iwasa, “Study on rail corrugation in sharp curves of commuter line”. *Wear* **253** (2002) pp. 193–198

[71] A. Matsumoto, Y. Sato, H. Ono, M. Tanimoto, Y. Oka, E. Miyauchi, “Formation mechanism and countermeasures of rail corrugation on curved track” *Wear* **253** (2002) pp. 178–184

[72] B. Kurzeck, M. Hecht, “Dynamic simulation of friction-induced vibrations in a light railway bogie while curving compared with measurement results” Vehicle System Dynamics 48 (2010) pp. 121–138

[73] B. Kurzeck, “Combined friction induced oscillations of wheelset and track during the curving of metros and their influence on corrugation”. Wear 271 (2011) pp. 299–310

[74] Torstensson, P. ; Pieringer, A. ; Nielsen, J. (2014) "Simulation of rail roughness growth on small radius curves using a non-Hertzian and non-steady wheel-rail contact model". Wear,nSpecial issue. Proc. of the 9th Conference on Contact Mechanics and Wear of Rail/Wheel Systems, SW Jiaotong Univ, State Key Lab Tract Power, Chengdu, China. Aug 2012, vol.3

[75] Y.Q. Sun, S. Simon (2008), Wagon-track modelling and parametric study on rail corrugation initiation due to wheel stick-slip process on curved track

[76] Carlberger A., “Simulation of rail corrugation growth on curves”, Master’s thesis, Department of Applied Mechanics, Division of Dynamics, Chalmers University of Technology, Gothenburg, Sweden, 2016

[77] Torstensson P.T., “Rail Corrugation Growth on Curves”, PhD thesis, Department of Applied Mechanics, Chalmers University of Technology, Gothenburg, Sweden, 2012

[78] Simpack manual, Simpack 9.10.2.

[79] Matlab Mathematics user guide, The MathWorks, Inc. (2018)

[80] Ekberg A. (2000) “Rolling Contact Fatigue of Railway Wheels - Towards Tread Life Prediction Through Numerical Modelling Considering Material Imperfections, Probabilistic Loading and Operational Data” PhD thesis. Chalmers University of Technology.

[81] EN 14363, March 2016, “Railway applications – Testing and Simulation for the acceptance of running characteristics of railway vehicles – Running behavior and stationary tests”

[82] Valigi M. C., Logozzo S., Affatato S. “New challenges in Tribology: Wear assessment by using 3D Optical Scanners” Materials,10 (5), pp. 548 (2017)

[83] Akkök M., Acar B., Açmaz E. “Experimental analysis and wear modeling for mechanical components of a typical rail launcher” Wear. 2013; 306:1–9

[84] Valigi M.C., Fabi L., Gasperini I. “Wear resistance of new blade for planetary concrete mixer” (2013) 5th World Tribology Congress, WTC 2013, 2, pp. 1208-1211

[85] Carmignato S., Spinelli M., Affatato S., Savio E. “Uncertainty evaluation of volumetric wear assessment from coordinate measurements of ceramic hip joint prostheses” Wear 2011, 270, 584–590

[86] Uddin M.S. “Wear measurement and assessment of explanted cross-linked PE acetabular cups using a CMM” Tribol. Trans. 2014, 57, 767–777

[87] Valigi M.C., Logozzo S., Butini E., Meli E., Marini L., Rindi A.” Experimental evaluation of tramway track wear by means of 3D metrological optical scanners” (2018) Proceedings of the 11th International Conference on Contact Mechanics and Wear of Rail/wheel Systems, CM 2018, pp. 1007-1012

[88] Valigi M.C., Logozzo S., Rinchi M. “Wear resistance of blades in planetary concrete mixers. Design of a new improved blade shape and 2D validation” Tribology International, 96, pp. 191-201(2016)

[89] Valigi M.C., Logozzo S., Rinchi M. "Wear resistance of blades in planetary concrete mixers. Part II: 3D validation of a new mixing blade design and efficiency evaluation" Tribology International, 103, pp. 37-44. (2016)

[90] Valigi M.C., Logozzo S., Gasperini I. "Study of wear of planetary concrete mixer blades using a 3D optical scanner" (2015) ASME International Mechanical Engineering Congress and Exposition, Proceedings (IMECE), 15-2015

[91] Valigi M.C., Logozzo S., Rinchi M., Galletti L. "New prototype of blade for planetary concrete mixers and wear analysis with a new method" (2018) Betonwerk und Fertigteil-Technik/Concrete Plant and Precast Technology, 84 (6), pp. 18-25

[92] Affatato S., Valigi M.C., Logozzo, S. "Wear distribution detection of knee joint prostheses by means of 3D optical scanners", (2017) Materials, 10 (4), art. no. 364

[93] Heyder R., Girsch G., "Testing of HSH rails in highspeed tracks to minimise rail damage", Wear, v. 258, pp. 1014-1021, 2005.

Publications

[1] X.J. Zhao, L.C. Guo, J. Guo, Q.Y. Liu, L. Marini, E. Meli, A. Rindi, W.J. Wang, “Effect of spherical and ballast dents on rolling contact fatigue of rail materials”, Wear 450-451 (2020)

[2] E. Butini, L. Marini, M. Meacci, E. Meli, A. Rindi, X.J. Zhao, W.J. Wang, “An innovative model for the prediction of wheel - rail wear and rolling contact fatigue”, Wear 436-437 (2019)

[3] E. Butini, L. Marini, E. Meli, A. Rindi, MC. Valigi, S. Logozzo, “Development and validation of wear models by using innovative three-dimensional laser scanners” Advances in Mechanical Engineering Vol. 11(8) 1–14 (2019)

[4] X.J. Zhao, J. Guo, Q.Y. Liu, E. Butini, L. Marini, E. Meli, A. Rindi, W.J. Wang, “Effect of spherical dents on microstructure evolution and rolling contact fatigue of wheel/rail materials”, Tribology International 127 pp. 520–532 (2018)

[5] M. Meacci, Z. Shi, E. Butini, L.Marini, E.Meli, A.Rindi, “A local degraded adhesion model for creep forces evaluation: An approximate approach to the tangential contact problem”, Wear 440-441 (2019)

[6] E. Butini, L. Marini, M. Meacci, E. Meli, A. Rindi, Z. Shi, X.J. Zhao, W.J. Wang, “An innovative tool for simultaneous wheel and rail damage evaluation”, Proceeding of the 9th ECCOMAS Multibody Dynamics Conference, 15-18 July 2019, Duisburg, Germany

[7] E. Butini, M. Meacci, E. Meli, M. Porcelli, A. Rindi, Z. Shi, “An improved wheel-rail contact model under degraded adhesion condition for multibody dynamics simulation”, Proceeding of the 9th ECCOMAS Multibody Dynamics Conference, 15-18 July 2019, Duisburg, Germany

[8] Elisa Butini, Lorenzo Marini, Martina Meacci, Enrico Meli, Andrea Rindi, Zhiyong Shi, Xiangji Zhao, Wenjian Wang “An innovative tool for simultaneous wheel and rail damage evaluation” 26th IAVSD Symposium on Dynamics of Vehicles on Roads and tracks, 12-16 August 2019, Gothenburg, Sweden

[9] E.Butini, L.Marini, M.Meacci, E.Meli, A.Rindi, “Development of an innovative model to study wear evolution considering wheel-rail conformal contact”, Proceedings of the 8th ECCOMAS Thematic conference on MULTIBODY DYNAMICS, Prague 19-22 June 2017

[10] E. Boccini, E.Butini, L.Marini, M.Meacci, E.Meli, A.Rindi "Development of an innovative degraded adhesion model for railway multibody applications", Proceedings of the 8th ECCOMAS Thematic conference on MULTIBODY DYNAMICS, Prague 19-22 June 2017

[11] E.Butini, L.Marini, E.Meli, S.Panconi, A.Rindi, B.Romani, "New wear model considering wheel-rail conformal contact", Proceedings of the First International Conference on Rail Transportation - ICRT 2017, Chengdu 10-12 July 2017

[12] E.Butini, A.Frilli, L.Marini, E.Meli, S.Panconi, A.Rindi, B.Romani, "An efficient wheel-rail conformal contact model for multibody simulation", Proceedings of the First International Conference on Rail Transportation - ICRT 2017, Chengdu 10-12 July 2017

[13] E. Butini, A. Frilli, E. Meli, D. Nocciolini, S. Panconi, L.Pugi, A. Rindi, B. Romani, "Innovative model for the efficiency optimization for high-speed trains through the recovery of braking energy", Proceedings of the First International Conference on Rail Transportation - ICRT 2017, Chengdu 10-12 July 2017

[14] E.Butini, L.Marini, M.Meacci, E.Meli, A.Rindi, "Development of an innovative tool for simultaneous wheel and rail wear and RCF damage evaluation", Proceedings of the 11th International Conference on Contact Mechanics and Wear of Rail/Wheel Systems – Delft 24-27 September 2018

[15] E.Butini, L.Marini, M.Meacci, E.Meli, A.Rindi, "Wear and Rolling Contact Fatigue: development of an innovative tool for simultaneous wheel and rail damage evaluation", Proceedings of the 5th Joint International Conference on Multibody System Dynamics, 24 – 28 June 2018, Lisbon, Portugal

[16] E. Butini, L. Marini, E. Meli, A. Rindi, S. Logozzo, M.C. Valigi, "Development and validation of a wear model by means of innovative measuring instruments", Proceedings of the 5th Joint International Conference on Multibody System Dynamics, 24 – 28 June 2018, Lisbon, Portugal

[17] E.Butini, L.Marini, M.Meacci, E.Meli, A.Rindi, Zhiyong Shi, "A New Local Degraded Adhesion Model for Railway Applications Including Energy Dissipation and Adhesion Recovery", Proceedings of the 5th Joint International Conference on Multibody System Dynamics, 24 – 28 June 2018, Lisbon, Portugal

[18] E. Butini, L. Marini, E. Meli, A. Rindi, S. Logozzo, M.C. Valigi, "Development and validation of a wear model by using innovative non-contact measuring instruments", Proceedings of the 4th International Conference on Railway Technology, Sitges, Barcelona, Spain 3-7 September 2018

[19] E.Butini, L.Marini, M.Meacci, E.Meli, A.Rindi, "Development of an innovative tool for wheel and rail wear and rolling contact fatigue evaluation", Proceedings of the 4th International Conference on Railway Technology, Sitges, Barcelona, Spain 3-7 September 2018

[20] E.Butini, L.Marini, M.Meacci, E.Meli, A.Rindi, Zhiyong Shi, "A New Local Degraded Adhesion Model for Railway Applications Including Energy Dissipation and Adhesion Recovery" Proceedings of the 4th International Conference on Railway Technology, Sitges, Barcelona, Spain 3-7 September 2018